Critical flow velocity in superfluid ^{3}He-B

Maros Skyba, MPhys (Hons.)

February, 2016

A thesis submitted in fulfilment

of the requirements of the degree of

Doctor of Philosophy

at Lancaster University

Critical flow velocity in superfluid ^{3}He-B

Maros Skyba

MPhys (Hons.)

February, 2016

Abstract

The experiments detailed within this thesis have measured the distortion of the superfluid energy gap in high magnetic field and the dissipation for an object in uniform linear motion through superfluid ^{3}He-B. The latter experiments led to an astonishing discovery of no discontinuity in the dissipation for an object in uniform linear motion at the Landau critical velocity. The experiments were performed in a "Lancaster style" nested experimental cell at ultra-low temperatures within the ballistic limit.

In the first set of experiments we studied two almost identical quartz tuning fork resonators with different vibration directions with respect to the vertical magnetic field. One vibrated along the field direction and the other vibrated in the horizontal plane. Our measurements have shown that the critical velocity for the vertical fork decreases significantly with increasing field, dropping to almost 60% of its original value as the highest field is approached. However, there is very little change of the critical velocity for the horizontal fork. Our data shows good agreement with theoretical predictions and previous experiments using vibrating wires.

During measurements at high magnetic fields, 300 mT to 330 mT, we observed discontinuities in the velocity response for very small changes in driving force. This behaviour might be due to vortex generation around the vibrating object and a subsequent shielding effect, previously observed in the response of a large vibrating wire (with diameter of 100 μm, similar to a typical fork dimension). Intriguingly the detailed behaviour also appears to depend on the orientation of the tuning fork with respect to the magnetic field direction.

The second set of experiments used a novel measurement tool referred to as the "flopper". The idea behind the development of the flopper was to have a low frequency device with low Q-factor that could be moved in an arbitrary fashion. The flopper is a large 25×9 mm goalpost-shaped NbTi vibrating wire. With AC current the wire can be driven at its resonance frequency or by using a DC linear stroke it can be moved over a controlled distance within the cell. By adding a high frequency "probe" signal on top of the DC signal we calibrated the position of the flopper with respect to the cell. We performed DC strokes of the flopper over short distances within the cell at various velocities. This led to us discovering that the dissipation of uniform linear motion at velocities exceeding the Landau velocity did not show any discontinuity. Since the critical Landau velocity is so fundamental in the understanding of superfluidity, this was a considerable surprise. The comparisons between AC and DC motion led to the development of a model to describe the dissipation processes in ^{3}He-B.

Declaration

The work within this thesis was a collaborative effort between members of the Lancaster University Low temperature Group and has not been submitted in substantially the same form for the award of a higher degree elsewhere. Any sections of the thesis which have been published, or submitted for a higher degree elsewhere, are clearly identified.

Acknowledgements

Lastly, I would like to thank Professor Fisher for always supporting all the PhD. students and always being eager to explain any physical problems. You are greatly missed, and I would like to dedicate this work to your memory.

Contents

List of Figures

xii

Chapter 1

Introduction

Out of the whole periodic table few elements have such remarkable properties as helium. As a noble gas element helium has zero valence and under normal conditions it is chemically non-reactive. Helium has two stable isotopes, helium-4 (^{4}He) and helium-3 (^{3}He). Both of these liquefy at very low temperatures, ^{4}He at $4.2\,\mathrm{K}$ and ^{3}He at $3.19\,\mathrm{K}$ at $1\,\mathrm{bar}$. What sets helium apart from other elements is that both of its isotopes stay liquid all the way to $T = 0\,\mathrm{K}$, at low pressures. In order to solidify ^{4}He or ^{3}He the pressure needs to exceed $25\,\mathrm{bar}$ and $34\,\mathrm{bar}$ at $T = 0$, respectively. The zero point energy of helium, be it ^{4}He or ^{3}He, is larger than the binding energy of the atoms below these pressures. Quantum mechanical effects dominate at low temperatures.

^{4}He is a composite boson, therefore it is governed by Bose-Einstein statistics. When cooled to around $2\,\mathrm{K}$, ^{4}He atoms start forming a Bose-Einstein condensate. The condensate is the superfluid and is described by a macroscopic wave function.

The atom of ^{3}He is made up of two electrons, two protons but only one neutron. The atom has half integer spin and is thus a composite fermion so that ^{3}He atoms are governed by Fermi-Dirac statistics. At temperatures of approximately $1\,\mathrm{mK}$ ^{3}He undergoes a second-order phase transition into a superfluid state. Superfluid ^{3}He is one of the purest substances in the universe. Similarly to superconductors, the superfluid is made of Cooper pairs, however, in case of ^{3}He the pairs are made of ^{3}He atoms. The creation of Cooper pairs gives rise to an energy gap Δ in the excitation spectrum. In superfluid ^{3}He there are many fascinating effects and phases. There are 3 well-known superfluid phases ^{3}He-A, ^{3}He-A$_1$ and ^{3}He-B, however, recent experiments suggest a fourth phase of superfluid ^{3}He existing in confined geometries [4]. Superfluid ^{3}He is also widely used as a model to relate to other quantum systems. When undergoing the phase transition to superfluid, ^{3}He spontaneously breaks three symmetries in an effect analogous to cosmological theories of the universe in its early stages [5]. Helium-3 proves to be an ideal model system to simulate effects within the universe which are hard to reach or observe directly (e.g. creation of topological defects, simulation of black holes [6]).

In this thesis I am focusing on some of the fundamental properties of superfluid ^{3}He, namely the superfluid energy gap and the critical flow velocity. In 1941 Landau [7, 8] considered the difference between normal fluid flow and superfluid flow through a capillary tube. He showed that if the velocity of the flow is below a certain value (the Landau critical velocity v_L), then no excitations are created and the liquid flows without viscosity. This critical velocity is well known in ^{4}He to be approximately $50\,\mathrm{m\,s^{-1}}$. A simple way to understand this result is by realising that if we have an object moving through the superfluid at velocity v, in its rest frame an excitation will have its energy shifted from E to $(E - pv)$. Spontaneous generation of excitations is expected to start when this shifted energy is equal to 0.

When this theory is applied to superfluid ^{3}He-B at 0 bar, we get $\mathrm{v}_L = \Delta/p_F = 27.3\,\mathrm{mm\,s^{-1}}$ for the critical velocity of the superfluid. Where $p_F = 8.28 \times 10^{-25}\,kg\,m\,s^{-1}$ is the Fermi momentum. However, measurements performed in superfluid ^{3}He using objects in oscillatory motion (such as vibrating wires) find critical velocities at approximately $9\,\mathrm{mm\,s^{-1}}$ which is $v_L/3$. To date the only measurement of the Landau velocity in superfluid ^{3}He-B was done by Ahonen $et.al.$[2]. In their studies on the mobility of negative ions they found a critical velocity consistent in magnitude with the Landau limit for pair breaking. Utilising our new experimental tool, the "flopper" (a special large vibrating wire), we can compare the differences in dissipation/damping between the oscillatory motion and steady motion of the same object moving through superfluid ^{3}He-B. We report the surprising result that the expected onset of dissipation at $v_L/3$ is completely absent in steady motion. Furthermore, there appears to be no extra onset of pair-breaking upon reaching the full Landau critical velocity.

The work presented in this thesis is a result of collaboration of all members of the ULT Lancaster group. My first task was fixing the numerous problems on the dilution refrigerator, like several leaks and a short in three out of four heat exchangers (this is addressed in section 4.1). Upon successfully repairing the

dilution refrigerator I performed all the measurements and analysis of the data presented in this thesis (chapters 5 and 6). I have helped in development of the model describing the dissipation processes (section 6.3).

This thesis is organised as follows. Chapter 2 gives a brief historical summary of Landau's theory and experiments involved in proving this theory.

The background theory of ^{3}He is discussed in chapter 3, addressing normal ^{3}He, mixtures of ^{3}He with ^{4}He and superfluid ^{3}He and its phases. Particular attention is given to the quasiparticle damping force and the ballistic regime in superfluid ^{3}He-B where all of the presented experiments were performed.

Chapter 4 describes the experimental set-up, starting from a discussion of cooling methods, dilution refrigeration and nuclear adiabatic demagnetisation. Then follows a detailed description of the experimental cell. This chapter also includes oscillator theory and a description of the various devices used in the experiment. Particular attention is given to our new experimental tool, the flopper. At the end of this chapter, the measurement techniques used are introduced.

The first presented experiment is in chapter 5. It is the measurement of the ^{3}He-B energy gap distortion due to external magnetic field by tuning forks. Techniques of measuring and determining the critical velocity are described. The results are compared with the previous work.

The Landau critical velocity experiment is presented in chapter 6. Measurements and calibrations in oscillatory motion (AC) are explained at the beginning of the chapter. The DC measurements follow and comparisons are made between AC and DC modes of operation of the flopper with all the other vibrating objects. At the end of the chapter I discuss our view of the model of the dissipation processes.

The last chapter gives a summary of all the results presented within this thesis together with a discussion about possible future work.

Chapter 2

Historical measurements

In 1908 Heike Kamerlingh Onnes liquefied ^{4}He, thus starting low and ultra-low temperature experimental physics. Although Kamerlingh Onnes reached the superfluid temperatures of ^{4}He, it was not until 1938 when Kapitza [9] actually recognized the new state, followed closely by Allen and Misener [10, 11]. Superfluidity was a brand new, not very well understood phenomenon. In the following years of the 20$^\text{th}$ century, the drive to achieve lower temperatures led to rapid developments in cryogenic technology and to greater understanding of fundamental physical properties of matter at ultra-low temperatures. The fast development of this very new field is attributed to close co-operation between experimental and theoretical physicists. Perhaps one of the most important co-operations started in 1939 when Kapitza enlisted theoretical physicist Lev Landau to his ongoing experiments in ^{4}He.

Landau in his work in 1941 laid the foundation of superfluid theory [7, 8]. He quantized the hydrodynamics of quantum liquids and proposed that "every weakly excited state can be considered as a combination of elementary excitations". He then split these elementary excitations into two categories. The first category are the phonons. Their linear energy dependence on momentum is well known, $\epsilon = cp$, here c is the velocity of first sound. The second category of excitations are rotons. The energy of rotons is related to momentum by a quadratic function $\epsilon = \Delta + \frac{(p-p_0)^2}{2\mu}$, where μ is the effective mass of a roton and p_0 is the momentum of the roton minimum. Dispersion relations for ^{4}He as proposed by Landau are shown on figure 2.1. The proposed excitation spectrum of superfluid ^{4}He was verified in 1961 by Henshaw and Woods from neutron-scattering experiments [12].

From the excitation spectrum Landau formulated the criterion of superfluidity [7]. Imagine a large body of mass M moving through the superfluid at velocity V_i. Let's assume that the temperature is low enough that the ^{4}He is a pure superfluid. In these conditions as long as V_i is small enough, the body will not experience any drag from the superfluid. This will be the case until the velocity reaches a critical point v_L where excitations are created directly from the superfluid, which
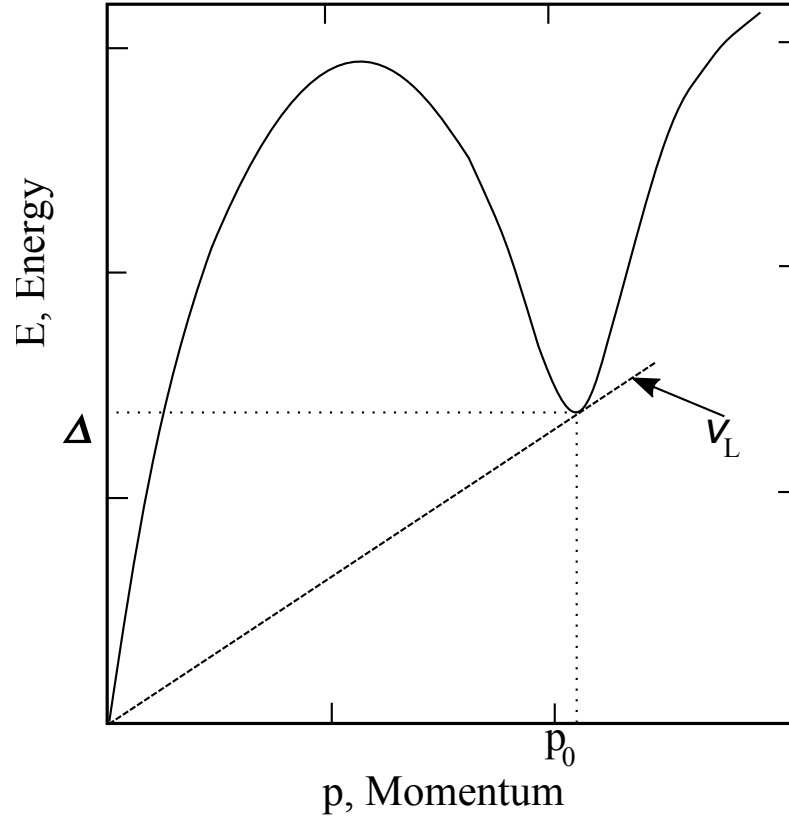
Figure 2.1: Dispersion relation of ^{4}He. The dashed line corresponds to the critical velocity.

leads to the loss of the body's kinetic energy. Thus, the body is experiencing drag. Assuming that the creation of one excitation at energy of $\epsilon(p)$ and momentum p causes the body to change its velocity from V_i to V_f, then the conservation of energy leads to

$$\frac{1}{2}MV_i^2 = \frac{1}{2}MV_f^2 + \epsilon(p), \tag{2.1}$$

and conservation of momentum gives

$$M\mathbf{V}_i = M\mathbf{V}_f + \mathbf{p}. \tag{2.2}$$

Combining (2.1) and (2.2) to eliminate V_f from we get

$$\epsilon(p) - \mathbf{p}.\mathbf{V}_i + p^2/2M = 0. \tag{2.3}$$

Now assuming that M is very large, the last term in equation (2.3) can be neglected. Then, if Θ is the angle between $\mathbf{p}$ and $\mathbf{V}_i$, we can write

$$pV_i \cos\Theta = \epsilon(p), \tag{2.4}$$

and since $\cos\Theta \leq 1$, then

$$V_i \leq \epsilon(p)/p. \tag{2.5}$$

This is the condition that must be satisfied for excitation creation. Creation of excitations becomes energetically favourable at the Landau critical velocity given by

$$v_L = \min\left(\frac{\epsilon}{p}\right). \tag{2.6}$$

From equation 2.6 follows that superfluidity will occur if

$$v_L = \min\left(\frac{\epsilon}{p}\right) > 0, \tag{2.7}$$

which is known as the Landau criterion of superfluidity [7, 13].

Looking at figure 2.1 we see that the minimum described by equation (2.6) lies in the region of roton minimum. Equation (2.6) can be rewritten as:

$$v_L \approx \frac{\Delta}{p_0}, \tag{2.8}$$

substituting the values we get $v_L = 60\,\mathrm{m\,s^{-1}}$ for $0\,\mathrm{bar}$.

The critical velocity was measured in 1977 by D. R. Allum and P. V. E. McClintock [1], later repeated in 1985 by T. Ellis and P. V. E. McClintock [14] by utilising fast moving negative ions in ^{4}He at $0.35\,\mathrm{K}$ and $25\,\mathrm{bar}$. Their results are shown on figure 2.2. The drag on the negative ion moving through superfluid ^{4}He at velocities smaller than v_L is negligible. However, upon reaching the critical velocity predicted by Landau theory, the drag on the ion dramatically increases, suggesting large dissipation.
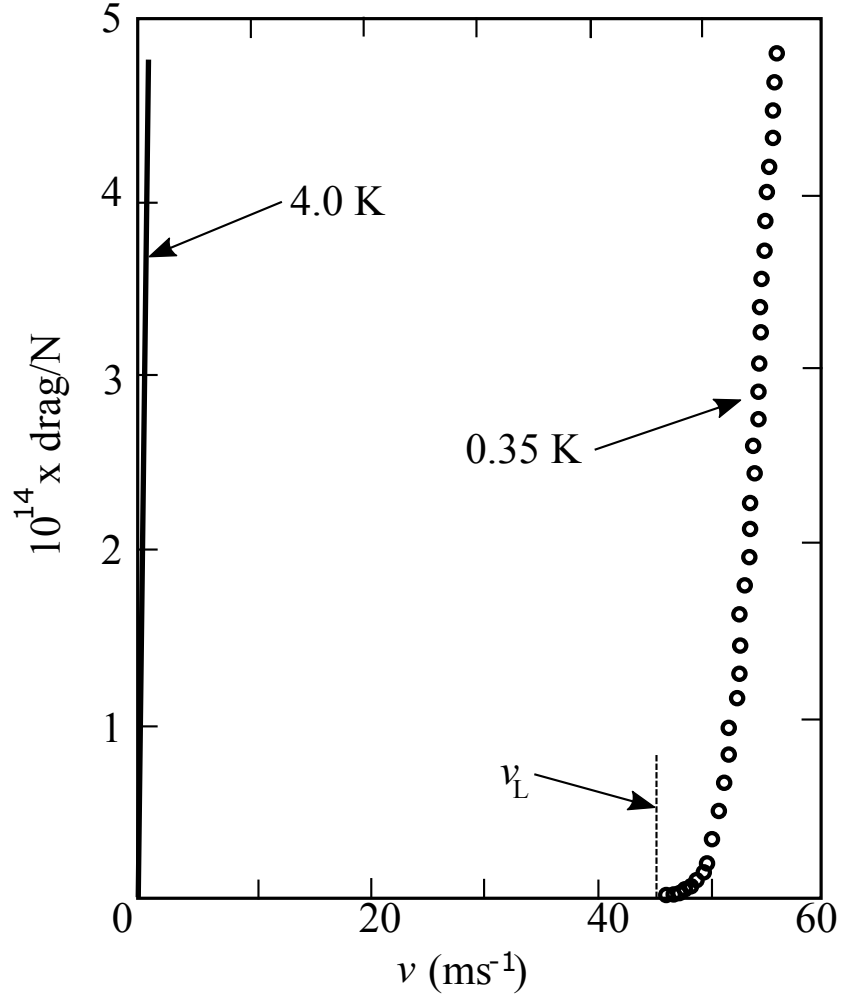
Figure 2.2: Drag force on a negative ion as function of its velocity through superfluid ^{4}He at 0.35 K. From [1].

In the case of ^{3}He, its superfluidity was proposed by L. P. Pitaevskii in 1959 [15]. However, it took 6 years until the first experiments began on dilution refrigerators that could prove experimentally the superfluidity of ^{3}He. Seven years later, 13 years after the first proposition by Pitaevskii, in 1972 R. Richardson, D. Osheroff and D. Lee, using Pomeranchuk cooling, registered one kink and one small jump in their pressure vs. temperature measurements of a coexistence of solid and liquid ^{3}He. The kink corresponded to the second order phase transition from the normal liquid to superfluid state and the jump was the first order phase transition between ^{3}He-A and ^{3}He-B [16]. In 1996 R. Richardson, D. Osheroff and D. Lee shared the Nobel physics prize for their discovery. Since 1972 there have been

countless experiments and theoretical works describing the basic properties of ^{3}He. One such property is the critical velocity as introduced by Landau (equation (2.8)). The superfluid ^{3}He is very well described by Bardeen, Cooper and Schrieffer theory [17]. The creation of Cooper pairs of ^{3}He atoms gives rise to an energy gap Δ, which can be expressed as [18]

$$\Delta = 1.76 k_B T_c, \tag{2.9}$$

where k_B is the Boltzman constant and T_c is the critical temperature. It was shown experimentally that the critical temperature is proportional to the pressure [19, 20]. Considering the equation (2.8) and very small changes in p_F with varying pressure [20], it means that with increasing pressure the Landau critical velocity increases.

Helium-3 has multiple diverse phases. These phases differ from one another in shapes of their energy gaps (shown in the next theoretical chapter). In 1976 Ahonen *et.al.*[2] performed experiments measuring the mobility of negative ions in superfluid ^{3}He at high pressures (18 bar). Their results are shown in figure 2.3. They report a critical velocity consistent in magnitude with the Landau limit at a pressure of 18 bar.

Many experiments followed using various experimental devices. Since 1986 experiments elucidating the interaction of superfluid ^{3}He with oscillating objects were performed (see for example [21, 22, 23, 24, 25]). In these experiments typically the moving objects were vibrating wires, showing increase in damping at velocities approximately $9\,\mathrm{mm\,s^{-1}}$. This was roughly 3 times smaller than the critical velocity calculated from equation (2.8) using values for the ^{3}He-B energy gap derived from BCS theory. The origin of this phenomena can be explained as follows. As the wire moves through the superfluid, the superfluid component has to accommodate the motion of the wire by pure potential flow of incompressible fluid. For a cylinder this potential flow has a maximum relative velocity to the wire of $2v$ at the top and the bottom of the wire. This phenomenon will be addressed in the later
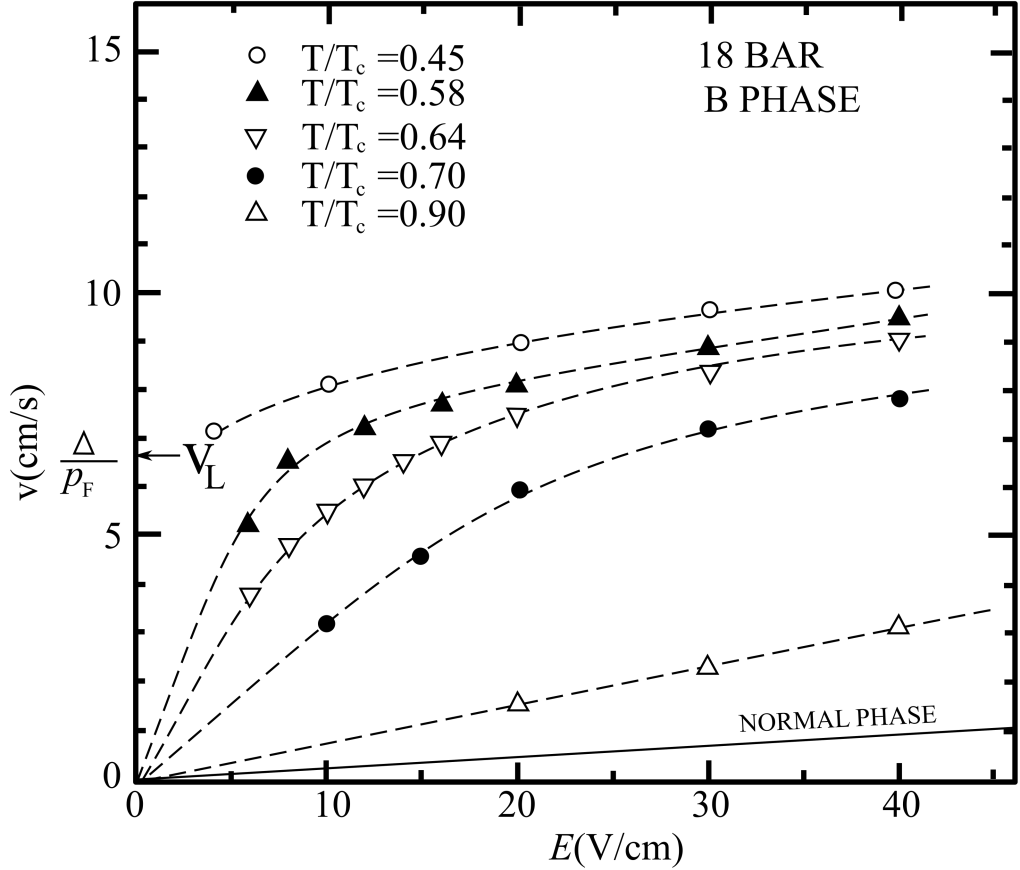
Figure 2.3: Drag force on a negative ion as function of its velocity through superfluid ^{3}He at 18 bar. From [2].

section 4.4.6. Furthermore, while the wire is moving, the dispersion curves of the superfluid close to the wire are tilted by a Galilean transformation of $\pm p_F v$. Now equation (2.8) can be rewritten to

$$2p_F v = \Delta - p_F v, \tag{2.10}$$

$$v_c = \frac{\Delta}{3p_F}. \tag{2.11}$$

Measurements of $v_c = v_L/3$ were largely considered as a proof of Landau criterion of superfluidity.

Our recent experiment (2014-2015) involved using a very special experimental tool called the flopper. Its unique features are its ability to move linearly with constant velocity through superfluid ^{3}He, its very low Q-factor and low

resonance frequency. During our experiment we were able to drive this device at velocities larger than Landau critical velocity, approximately $2v_L$, without seeing any associated dissipation.

Chapter 3

Theoretical background

3.1 Helium 3 phase diagram

Helium-3 liquefies at approximately 3.2 K at atmospheric pressure [20]. The liquefaction is mediated via van der Waals interactions between the ^{3}He atoms. Due to its large zero point oscillations, ^{3}He remains liquid until zero temperature
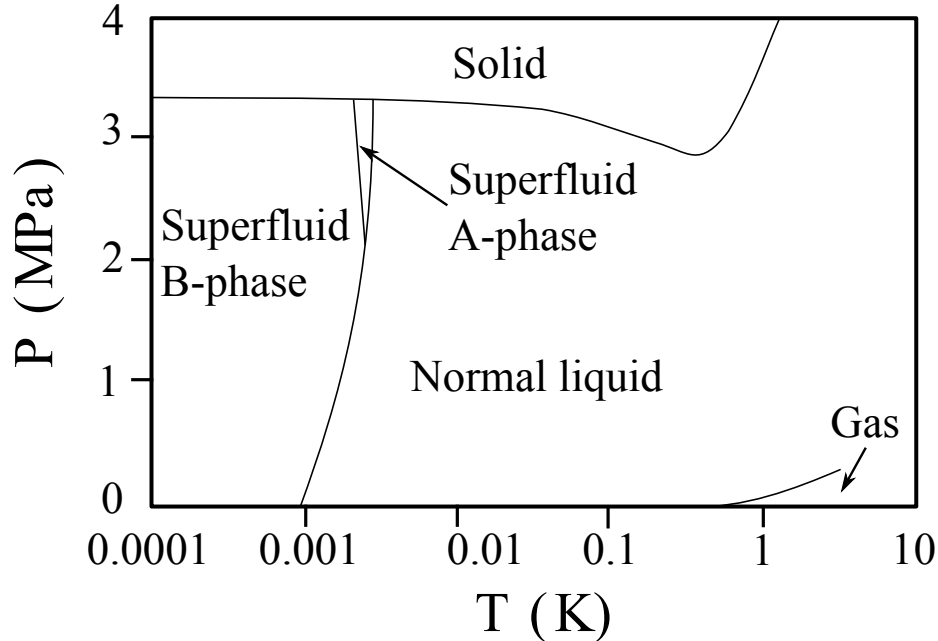
Figure 3.1: Pressure-temperature phase diagram of ^{3}He at zero magnetic field.

for pressures below 30 bar. Further cooling the liquid, ^{3}He becomes more and more viscous. The reduction of the distance between the atoms increases the strength of van der Waals interactions. At temperatures below 300 mK, ^{3}He behaves as a strongly interacting Fermi liquid. At temperatures of approximately 1 mK ^{3}He undergoes a second-order phase transition into the superfluid state. The phase transition between the A and B superfluid phases is of first-order. The superfluid ^{3}He phase diagram is discussed in more detail in section 3.2.

3.1.1 ^{3}He-^{4}He mixture

One of the unique features of ^{3}He is its finite solubility in ^{4}He. With decreasing temperature a mixture of ^{3}He-^{4}He undergoes a phase separation (see figure 3.2). The result of this phase separation are two phases: a dilute and a concentrated
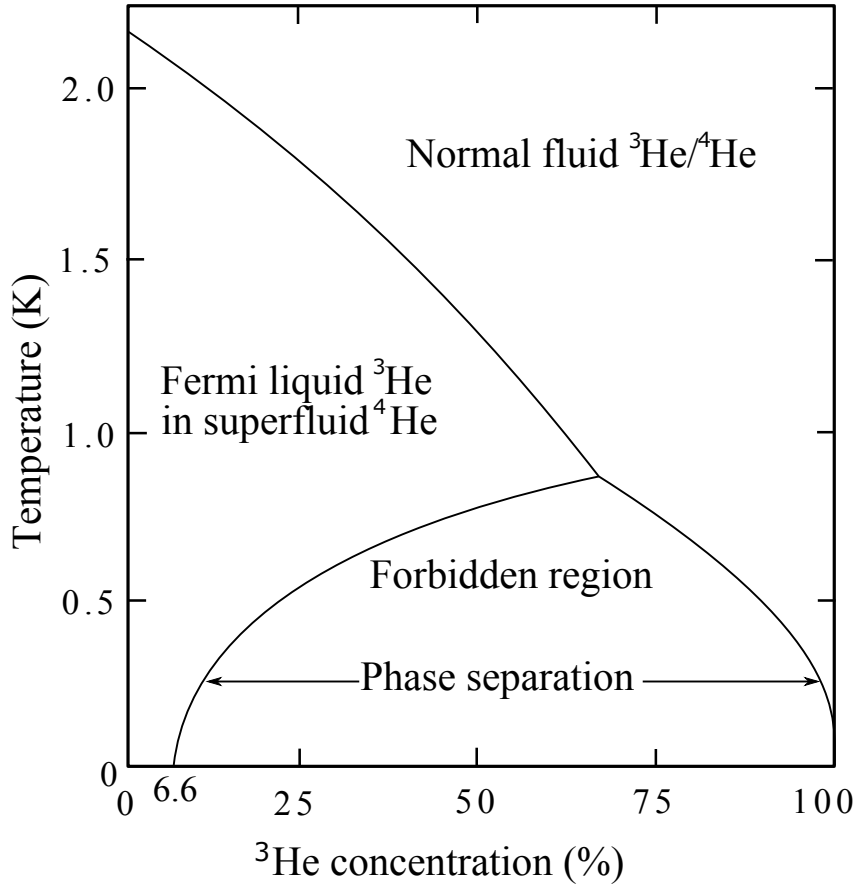
Figure 3.2: Concentration-temperature phase diagram of liquid ^{3}He-^{4}He mixture.

phase of ^{3}He. By further lowering the temperature, the difference in concentrations of ^{3}He between these phases increases. The temperature dependence of the concentration of ^{3}He on temperature in the dilute phase (left side of the phase diagram) can be expressed as [26]

$$x_3 = 0.066(1 + 8.3T^2). \tag{3.1}$$

Thus, at $0\,\mathrm{K}$ the dilute phase will contain about 6.6% of ^{3}He. This property of ^{3}He-^{4}He mixtures is used as the main source of cooling in all dilution refrigerators (see experimental methods section 4.1). The concentration of ^{4}He in the concentrated

phase (right side of the phase diagram) depends on temperature as [26]

$$x_4 = 0.85T^{3/2}e^{-0.56/T}. \tag{3.2}$$

As follows from equation (3.2) at low temperatures the concentrated phase will consist of essentially pure ^{3}He. As all our experiments are performed in the microkelvin regime, the ^{3}He experimental sample can be considered as an almost absolutely pure substance (at temperature of $1\,\text{mK}$ the concentration of ^{4}He in the concentrated phase is already on the order of 10^{-248}). It is worth mentioning at this point that there are attempts being made to achieve superfluid ^{3}He in a mixture of ^{3}He-^{4}He [27].

3.2 Superfluid ^{3}He

At temperatures around $1\,\text{mK}$, depending on the pressure, ^{3}He undergoes a second-order phase transition to the superfluid state. This transition is linked with spontaneous breaking of three symmetries: orbital, spin, and gauge symmetry.

Unlike ^{4}He, ^{3}He atoms are fermions, so they cannot undergo direct Bose-Einstein condensation to form a superfluid. How does the ^{3}He form the superfluid? To answer this question in a general way we can take a look at the related phenomenon of superconductivity. Electrons are fermions and while undergoing a phase transition to the superconducting state, with the aid of the electron-phonon interaction, they form Cooper pairs. This process is very well described by the theory developed by Bardeen, Cooper, Schrieffer (BCS theory) [17, 28]. The fundamental idea is that there is a weak coupling interaction between electrons via phonon exchange. This interaction becomes significant at temperatures where the thermal energy of the electrons is comparable with the energy of the electron-phonon interaction. In an intuitive picture, an electron moving through a lattice attracts the nearby positive ions of the atomic nuclei. This attraction slightly displaces these ions bringing them closer together, forming an increase in positive

charge. This leads to an enhanced attraction on a second electron moving on a similar trajectory. The moving ions of the lattice are described by a momentum wave-vector i.e. a phonon. The energy of the two electrons forming the pair is reduced by a binding energy. This reduction of energy compresses the density of states around the Fermi energy giving rise to an energy gap Δ (2Δ is the energy needed to break a Cooper pair). A similar intuitive picture can be applied to superfluid ^{3}He. However, the mechanism of Cooper pair creation is different. When the temperature reaches the transition temperature, the atoms of ^{3}He start forming Cooper pairs. Since atoms of ^{3}He are magnetic, a moving ^{3}He atom attracts other ^{3}He atoms and leaves a magnetic disturbance in its wake. Instead of a phonon mediating the interaction between the particles forming Cooper pairs it is now a paramagnon. Paramagnons are long-lived long-range spin fluctuations [29]. Creation of the Cooper pairs gives rise to an energy gap $\Delta(T)$ in the energy spectrum. This gap separates the Cooper pairs (ground state) from unpaired excitations.
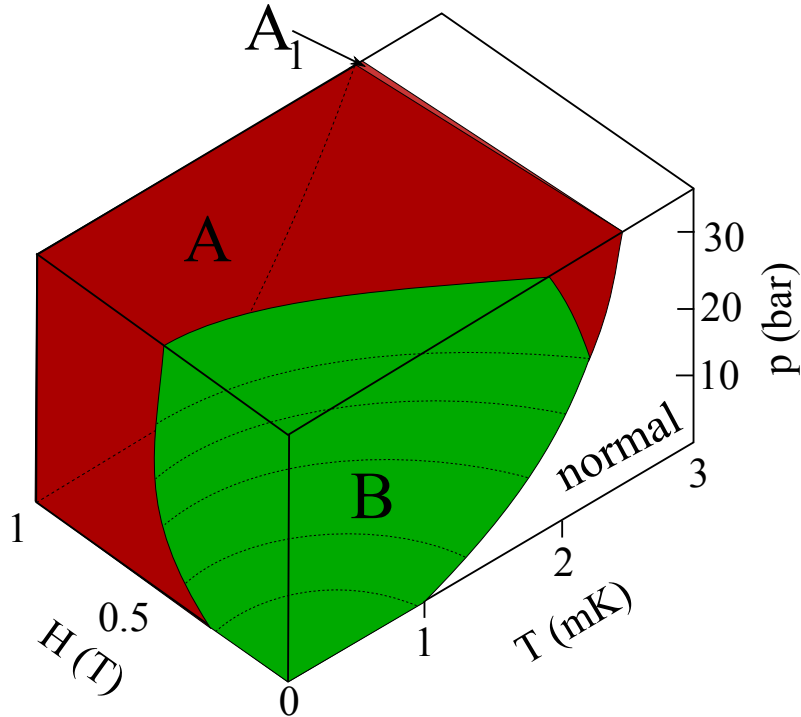
Figure 3.3: Pressure-temperature-magnetic field phase diagram for superfluid ^{3}He.

A detailed picture of superfluid ^{3}He is more complicated. First, the ^{3}He atoms create Cooper pairs with orbital momentum (L=1). In a simple classical picture it is easy to imagine the Cooper pair atoms revolving about their centre of mass. Secondly, the spin of the Cooper pair is equal to one (S=1) in order to preserve the antisymmetry of the fermionic wavefunction, and thus superfluid ^{3}He has magnetic properties. Thirdly, the orbital and spin momenta of the pair are coupled via a dipole-dipole interaction. This type of pairing is called "spin triplet p-wave pairing".

The phase diagram for temperatures below $3\,\mathrm{mK}$ is shown in figure 3.3. From the phase diagram it is clear that there are two main phases of superfluid ^{3}He. The B phase occupies the low temperature and low field region. The high magnetic field and high temperature region is dominated by the A phase. The phase transition from the superfluid A to B phase is of first order and has an associated latent heat. The last visible phase on this diagram is the A_1 phase. This phase exists only in high temperatures and in magnetic field.

For the spin-triplet configuration we can write the wave-function in the form [20, 30, 29]

$$\Psi(\boldsymbol{k}) = \Phi_{\uparrow\uparrow}(\hat{k})|\uparrow\uparrow\rangle + \Phi_{\downarrow\downarrow}(\hat{k})|\downarrow\downarrow\rangle + \frac{1}{\sqrt{2}}\Phi_{\uparrow\downarrow}(\hat{k})(|\uparrow\downarrow\rangle + |\downarrow\uparrow\rangle), \qquad (3.3)$$

where $\hat{k}$ is a unit vector in momentum-space, and $\Phi_{\uparrow\uparrow}(\hat{k})$, $\Phi_{\downarrow\downarrow}(\hat{k})$ and $\Phi_{\uparrow\downarrow}(\hat{k})$ are amplitudes of the spin sub-state operators determined by the projection $|\uparrow\uparrow\rangle$, $|\downarrow\downarrow\rangle$ and $(|\uparrow\downarrow\rangle + |\downarrow\uparrow\rangle)$ on the z-axis. As this wave function accounts for all three elements of the spin projections it describes the B phase of superfluid ^{3}He. For a more detailed description see section 3.2.2.

The A phase does not contain Cooper pairs with zero spin projection. The wave function for the A phase is expressed as

$$\Psi(\boldsymbol{k}) = \Phi_{\uparrow\uparrow}(\hat{k})|\uparrow\uparrow\rangle + \Phi_{\downarrow\downarrow}(\hat{k})|\downarrow\downarrow\rangle, \qquad (3.4)$$

For a more detailed description see section 3.2.1.

As mentioned earlier the A_1 phase exists only in high temperatures and magnetic fields. This phase consists only of the condensate component with spin projection $|\uparrow\uparrow\rangle$. The wave function can be written

$$\Psi(\boldsymbol{k}) = \Phi_{\uparrow\uparrow}(\hat{k})|\uparrow\uparrow\rangle. \tag{3.5}$$

Recent experiments suggest a fourth stable superfluid phase, the "polar" phase, present in confined geometry [4]. The energy gap of this phase has a line of zeroes along the equator.

Generally from BCS theory the order parameter can be written in the form

$$\Psi_{\nu\mu}(\hat{k}) = \left\langle \hat{a}_\nu(\hat{k})\hat{a}_\mu(-\hat{k}) \right\rangle, \tag{3.6}$$

where $\hat{a}_{\nu,\mu}$ are annihilation/creation operators for the wave vector $\hat{k}$ and ν, μ denote the spin state. For superfluid ^{3}He we have spin-triplet pairing, therefore the order parameter in spin space becomes a 2x2 matrix of the form

$$\Psi(\hat{k}) = \begin{pmatrix} \Psi_{\uparrow\uparrow} & \Psi_{\uparrow\downarrow} \\ \Psi_{\downarrow\uparrow} & \Psi_{\downarrow\downarrow} \end{pmatrix}. \tag{3.7}$$

Usually the order parameter is expressed in vector form. Any 2x2 matrix can be expressed as

$$i\hat{\sigma}_y(d_0\mathbf{I} + \boldsymbol{\sigma}.\mathbf{d}), \tag{3.8}$$

where $\mathbf{d} = (d_x, d_y, d_z)$ is a complex vector, d_0 is a scalar, $\mathbf{I}$ is a unitary matrix and $\boldsymbol{\sigma} = \mathbf{e}_x\hat{\sigma}_x + \mathbf{e}_y\hat{\sigma}_y + \mathbf{e}_z\hat{\sigma}_z$; $\hat{\sigma}_x$, with $\hat{\sigma}_y$ and $\hat{\sigma}_z$ being the Pauli matrices. The first component corresponds to singlet pairing, while the second component corresponds

to triplet pairing. Using this the order parameter can be rewritten

$$\Psi(\boldsymbol{k}) = \begin{pmatrix} 0 & d_0 \\ -d_0 & 0 \end{pmatrix} + \begin{pmatrix} -d_x(\hat{k}) + id_y(\hat{k}) & d_z(\hat{k}) \\ d_z(\hat{k}) & d_x(\hat{k}) + id_y(\hat{k}) \end{pmatrix}. \tag{3.9}$$

As mentioned earlier the first matrix corresponds to spin singlet pairing and we will not consider it further. Next if we assume that $\Psi(\hat{k})$ is a unitary matrix, we can determine the meaning of vector $\mathbf{d}(\hat{k})$

$$\left| \mathbf{d}(\hat{k}) \right|^2 = \frac{1}{2} Tr[\Psi(\hat{k})\Psi^\dagger(\hat{k})], \tag{3.10}$$

where Tr denotes the trace of the matrix and $\Psi^\dagger(\hat{k})$ is the matrix Hermitian conjugate. From equation (3.10) we see that the absolute value of $\mathbf{d}(\hat{k})$ is in fact the amplitude of spin triplet pairing at every point on the Fermi surface. This amplitude is proportional to the size of the energy gap Δ on the Fermi surface. Furthermore, for any orientation of $\hat{k}$ on the Fermi surface, $\mathbf{d}(\hat{k})$ points in the direction in which Cooper pairs have zero spin projection. In other words $\mathbf{d}(\hat{k})$ is perpendicular to the spin vector.

Orbital pairing in the state with $L = 1$ leads to three possible projections in orbital space. The components of vector $\mathbf{d}$ (d_x, d_y, d_z) are linear functions of vectors $\mathbf{k}(k_1, k_2, k_3)$, in momentum space giving

$$d_i(\hat{k}) = \sum_{\rho=1}^{3} A_{i\rho}(\hat{k})_\rho, \tag{3.11}$$

where $i = x, y, z$ and $A_{i\rho}$ is the order parameter in the form of a complex 3x3 matrix. This gives 9 independent complex functions giving 18 degrees of freedom and the possibility of existence of more than 4 superfluid ^{3}He phases.

Next we will examine the order parameters of the superfluid ^{3}He-A and ^{3}He-B phases.

3.2.1 ^{3}He-A
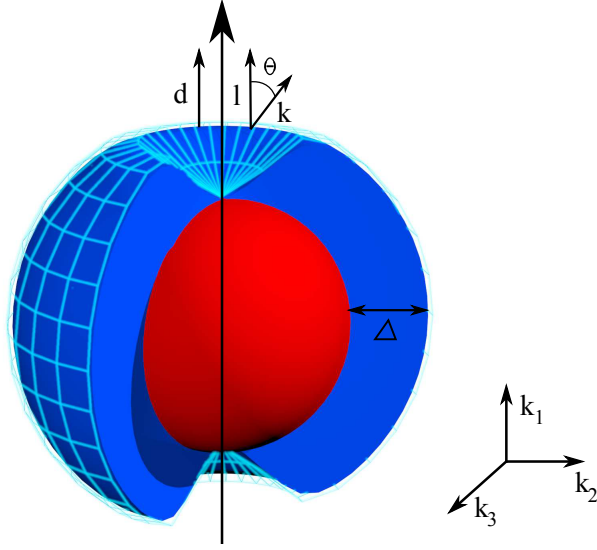
Figure 3.4: A-phase energy gap with two Fermi points. E_F is coloured red. Δ and E_F are not to scale.

The A phase is described as the ABM state, a state suggested by Anderson, Brinkman and Morel [31]. As previously mentioned, the absence of the $(|\uparrow\downarrow\rangle+|\downarrow\uparrow\rangle)$ component in the Cooper pairs of the A phase leads to anisotropy in the energy gap for quasiparticle excitations. In the A phase, vector $\mathbf{d}$ has the same direction for all vectors $\mathbf{k}$. The order parameter matrix $A_{i\rho}$ can then be written in the form

$$A_{i\rho} = \sqrt{\frac{3}{2}}\Delta \hat{d}_i(\hat{n}_{1\rho} + i\hat{n}_{2\rho}), \tag{3.12}$$

where $\hat{n}_1, \hat{n}_2$ are orthogonal unit vectors in k space and Δ is the temperature dependent scalar value of the energy gap. The vector of the orbital angular momentum of the Cooper pair has the same direction as a unit vector $\hat{l}$ defined as $\hat{l} = \hat{n}_1 \times \hat{n}_2$. In the A phase the vectors $\hat{d}$ and $\hat{l}$ are parallel.

This is represented in figure 3.4. The energy gap Δ is reduced to zero where vectors $\hat{k}$ and $\hat{l}$ are parallel. For the magnitude of the energy gap Δ we can write

$$\Delta(\hat{k}) = \Delta_0 \sin(\Theta_k), \tag{3.13}$$

where Θ_k is the angle between vectors $\hat{k}$ and $\hat{l}$ and $\Delta_0 = 2.02 k_B T_c$. The anisotropic gap leads to an easy excitation generation in two directions (the direction of the poles where the gap is supressed to 0).

3.2.2 ^{3}He-B

The B-phase is known as the BW state named after Balian and Werthamer[32]. By having all possible spin and angular momentum projections, the energy gap (the order parameter) is isotropic in k-space, as shown in figure 3.5. For the magnitude of the energy gap of the B phase we can write

$$\Delta_{BW} = 1.76 k_B T_c. \tag{3.14}$$
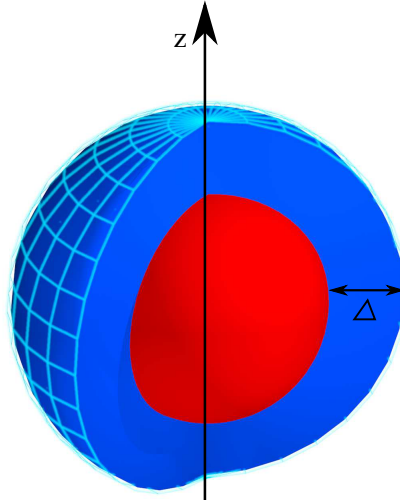
Figure 3.5: Fully isotropic energy gap of B phase in zero magnetic field.

However, BW theory describes a p-wave pairing superconductor and does not take into account the magnetic dipoles present in ^{3}He atoms. While these spin orbit interactions are missing the vector of orbital angular momentum can have any orientation to the spin vector, therefore the ground state is degenerate. Recalling equation (3.11) we can express the components of vector $\mathbf{d}$ as follows

$$d_i(\hat{k}) = \sum_{\rho=1}^{3} A_{i\rho}(\hat{k})_\rho = \Delta e^{i\Theta} \sum_{\rho=1}^{3} R_{i\rho} \hat{k}_\rho, \tag{3.15}$$

22

where $R_{i\rho}$ are the elements of rotation matrix R, which determines coupling between the spin coordinates and the orbital coordinates via an angle Θ around an arbitrary rotational axis $\hat{n}$. As shown by Leggett [33] the dipole energy is minimised when the angle between the spin and angular momentum is 104°. Upon condensing into the superfluid this preferential orientation of the two vectors is known as spin-orbit symmetry breaking.

Applying an external magnetic field results in the energy gap of ^{3}He-B becoming distorted (figure 3.6). The gap is suppressed in the direction of the magnetic field.
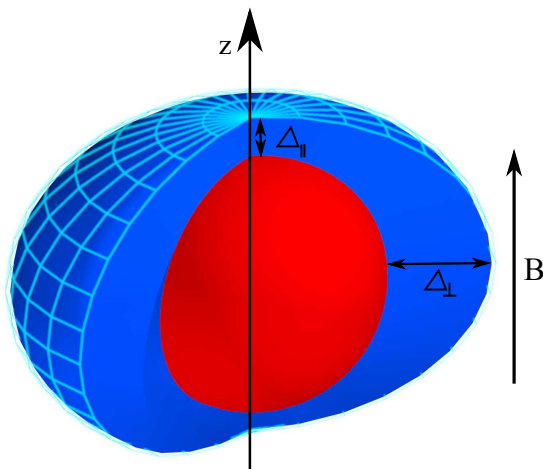
Figure 3.6: Energy gap of B phase in magnetic field.

The field is suppressing $(|\uparrow\downarrow\rangle + |\downarrow\uparrow\rangle)$ pairs due to their zero magnetic susceptibility. Zeeman splitting of $\downarrow$ and $\uparrow$ puts each component of these Cooper pairs at different energies. This reduces the energy gap in the direction these pairs reside $\Delta_{||}$. However, Zeeman splitting increases the binding energy of the remaining two types of Cooper pairs, which is seen as a slight increase in energy gap around the equator $\Delta_{\perp}$ (see figure 3.9). At fields above 0.5 T the system undergoes first-order transition into ^{3}He-A phase.

3.3 Excitation dynamics in ^{3}He-B

In order to explain the dynamics of quasiparticle excitations in ^{3}He-B we have to start from the dispersion relations. For the total amount of particles N in the

system of volume V one can write

$$N = V \int_0^\infty f(E)g(E)dE, \qquad (3.16)$$

where $f(E)$ is the Fermi distribution function and $g(E)$ is the density of states. At $T = 0\,\mathrm{K}$, all available states up until the Fermi energy are filled, so $f(E)=1$ if $E < E_F$ and $f(E)=0$ if $E > E_F$. Then equation (3.16) can be rewritten

$$N = V \int_0^{E_F} g(E)dE. \qquad (3.17)$$

For the energy itself we can write

$$E = \frac{p^2}{2m}, \qquad (3.18)$$

where m is the mass of the ^{3}He atom. The dispersion curves take the form shown in figure 3.7. Excitations occur only when particles within $k_B T$ (when $k_B T << E_F$)
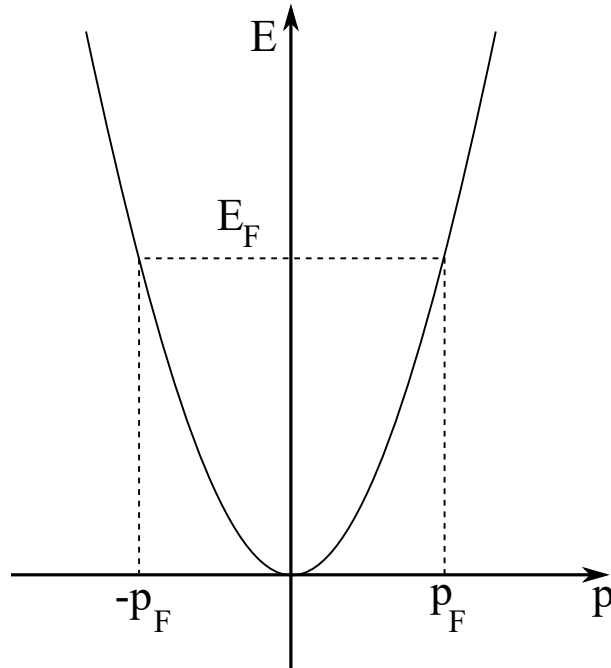
Figure 3.7: Dispersion curve for 1-D non-interacting fermions.

of the Fermi energy are excited to higher available energy states. However, at

temperatures below approximately $100\,\text{mK}$ corrections are necessary to account for Fermi liquid interactions in ^{3}He. Atoms of ^{3}He are replaced with an equal amount of quasiparticles, each with effective mass m_{ex}, and identical spin and angular momentum as the original ^{3}He atom. The effective mass accounts for the mass of the helium atom itself and its interactions with the surrounding particles.

In superfluid ^{3}He-B with an isotropic energy gap the energy of excitations is given by

$$E = \sqrt{\epsilon^2(p) + \Delta^2}. \tag{3.19}$$

here Δ is the energy gap and $\epsilon(p)$ is the energy of excitation relative to the Fermi energy,

$$\epsilon(p) = \frac{p^2}{2m_{ex}} - E_F. \tag{3.20}$$

Thus, the momentum is

$$p = \sqrt{2m_{ex}(\epsilon(p) + E_F)}. \tag{3.21}$$
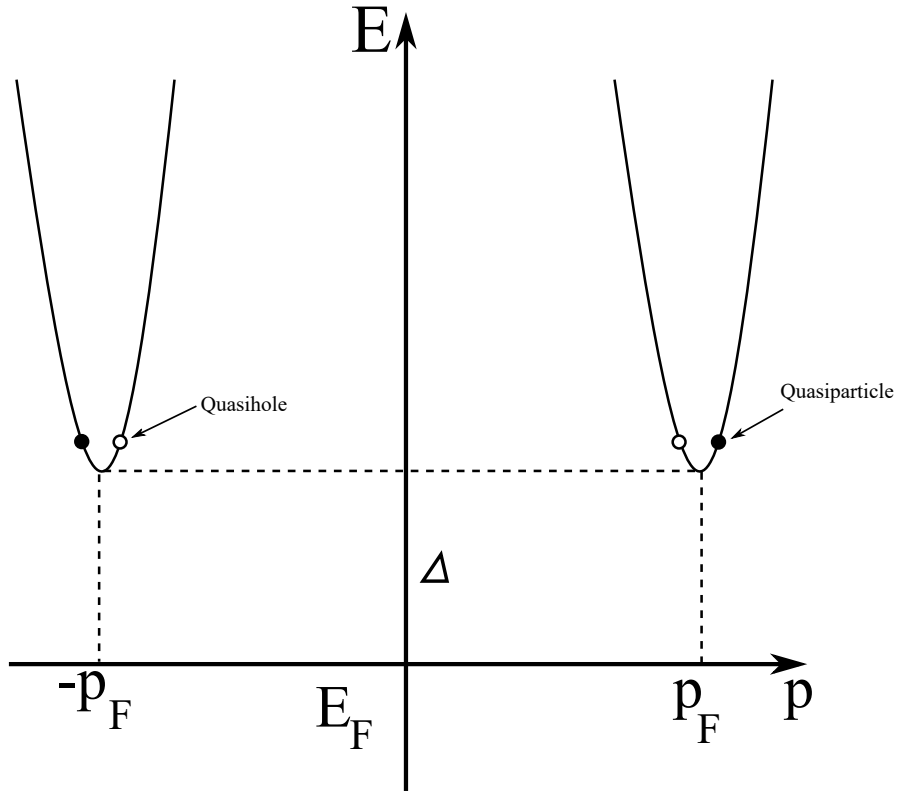
Figure 3.8: Dispersion curves of superfluid ^{3}He-B relative to the Fermi energy.

Substituting for $\epsilon(p)$ from equation (3.19) we get to the final form of the momentum of excitations

$$p_{qp} = \sqrt{2m_{ex}(E_F + \sqrt{E^2 - \Delta^2})}, \tag{3.22}$$

$$p_{qh} = \sqrt{2m_{ex}(E_F - \sqrt{E^2 - \Delta^2})}, \tag{3.23}$$

where the subscripts "qp" denotes quasiparticles and "qh" quasiholes, the two types of excitations in superfluid ^{3}He-B. While quasiparticles have their group velocity in the direction of their momentum, quasiholes have group velocity in the opposite direction to their momentum. The action of the quasiparticles is manifested as pressure acting on a solid wall (they push), while quasiholes exert traction (they pull). The dispersion curves are shown in figure 3.8.

As previously mentioned when an external magnetic field is applied to the ^{3}He-B, the energy gap becomes distorted. This changes the dipersion curves for both types of pairing with spin projections $S_z = \pm 1$ and $S_z = 0$. The dispersion curves for all three types of pairings of ^{3}He-B in magnetic field are shown in figure 3.9.
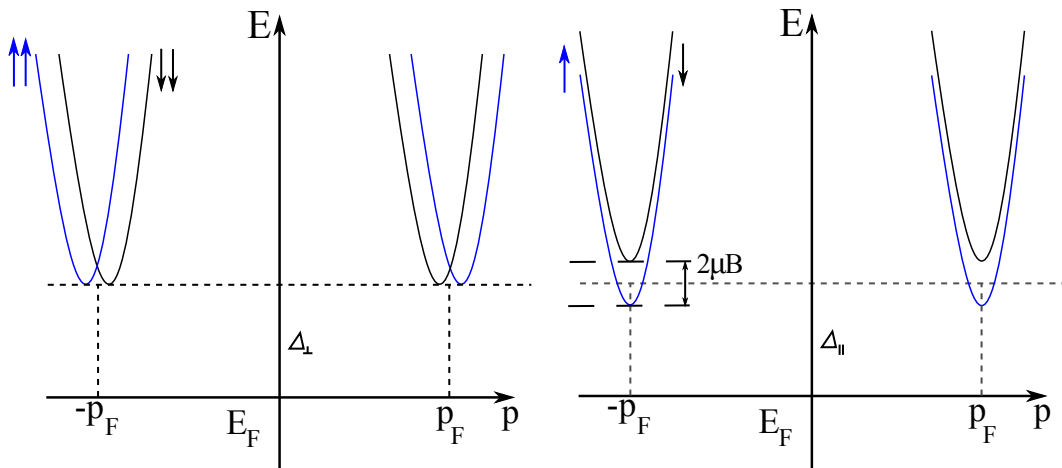
Figure 3.9: The dispersion curves of ^{3}He-B in an external magnetic field along the z direction as seen in figure 3.6.

At ultra-low temperatures ($T < 0.25T_C$) the mean free path of excitations becomes bigger than any dimension of our experimental cell (at these temperatures the mean free path is on the order of centimetres). In this regime a single excitation will move through the experimental cell without interacting with any other excitation until it scatters off the walls of the cell. In these conditions it is more convenient to consider the flux of excitations. For the number of quasiparticles excited above the energy gap Δ we can write

$$N_{(ex)} = V \int_{E_F+\Delta}^{\infty} g(E)f(E)dE. \qquad (3.24)$$

Then the total excitation flux through a unit area and unit time is given by

$$\langle nv_g \rangle = \int_{E_F+\Delta}^{\infty} v_g g(E)f(E)dE. \qquad (3.25)$$

At first glance this is the complete derivation of excitation flux, however the density of energy states $g(E)$ in a superfluid is a discontinuous function (figure 3.10). As mentioned earlier, entering the superfluid state gives rise to an energy gap which effectively introduces a forbidden region in energy where no states are available. However, the density of momentum states is a continuous function of energy so
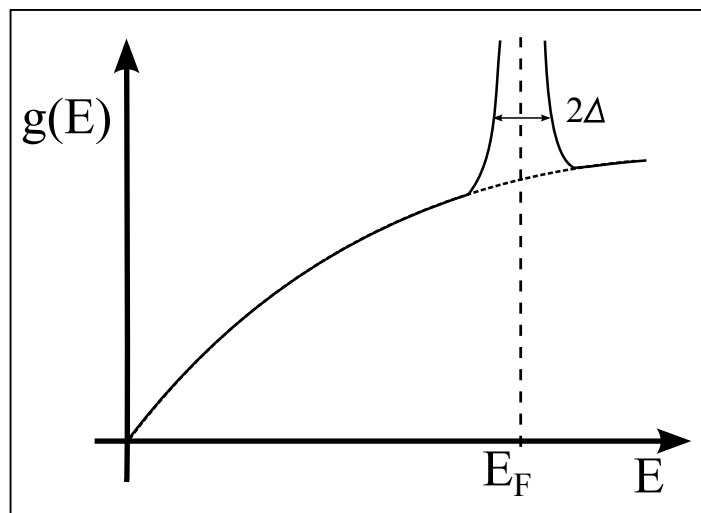
Figure 3.10: Density of energy states as a function of energy. Δ is the energy gap around E_F.

27

utilising

$$g(E)dE = g(p)dp, \tag{3.26}$$

where $g(p)$ is the density of momentum states, gives

$$g(E)v_g = g(p), \tag{3.27}$$

where $v_g = dE/dp$ is the group velocity. At ultra-low temperatures, the momentum of excitations is very close to the Fermi momentum so we can assume

$$g(E)v_g = g(p) = g(p_F) = g(E_F)v_F \tag{3.28}$$

where v_F is the Fermi velocity. Equation (3.25) then becomes

$$\langle nv_g \rangle = g(E_F)v_F \int_{E_F+\Delta}^{\infty} f(E)dE, \tag{3.29}$$

with the Fermi distribution function

$$f(E) = \frac{1}{e^{\frac{E-E_F}{k_BT}} + 1}. \tag{3.30}$$

At ultra-low temperatures when $E >> k_BT$ this simplifies to

$$f(E) = e^{-\frac{E-E_F}{k_BT}}. \tag{3.31}$$

Combining equations (3.29) and (3.31) we get

$$\langle nv_g \rangle = g(E_F)v_F k_B T e^{-\frac{\Delta}{k_BT}}. \tag{3.32}$$

The importance of knowing the excitation flow is two-fold. First, it allows us to calculate the "pressure" or force exerted by excitations on the walls of the container or any measurement object. Secondly, since the flux depends on temperature, by measuring the flux of excitations we can determine the temperature of the

superfluid.

3.4 Quasiparticle damping force

As mentioned in the previous section the excitations interact only with the walls
or macroscopic objects in their path. In this section I will describe the force that
comes from these interactions.
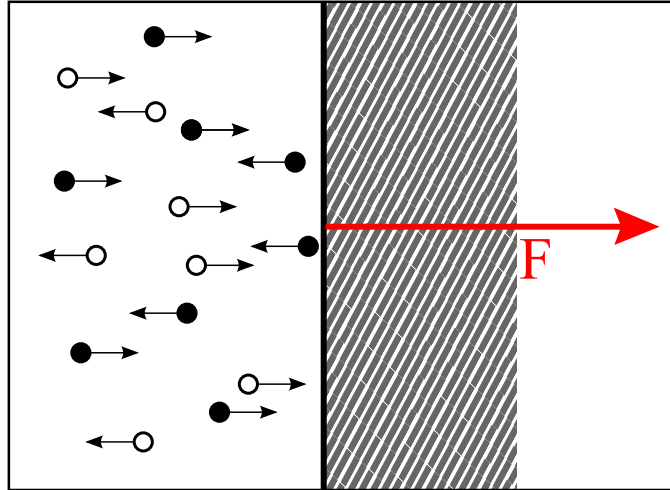
Figure 3.11: Quasiparticles (full circles) and quasiholes (empty circles) moving
at velocity v_g (arrows), interacting with a solid stationary wall .

First, we consider a one-dimensional model where excitations interact with
a stationary solid wall (figure 3.11). The force exerted on the wall by these
excitations is given by

$$\mathbf{F} = \frac{d\mathbf{p}}{dt}. \tag{3.33}$$

The total change in momentum of an excitation after scattering on the wall is
equal to $2\mathrm{p}_F$ assuming that the wall surface is specular. Considering the geometry
of the system for the force acting on the wall one can write

$$F = 2p_F \left\langle nv_g \right\rangle A\frac{1}{2}, \tag{3.34}$$

where A is the wall surface and $\langle nv_g \rangle$ is the excitation flux as mentioned in the
previous section (equation (3.32)), and the factor $\frac{1}{2}$ corresponds to the quasi-static

approximation that half of all excitations are heading towards the wall. In order to account for both quasiparticle and quasihole excitations, equation (3.32) must be multiplied by 2 giving the final form for excitation flux in ^{3}He-B

$$\langle n v_g \rangle = 2g(E_F) v_F k_B T e^{-\frac{\Delta}{k_B T}}. \tag{3.35}$$

In the next part we will show the damping force coming from excitations on moving object through the superfluid. We expect this force to be small because of the exponential factor and the relatively slow motion of the object compared with v_F. Let us consider an infinitely large paddle moving at a speed v through superfluid ^{3}He-B. The superfluid is pushed by this paddle and it flows with a velocity of $v_s = v$ with the paddle. Close to the paddle where the superfluid is moving, the dispersion curves shift due to Galilean transformations by $\pm p_F v$, however, in the bulk liquid the superfluid is static. The situation is illustrated in figure 3.12 [34]. Lets consider 4 possible channels from which excitations can approach the paddle (as illustrated on figure 3.12. Channel 1 and 4 belong to quasiholes approaching from in front and behind the paddle, respectively. Channels 2 and 3 correspond to quasiparticles approaching from in front and behind the paddle, respectively. The total force acting on the paddle is a sum of damping
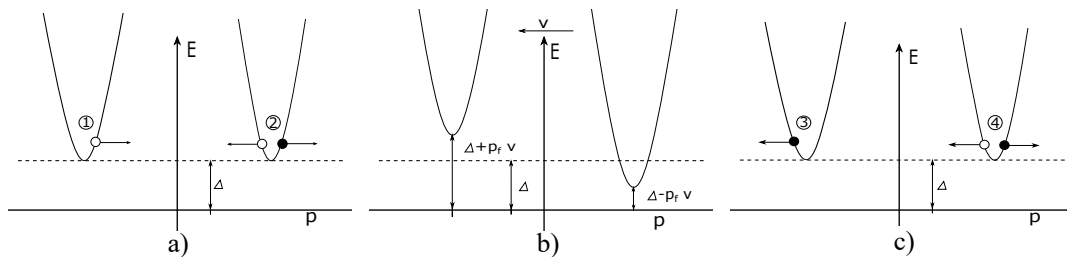
Figure 3.12: Dispersion curves in three different positions, a) in front of the paddle in the bulk liquid, b) on the paddle, c) behind the paddle in the bulk liquid. The numbers label channels of excitations (quasiparticles and quasiholes alike) heading towards the paddle.

forces coming from all four channels [35],

$$F_{TH} = F_1 + F_2 + F_3 + F_4. \tag{3.36}$$

Low energy excitations can interact with the paddle only from channels F_2 and F_4 as there are free low energy states available by the wire surface.

$$F_2 = F_4 = 2p_F \langle n v_g \rangle A \frac{1}{2}. \tag{3.37}$$

For channels F_1 and F_3 only high energy excitations, with energy greater than $\Delta + p_F v$, can contribute to the total damping on the paddle. Let us consider a quasihole with energy $\Delta < \Delta + p_F v$ approaching the paddle from channel 1. When it is approaching the paddle and the superfluid flow, then from energetic point of view, the quasihole is moving towards a region of increasing gap (as illustrated in figure 3.13).
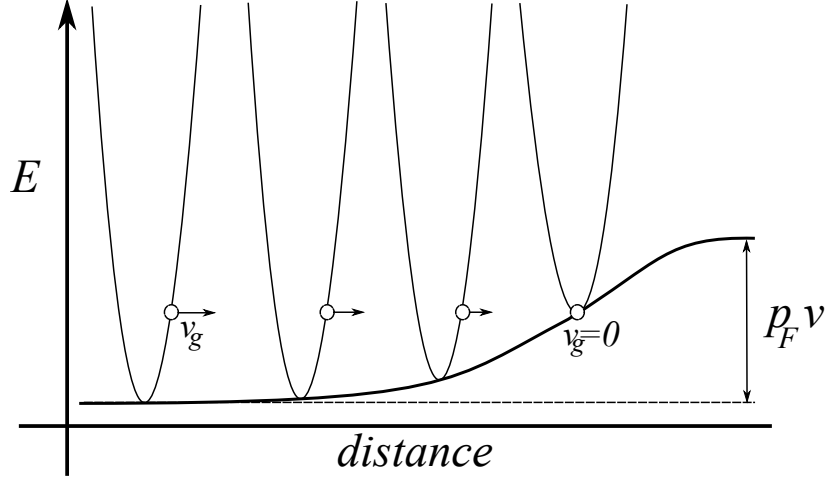
Figure 3.13: Quasihole moving towards a region of increasing potential.

With increasing potential the quasihole's group velocity is going to decrease until $v_g = 0$. The quasihole's energy is not high enough to cross the potential. At this moment the quasihole is replaced by a quasiparticle coming from a broken Cooper pair from the condensate. The created quasiparticle has the same momentum as the quasihole did, but its group velocity has opposite direction. This

process is known as Andreev reflection [36]. It is important to note that the change in momentum is insignificant, of the order of $(\Delta/E_F)p_F \approx 10^{-3}p_F$, therefore the damping force arising from Andreev reflection is negligible and excitations undergoing this process do not contribute to the total damping on the paddle. For channel F_1 we can write

$$F_1 = F_3 = -2p_F A \frac{1}{2} \int_{\Delta+p_F v}^{\infty} g(E)f(E)v_g dE, \qquad (3.38)$$

noting that only excitations with energies above $\Delta + p_F v$ contribute to damping. Using the same identities as in equation (3.25) we can rewrite this equation

$$F_1 = F_3 = -p_F A g(E_F)v_F \int_{\Delta+p_F v}^{\infty} f(E)dE, \qquad (3.39)$$

and integrate to get

$$F_1 = F_3 = -p_F A g(E_F)v_F k_B T e^{-\frac{\Delta+p_F v}{k_B T}}. \qquad (3.40)$$

Combining equations (3.37) for forces F_2 and F_4 and (3.40) for F_1 and F_3 with equation (3.36) we get

$$F_{TH} = 2p_F A g(E_F)v_F k_B T e^{-\frac{\Delta}{k_B T}}\left(1 - e^{-\frac{p_F v}{k_B T}}\right). \qquad (3.41)$$

This equation describes the thermal damping force of ballistic excitations. The presented simplified theory considers only 1D system. In order to consider real 3 dimensional situations we introduce dimensionless constants λ and γ, where γ is a geometrical factor that takes account the geometry and specularity of the scattering surface, and λ takes account averaging of dispersion curves over all possible scattering angles around the paddle. Both constants are on the order of unity. With this in mind equation (3.41) becomes

$$F_{TH} = \gamma 2p_F A \langle nv_g \rangle \left(1 - e^{-\frac{\lambda p_F v}{k_B T}}\right). \qquad (3.42)$$

In this work we will call this force the thermal damping force exerted on an object by ballistic excitations.

Chapter 4

Experimental methods

4.1   Dilution refrigerators

Dilution refrigerators have been around for a significant amount of time cooling down various experiments or devices to millikelvin temperatures. The first prototypes were made in 1965 [37]. A schematic of a typical dilution fridge is shown in figure 4.1. A mixture of ^{3}He and ^{4}He is used to cool down to millikelvin temperatures. As mentioned earlier in section 3.1.1 at temperatures below $900\,\mathrm{mK}$, the mixture undergoes phase separation into the dilute (high entropy) and concentrated phases (low entropy). The main cooling happens inside the mixing chamber, where the phase boundary is established. Here ^{3}He from the concentrated phase is "evaporating" into the dilute phase. The ^{3}He atom gains entropy while crossing the boundary from the concentrated into the dilute phase. In doing so the atoms absorb energy from surroundings which causes cooling. The "evaporation" rate is driven by heating the still to allow pumping of ^{3}He gas. For the cooling power of a dilution fridge we can write [26, 38, 37, 39]

$$\dot{Q} = \dot{n}_3(H_d(T) - H_c(T)) = 84\dot{n}_3T^2, \tag{4.1}$$

where $\dot{n}_3$ is the molar circulation rate of the ^{3}He atoms (determined by the pumping rate) and H_d, H_c are the enthalpies of the dilute and concentrated phases, respectively. The pumped out ^{3}He gas is then returned to the system via the ^{4}He pot where it is condensed into liquid again. This liquid ^{3}He is then pre-cooled by the continuous and discrete heat exchangers prior to entering the mixing chamber. Heat exchangers, as the name suggests, are components that exchange heat between the incoming hot fluid into the mixing chamber with the out-going cold fluid from the mixing chamber. With this, the returning fluid is pre-cooled to low temperatures. The discrete heat exchanger consists of two silver sinter "biscuits" glued to a thin silver foil all enclosed in metal casing. The silver biscuits are made by pressing very fine silver powder in a pre-made former. The silver biscuits provide a large surface area for the fluid to cool and the silver foil

separates the concentrated and the dilute phases (hot and cold).
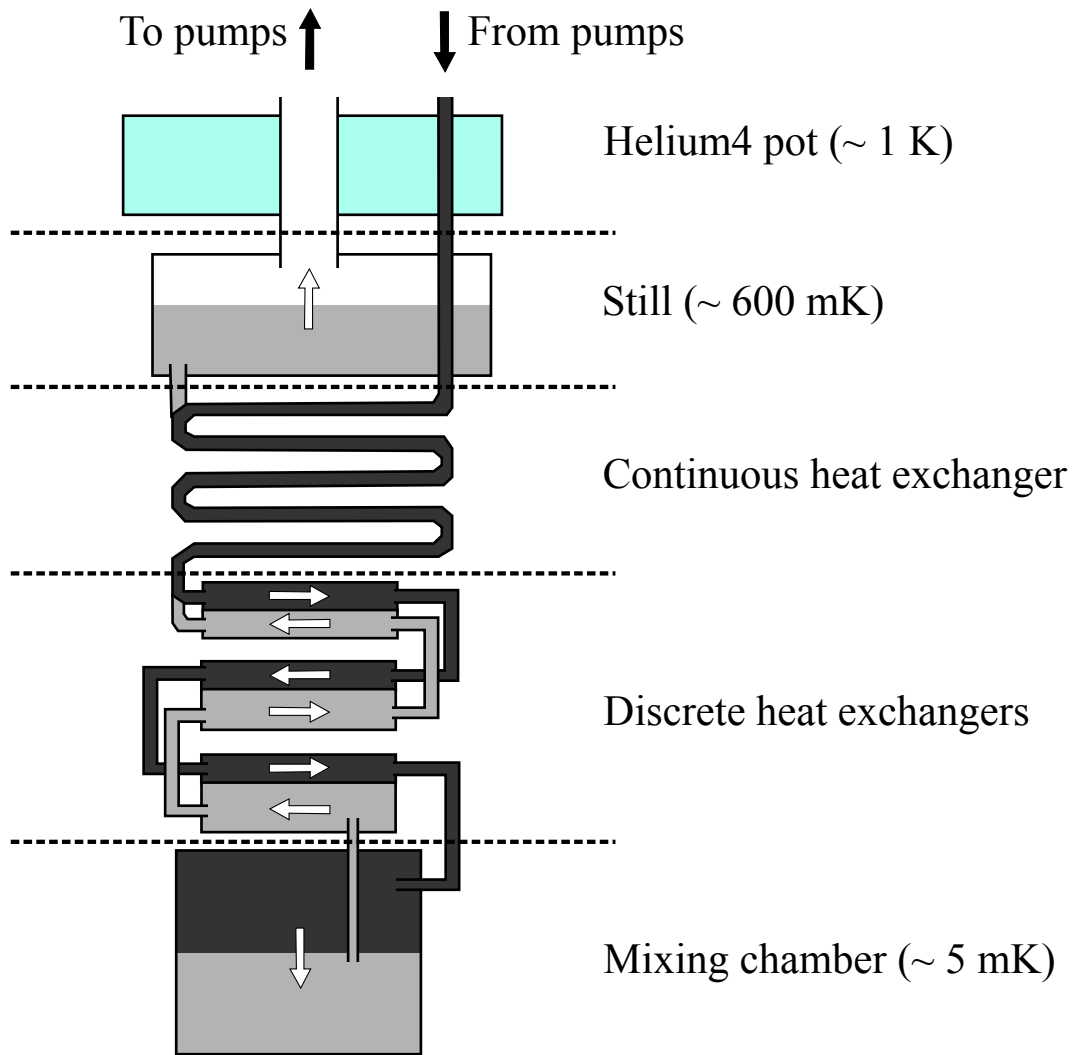
Figure 4.1: Dilution refrigerator schematic. The [3]He rich phase is in dark grey and the dilute phase is in light grey.

The Lancaster dilution fridges are all built in-house. The experiments presented in this work were performed using an experimental cell mounted on the mixing chamber of a dilution refrigerator first installed in 1978. The dilution refrigerator is placed within a double vacuum dewar vessel. Liquid nitrogen is used within the shell of the dewar to shield the refrigerator from thermal radiation. The inner volume also known as the main bath, is filled with liquid [4]He. The main bath also contains the dilution refrigerator itself placed within the inner vacuum chamber (IVC) and the main magnet attached to the bottom of the IVC. The experimental

cell is connected to the mixing chamber of the dilution refrigerator within the IVC and is shielded by two more radiation shields thermally anchored at $600\,\text{mK}$ and $20\,\text{mK}$ plates. A schematic of the refrigerator is shown in figure 4.2.
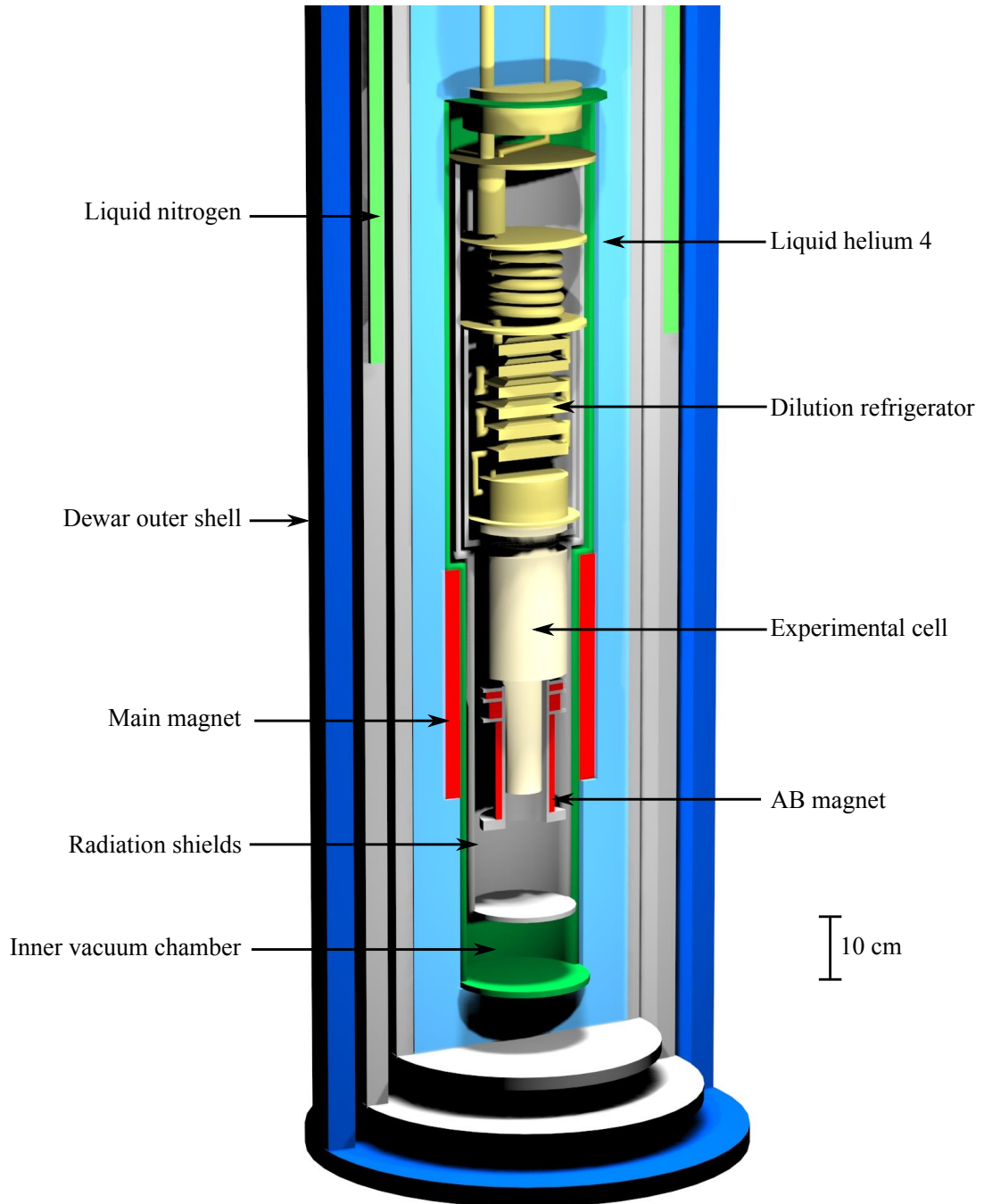
Figure 4.2: Dilution refrigerator schematic within the cryostat.

With no extra heat load, the base temperature of this particular fridge is lower than $4\,\text{mK}$. With the cell thermally connected to the mixing chamber it pre-cools the cell to approximately $5\,\text{mK}$ in preparation for nuclear adiabatic

37

demagnetisation. However, in the early stages of the experiment the fridge did not reach its base temperature. Upon removing the cell to reduce the heat load on the fridge and performing a test run we noticed that the temperature of the discrete heat exchanger stack was lower than the mixing chamber. We reasoned this was possible only if there was a short somewhere between the concentrated and dilute sides of the heat exchanger stack.

The source of the problem was found to be holes in the silver foil in three out of the four discrete heat exchangers (figure 4.3) effectively "short-circuiting" the concentrated and dilute sides of the dilution fridge. Upon rebuilding and replacing

Figure 4.3: Picture of the damaged heat exchanger. Circled is the hole in the silver foil.

all the affected heat exchangers the dilution fridge was then able to reach a base temperature of 3.5 mK within 12 hours after condensing all the mixture into the refrigerator.

Next, the experimental ^{3}He sample is further cooled by the adiabatic nuclear demagnetisation process. During this process, and measurements in the microkelvin regime, the mixing chamber of the dilution refrigerator is thermally disconnected by the aluminium superconducting heat switch from the cell and remains at its unloaded base temperature. In the following section we describe the magnets used in the experiment.

4.2 Superconducting magnets

In the experiments we used two superconducting magnets. The first one is the main magnet used in the adiabatic nuclear demagnetisation process. The maximum field it can deliver is $7.5\,\mathrm{T}$ at $90\,\mathrm{A}$. The on-axis magnetic field profile and the configuration of the bottom part of the fridge is shown in figure 4.4.
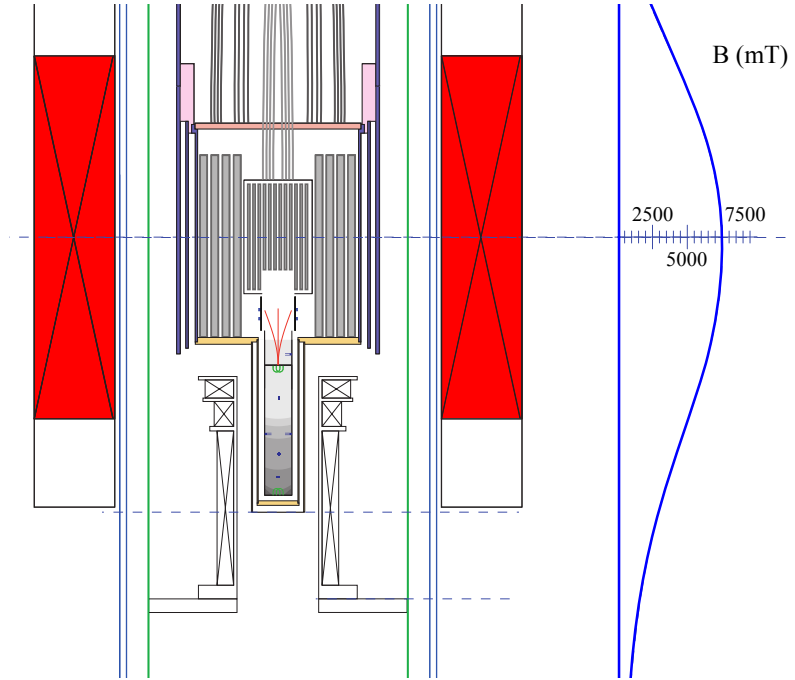
Figure 4.4: The on-axis calculated field profile of the main magnet at $90\,\mathrm{A}$ (blue lines), shown with respect to the position of the main magnet (red rectangles) and the position of the cell.

The second is the AB magnet. This magnet is attached and thermally anchored to the still radiation shield with a persistent switch at the ${}^4\mathrm{He}$ pot. The magnet completely surrounds the tail piece of the experimental cell (see figure 4.5 and 4.7). This helps to reduce the heat leaks to the experimental cell as the magnet itself acts as a radiation shield. This magnet, in conjunction with the main demagnetisation magnet, provides strong enough magnetic field to nucleate and fill half of the tail piece with ${}^3\mathrm{He}$-A. The magnet itself consists of three coils. The top two coils, labelled 2 and 3 in figure 4.5 were designed to quickly reduce the total magnetic field to zero at the copper refrigerant and in order to have accurate thermometry

39

in a low field ^{3}He-B phase at the top of the tail piece. The calculated field profiles with respect to the tail piece of the experimental cell are shown in figure 4.5. In the next section we describe the process of adiabatic nuclear demagnetisation in more detail.
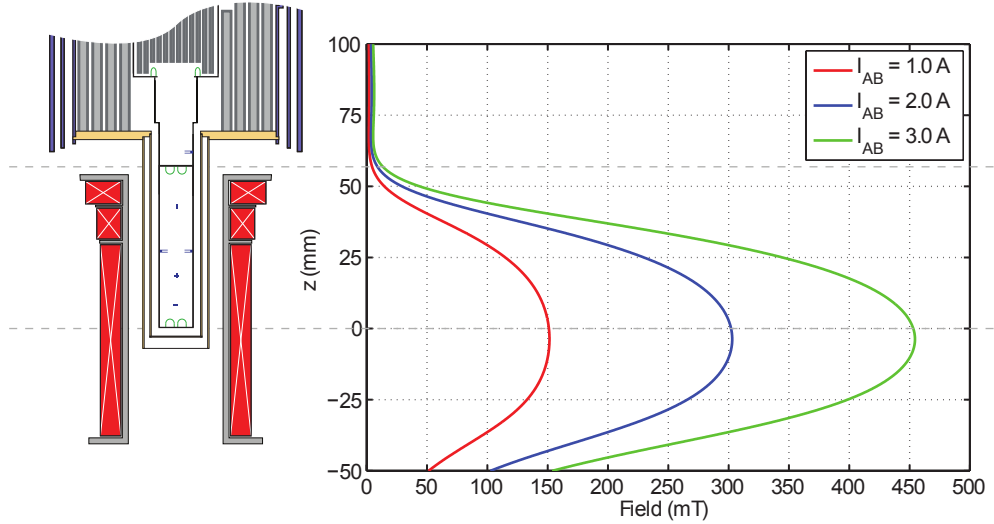
Figure 4.5: The on-axis calculated field profile of the AB magnet at various currents.

4.2.1 Adiabatic nuclear demagnetisation

Unlike the continuous cooling of a dilution refrigerator the adiabatic demagnetisation process is a one-shot process reaching sub-millikelvin temperatures.

There are three important components needed to build a demagnetisation stage: a superconducting magnet reaching large magnetic fields, a nuclear paramagnetic material to cool down and a heat switch that can adiabatically isolate the refrigerant. As previously mentioned the main magnet reaches approximately 7.5 T, the stage itself uses copper as the refrigerant and the heat switch is made out of pure aluminium. The main magnet surrounds the cell and is mounted in the helium bath on the IVC surrounding the dilution refrigerator. The copper refrigerant is thermally connected to the mixing chamber of the refrigerator via several annealed silver wires. This thermal connection is controlled by the

aluminium heat-switch with its own solenoid. By applying a magnetic field we can switch the aluminium between the normal or superconducting state which thermally connects or disconnects the experimental cell from the mixing chamber. Pure aluminium is a type I superconductor and while in the superconducting state there are virtually no free electrons left to carry heat.

A typical demagnetisation starts after at least 4 days of precool of the nuclear stage and cell by the dilution refrigerator. The typical initial temperature is $T_{in} \approx 6\,\mathrm{mK}$. The demagnetisation process itself lasts about 18 hours reducing the magnetic field to 1% of the initial field. The slow rate allows the copper to remain in thermal equilibrium with the ^{3}He sample and also reduces the risk of inducing large eddy currents [40].

In a magnetic field, the energy levels of nuclear magnetic spins are split (Zeeman splitting). The bigger the magnetic field the bigger the difference in energies between the levels. The population of these levels obeys a Boltzmann distribution on temperature. By reducing the thermal energy of this system we deplete the population of spins at higher energy levels. As mentioned above our current experimental cell uses copper as its nuclear spin is $I = 3/2$. For the entropy of this system we can write [37]

$$S_n = R \ln(2I + 1) - \frac{\lambda_n B^2}{2\mu_0 T_{in}^2}, \qquad (4.2)$$

where λ_n is the molar Curie constant. When we adiabatically isolate the system from the rest of the fridge, the entropy remains constant. Reducing the magnetic field B will then decrease the temperature of nuclear spins T_{in} by the same proportion

$$T_{fin} = T_{in} \frac{B_{fin}}{B_{in}}, \qquad (4.3)$$

where B_{in} is the initial magnetic field and B_{fin} and T_{fin} are the final magnetic field and temperature. Equation (4.3) ignores the internal magnetic field of the copper itself, $B_{int} \approx 0.36\,\mathrm{mT}$. To account for the internal field, we replace B_{fin}

and write

$$T_{fin} = T_{in} \frac{\sqrt{B_{fin}^2 + B_{int}^2}}{B_{in}}. \qquad (4.4)$$

The process of a typical demagnetisation cycle is shown on figure 4.6. This final
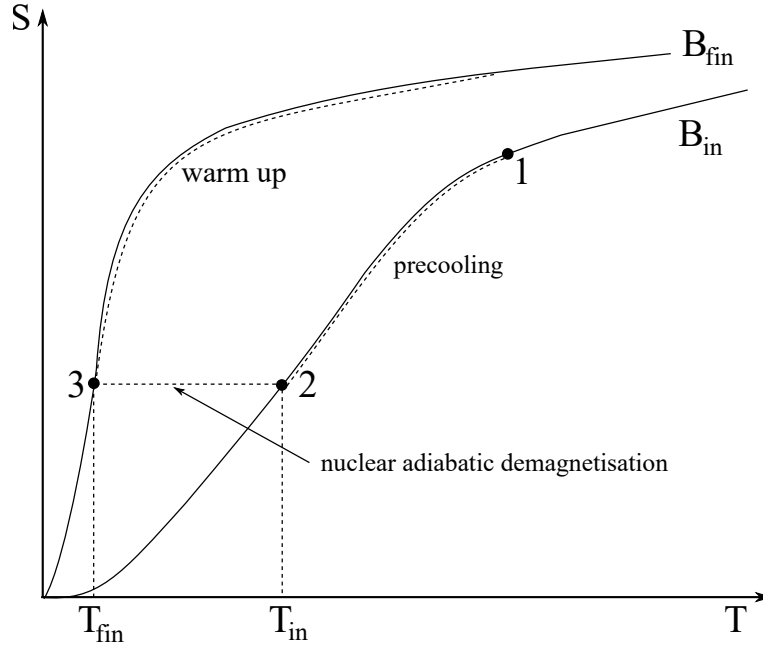
Figure 4.6: Precooling in a high magnetic field by a dilution refrigerator (1-2). Nuclear adiabatic demagnetisation of a nuclear stage (2-3).

temperature is the temperature of the nuclear spins. The nuclear spins cool the electrons. Then the electrons cool the phonons. This process is characterised by the spin-lattice relaxation time constant τ_1 which is temperature dependent and is coupled to the electron temperature using Korringa relation

$$\kappa = T_e \cdot \tau_1, \qquad (4.5)$$

where κ is the Korringa constant ($\kappa = 1.1\,\mathrm{K\,s}$ for copper) and T_e is the temperature of the electrons. The thermal equilibrium between the nuclear spins and the lattice at electron temperature T_e is achieved on a time scale of $\tau \approx 3\tau_1 = 3\kappa/T_e$. The ^{3}He sample is cooled down through thermal coupling to the copper refrigerant. This cooling is provided by phonon-phonon interactions, which is in principle very ineffective due to an acoustic mismatch, leading to a large Kapitza resistance [41].

42

In order to overcome the boundary resistance we use silver sinters to maximise the surface area in contact with ^{3}He. The silver is sintered directly on to the copper foils and plates of the nuclear stage. These silver heat exchangers offer huge heat exchange area for ^{3}He and their direct connection to the copper ensures good thermal contact between the copper refrigerant and the ^{3}He.

4.3 Experimental cell

The experimental cell is a Lancaster-type double walled nuclear demagnetisation cell. The design involves the use of two nested volumes, with the "inner cell" being the experimental volume. The "outer cell" serves as a thermal shield to the inner cell. Both of these volumes are filled with ^{3}He and both of them contain their own copper refrigerant. This allows the experimental volume to remain below $250\,\mu$K for 3 days. The cell is constructed from Araldite and Stycast 1266, rather than from metal, in order to avoid any heating from eddy currents while demagnetising. However, due to the very low thermal conductivity of plastic and the large amounts of plastic used in this cell it can take longer to cool, usually requiring at least one demagnetisation to remove the stored heat. The whole experimental cell is shown in figure 4.7.
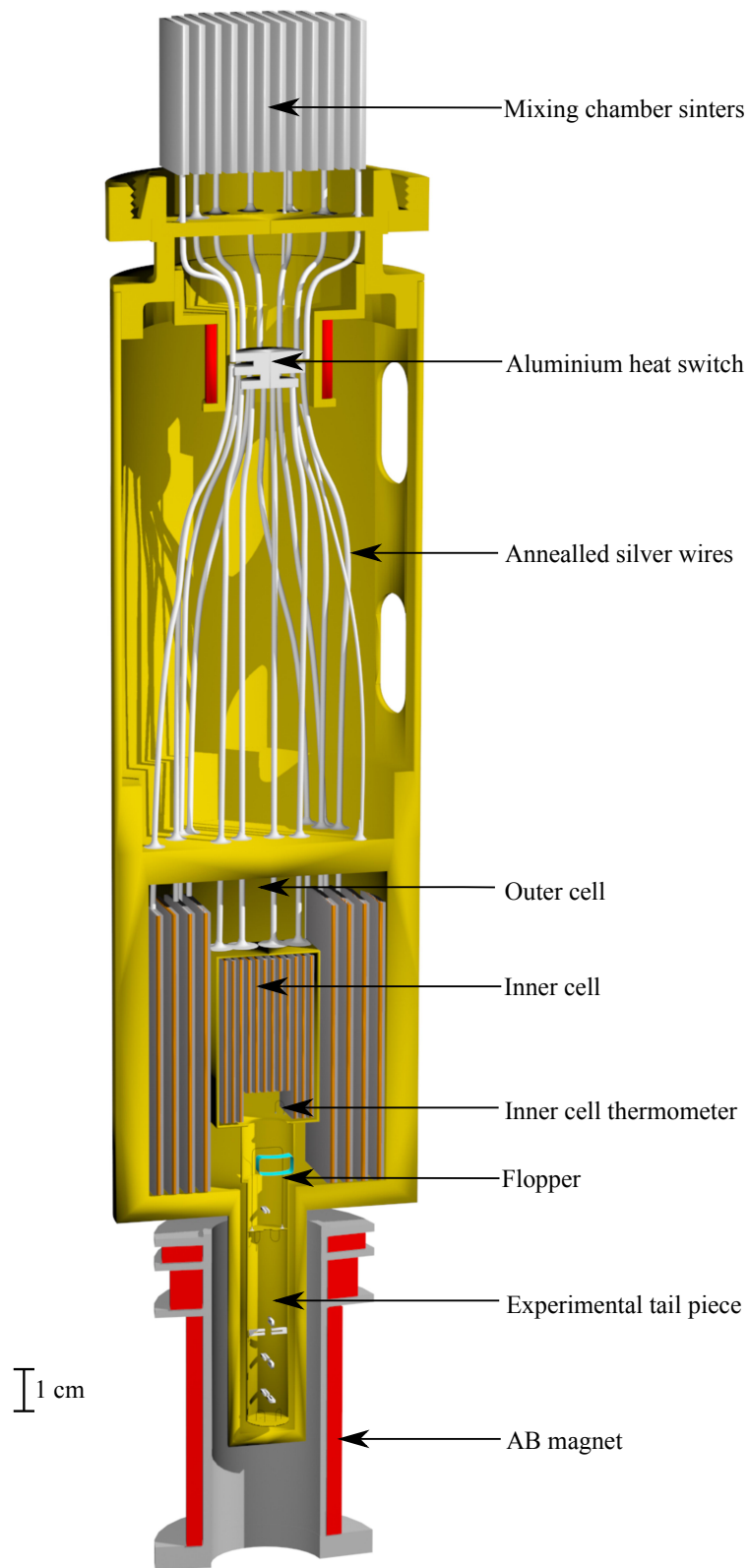
Figure 4.7: The experimental cell. Experimental devices are not to scale.

At the top is the mixing chamber silver sinter stack and the cone joint, used to connect the cell to the mixing chamber. Under the sinter stack is the heat switch

with its own solenoid thermally connecting or isolating the experimental cell.

The inner cell experimental volume consists of two parts: the upper cell and the experimental tail piece. The upper cell, shown in figure 4.8, contains the flopper, two quartz tuning forks and several vibrating wires, such as a $125\,\mu$m diameter tantalum thermometer wire used to monitor the precooling and demagnetisation processes, a $13.5\,\mu$m diameter heater wire and a $4.5\,\mu$m diameter thermometer wire. The properties, construction and use of these measurement tools will be discussed in the next section.
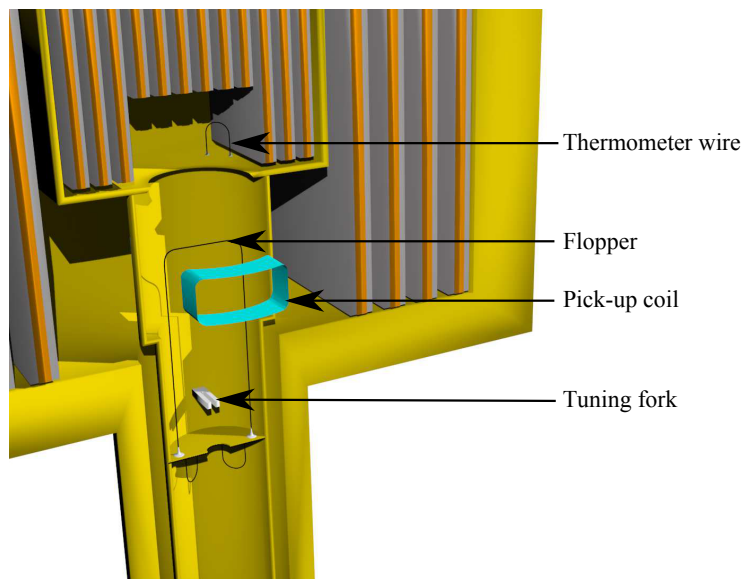
Figure 4.8: Close up of the top part of the experimental cell with the flopper. The heater wire and the tantalum thermometer wire occupy the same space as the $4.5\,\mu$m thermometer wire. Experimental devices are not to scale.

The tail piece is separated from the upper cell by the base-plate of the flopper. Along with the flopper another $13.5\,\mu$m heater wire and a $4.5\,\mu$m thermometer wire are mounted below this plate. The base plate features a $1.4\,$mm diameter hole that connects the tail piece to the upper cell. The tail piece is very weakly thermally connected to the inner cell. Thus, it could be used as a ^{3}He black body radiator (BBR) [42, 43]. A BBR is a technique used to directly measure the dissipated power. However, this technique was not used in experiments described in this thesis.

The tail piece, shown in figure 4.9, was designed to probe the AB interface of ^{3}He at ultra-low temperatures. The whole tail piece fits inside the AB magnet shown in figure 4.7. The probes are quartz tuning forks mounted on the walls. These forks are positioned in one of two different orientations so that their prongs oscillate horizontally or vertically. The bottom part of the tail piece includes the last set of a $13.5\,\mu$m heater wire and a $4.5\,\mu$m thermometer wire.
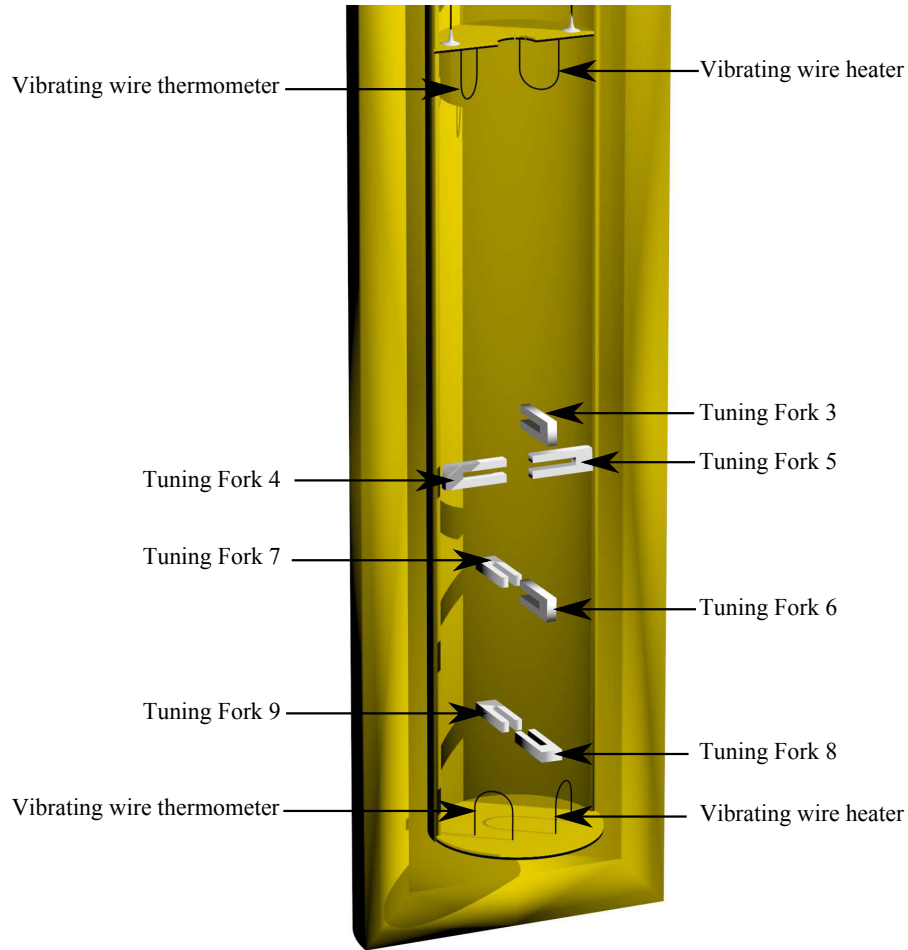
Figure 4.9: Close up of the experimental tail piece with the array of tuning forks.

In the next section I will briefly describe relevant the theory of vibrating objects in ^{3}He, followed by our construction methods for the various devices.

4.4 Vibrating objects

Vibrating object such as vibrating wires, grids, quartz tuning forks and whiskers have been used in low temperature physics for a long time [3, 44, 45, 46]. In the experiments described in this work we made extensive use of vibrating wires, tuning forks and the flopper for thermometry and for direct measurements of the damping force.

These objects have shown themselves to be extremely useful for probing quantum fluids at low temperatures. They introduce small amounts of heat into the system and the damping experienced by these objects comes almost entirely from their interactions with the fluid.

We can describe the dynamics of such objects in terms of simple harmonic oscillators (if we assume that the vibrations are small and weakly damped). The equation of motion for the driven harmonic oscillator is

$$m^* \frac{d^2 x}{dt^2} + \Gamma \frac{dx}{dt} + kx = F(t), \qquad (4.6)$$

where m^* is the effective mass of the vibrating object, Γ is a parameter characterising the damping, k is the spring constant and $F(t)$ is the driving force. The effective mass of the object (be it a fork or a wire) is the sum of its mass in vacuum, the mass of fluid viscously coupled to its surface and a contribution owing to the fluid backflow. Solving equation (4.6) for the velocity $\dot{x}$

$$\dot{x} = \frac{dx}{dt} = v_0 e^{i\omega t}, \qquad (4.7)$$

we get the velocity amplitude (assuming that the driving force is periodic)

$$v_0 = \frac{F_0 i\omega}{k - \omega^2 m^* + i\omega \Gamma}, \qquad (4.8)$$

a complex Lorentzian function which can be split into real and imaginary parts

$$Re\{v_0\} = \frac{F_0 m^* \omega^2 \Gamma}{\omega^2 \Gamma^2 + (k - \omega^2 m^*)^2}, \tag{4.9}$$

and

$$Im\{v_0\} = \frac{F_0 \omega(k - \omega^2 m^*)}{\omega^2 \Gamma^2 + (k - \omega^2 m^*)^2}, \tag{4.10}$$

These equations describe the dependence of absorption and dispersion on excitation frequency and are shown in figure 4.10. From equation (4.9) it is clear that
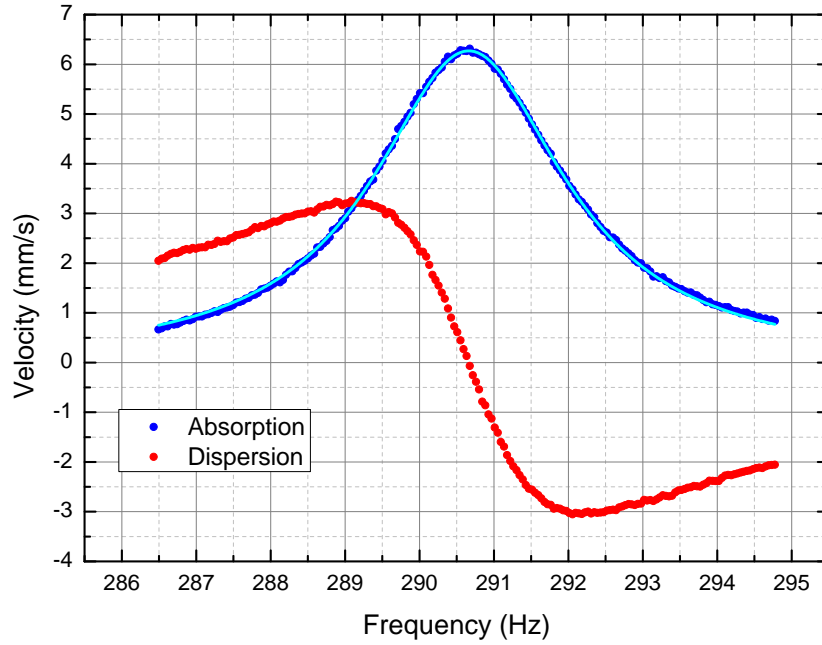
Figure 4.10: Absorption and dispersion components as measured by lock-in amplifier for a typical vibrating wire. The bright blue line is the Lorentzian fit.

at frequency

$$\omega = \sqrt{\frac{k}{m^*}}, \tag{4.11}$$

the $Re\{v_0\}$ reaches its maximum of

$$Re\{v_0\} = \frac{F_0}{\Gamma}, \tag{4.12}$$

48

The quadrature has two local extrema when $k - \omega^2 m^* = \pm\omega\Gamma$ (equation (4.10)). The difference between the values of ω that satisfy this condition gives the full width at half maximum of the resonance, also known as the width. The width is inversely proportional to the effective mass m^* of the wire.

$$\Delta\omega = \frac{\Gamma}{m^*}. \tag{4.13}$$

From equation (4.12) we can write

$$\Gamma = \frac{F_0}{Re\{v_0\}} = \frac{F_0}{v_0}, \tag{4.14}$$

where v_0 is the velocity amplitude of the oscillator at resonance. Inserting equation (4.14) into equation (4.13) we get the width as a function of force, velocity and effective mass of the oscillator

$$\Delta f = \frac{F_0}{2\pi v_0 m^*}. \tag{4.15}$$

this allows us to characterise the "strength" of the resonance with the "height times width over drive" (HWD) parameter.

$$(HWD) = \frac{v_0 \Delta f}{F_0} = \frac{1}{2\pi m^*}. \tag{4.16}$$

This model considers only a simple model of motion of the resonator.

4.4.1 Forces acting on moving objects in ^{3}He

In this subsection we will look into all the forces acting on a vibrating object moving through ^{3}He. In our experiments all of the oscillators are driven by waveform generators supplying periodic voltages or currents. As mentioned in the previous section the driving force acting on an oscillator in steady state is balanced by three forces: inertial, damping and the restoring force.

$$F = F_i + F_D + F_R = m^*\ddot{x} + \Gamma\dot{x} + m^*\omega^2 x. \tag{4.17}$$

On resonance the inertial and restoring forces cancel out giving

$$F = F_D = \Gamma\dot{x}_0. \tag{4.18}$$

The total damping force is a sum of three forces: intrinsic, thermal and pair breaking

$$F_D = F_{IN} + F_{TH} + F_{PB}. \tag{4.19}$$

The intrinsic damping is related to the oscillator itself and its mechanical properties. The thermal damping force is described in section 3.4 and we know it is a contribution to damping by thermal excitations (equation (3.42)). The pair breaking damping, as the name suggests, comes into play only when velocities of the oscillations are high. At high enough velocities the dispersion curves get tilted in such a way that the energy cost to break a Cooper pair and promote quasiparticles form the condensate to become excitations is zero. This process is referred to as pair breaking process.

4.4.2 Oscillator thermometry

One of the primary usages of vibrating objects in our experiments is to accurately measure the temperature of superfluid ^{3}He-B. We do this by inferring the density of thermally-excited quasiparticles. For oscillators like the vibrating wire or tuning fork, equation (3.42) describes the thermal excitation damping force. When the oscillator is moving at such low velocities that $\lambda p_F v \ll k_B T$, the exponential dependence on v in equation (3.42) can be expanded to first order, giving

$$F_{TH} = \gamma \lambda A 2 p_F^2 g(E_F) v_F e^{-\frac{\Delta}{k_B T}}. \tag{4.20}$$

Recalling equation (4.15) the dependence of width on F_0, v_0 and m^*. Identifying F_0 with F_{TH} and substituting equation (4.20) into (4.15) we get

$$\Delta f = \frac{\gamma \lambda A p_F^2 g(E_F) v_F}{\pi m^*} e^{-\frac{\Delta}{k_B T}}. \tag{4.21}$$

This gives us the width as a function of energy gap Δ and temperature T. Experimentally the measured width contains also the intrinsic damping component. In order to correctly calculate the temperature it is necessary to subtract this component Δf^i from the measured resonant width. Further rearranging of equation (4.21) yields temperature as a function of width

$$T = \frac{\Delta}{k_B \ln \left(\dfrac{a}{\Delta f - \Delta f^i} \right)}, \tag{4.22}$$

where a is

$$a = \frac{\gamma \lambda A p_F^2 g(E_F) v_F}{\pi m^*}. \tag{4.23}$$

The value of $\gamma = 0.28$ was calculated for a $4.5\,\mu$m wire [43]. Then the calibration factor $a = 1.691 \times 10^5\,Hz$ is used for a $4.5\,\mu$m thermometer wire.

In the next few subsections we will take a more detailed look at each vibrating object in use in our experiment.

4.4.3 Vibrating wires

Construction

The construction of a vibrating wire is described in detail in [3, 47] so here I will briefly summarise. For low temperature experiments we use a multi-filament NbTi wire. To prepare the wire it is necessary to first remove the enamel coating of the wire by submerging it in a wire stripper. Any remaining coating is then removed by a Scotch-Brite abrasive cloth. The base of a vibrating wire is made from a Stycast 1266 impregnated paper. Using a pin, two small holes are made in the paper. The wire is then threaded through the two holes to create a small loop.

Usually the wire is pulled onto a former to form its semicircular shape. Two drops of stycast are then used to glue the wire's legs to the paper.
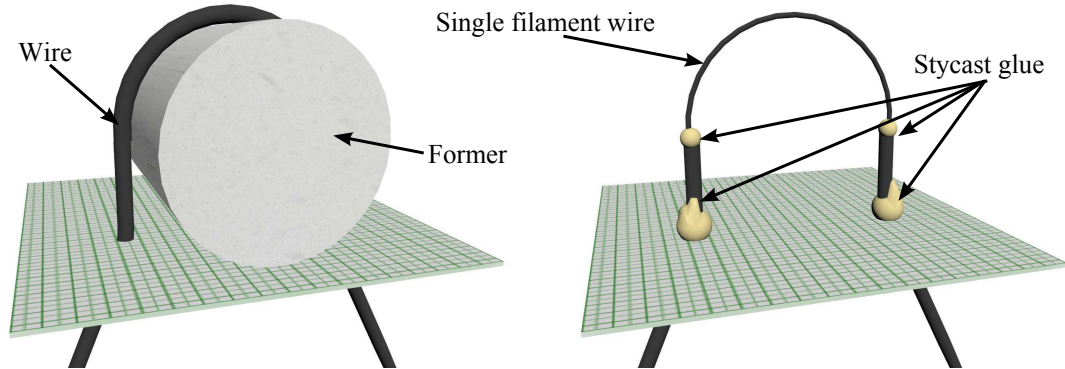
Figure 4.11: Constrution of a vibrating wire. A typical leg spacing of a vibrating wire is on the order of $2\,\text{mm}$.

The semicircular part of the wire is then dipped into concentrated nitric acid to dissolve all the copper cladding of the wire filaments. The filaments are then plucked away using tweezers, microscope and patience until only one filament remains. Stycast epoxy is used again to glue all the broken ends of the filaments to the wire's legs.

Operation

If there is an AC current $(\text{I}=I_0\sin(\omega t))$ passing through such a wire in a magnetic field, there will be a force acting on the wire that will cause it to oscillate. This force is the Lorentz force

$$\mathbf{F} = e(\mathbf{v} \times \mathbf{B}), \tag{4.24}$$

where $\mathbf{v}$ is the velocity of charge and $\mathbf{B}$ is the magnetic field. We can further simplify the situation by assuming the wire is goalpost-shaped and neglect the contribution of the wire legs. This scenario is illustrated in figure 4.12 where only the cross bar moves through the magnetic field. This simplifies equation (4.24) to

$$F = BID, \tag{4.25}$$

where I is the current and D is the leg spacing of the wire (length of the cross

bar). The motion of such a wire through a stationary magnetic field induces a
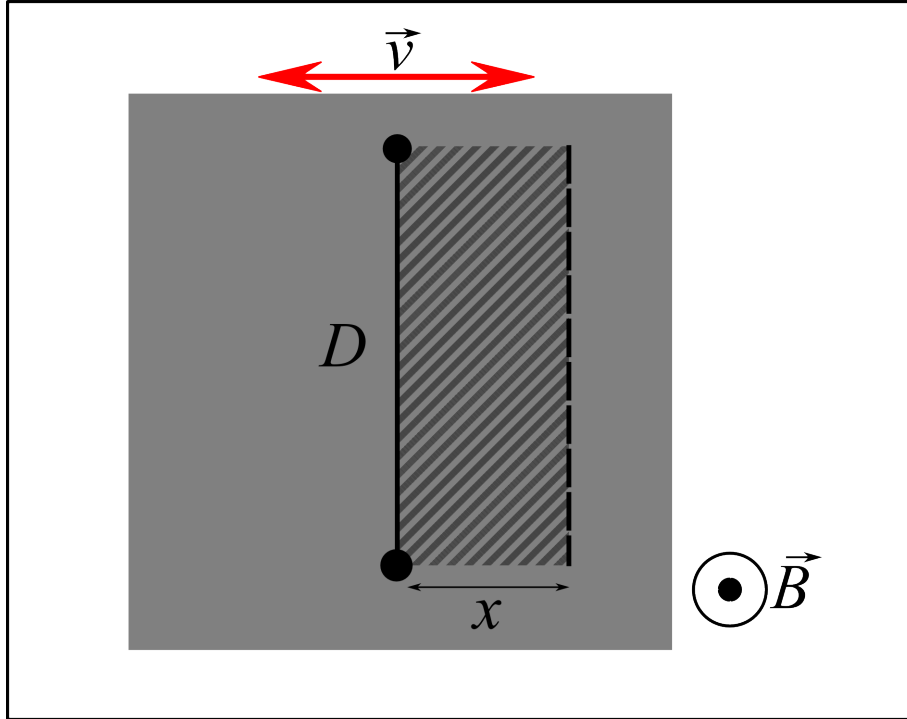
Figure 4.12: Vibrating wire model.

Faraday voltage in the wire

$$V = \frac{d\Phi}{dt},$$

(4.26)

where Φ is the magnetic flux. Thus

$$V = \frac{d(\mathbf{B}.\mathbf{A})}{dt} = \frac{\mathbf{B}d\mathbf{A}}{dt},$$

(4.27)

where $\mathbf{A}$ is the hatched area shown in figure 4.12. In simple terms this area is equal to the leg spacing of the wire multiplied by the displacement of the crossbar. Considering our scenario (figure 4.12) the angle between the vector of the magnetic field $\mathbf{B}$ and area $\mathbf{A}$ is 0 degrees simplifying the dot product. Since the leg spacing is constant and does not depend on time, equation (4.27) becomes

$$V = \frac{BDdx}{dt} = BD\dot{x},$$

(4.28)

where $\dot{x}$ is the velocity of the wire.

This describes the goalpost-shaped flopper well, but all the other vibrating wires are semicircular in shape. The rate of change of the angle between vectors **B** and **A** can be expressed as $\frac{2\dot{x}}{D}$ while the area is $A = \frac{\pi D^2}{8}$, so equation (4.28) becomes,

$$V = \frac{\pi}{4} B D \dot{x}, \tag{4.29}$$

The response voltage is measured by a lock-in amplifier synchronised with the waveform generator.

4.4.4 Flopper

The flopper is a key new device for studying the superfluid phases of ^{3}He-B. The idea behind its construction was to build a vibrating wire with low quality factor and low resonant frequency. While the usual shape of the vibrating wires used in Lancaster is a semicircle, the flopper is a goalpost-shaped vibrating wire. Also, the flopper is a very "large" vibrating wire when compared with the rest of the vibrating wires used by the Lancaster group both in terms of wire diameter and loop size. While the usual vibrating wires have leg-spacing on the order of 2 mm and a height of approximately 2 mm, the floppers leg-spacing is 9 mm and the legs are 25 mm long. The flopper is made out of a single-core NbTi wire with an outer diameter of 100 μm [48]. The NbTi wire is copper clad with an insulating enamel coating. In the process of construction the insulation and the copper cladding were not removed. This was done in order to add support to the wire, spoil the Q-factor and reduce the resonant frequency by having a large mass. The resonant frequency of the flopper is 66.19 Hz and its Q-factor is approximately 1320 in superfluid ^{3}He-B at approximately 150 μK.

Construction of this wire is very similar to the construction of its smaller counter-parts with only one major difference: due to the sheer size of the wire the corners had to be formed using tweezers before using the former. This was done in order to avoid deformation of the wire. Our previous attempts in building the flopper by directly using the former led to the wire being deformed in its
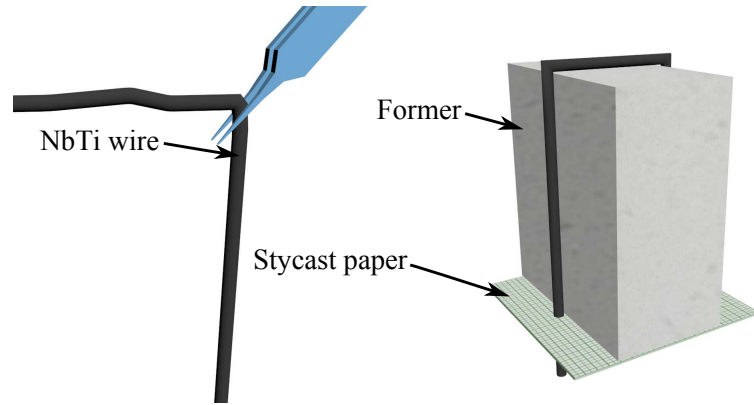
Figure 4.13: Schematic of flopper construction.

shape. After bending, the legs of the goalpost were threaded through a Stycast-impregnated paper and glued in place using two drops of Stycast 1266. The schematic of the construction process is shown in figure 4.13. The twisted pairs of voltage and current leads were soldered to the legs of the goalpost under the Stycast-impregnated paper. What distinct this wire from any other oscillator currently in use is its sheer size and the use of different circuitry. This circuitry gives us the capability to switch between AC and DC drive of the flopper, thus changing its motion from oscillatory to for example controlled linear movement at a constant velocity. The circuitry is explained in more detail in section 4.5.1.

As mentioned in section 4.4.3, it is easy to determine the velocity of the wire while in oscillatory motion due to Faraday voltage induced by its motion through a magnetic field using a lock-in amplifier. Problems with determining the velocity arise when the flopper is moving in the linear regime. In this regime we utilise a different method of measurement and instead of velocity, we directly measure the position of the wire via two detection (or pick-up) coils placed at the side of the flopper (see figure 4.14).

The pick-up coils used in the experiment are 10 mm in diameter with 100 turns each using a 0.1 mm multi-filament NbTi wire. The coils are in the outer cell mounted on the outside of the inner cell wall. This puts the flopper in the middle of the two coils (approximately 7.5 mm between the flopper and each detection
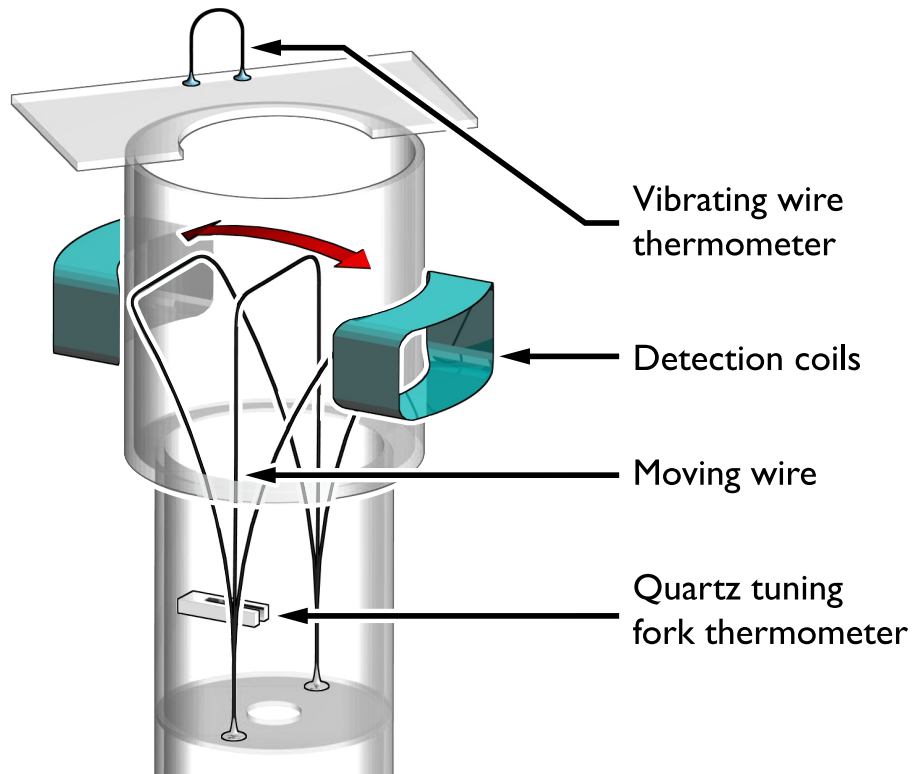
Figure 4.14: Experimental arrangement of the flopper and its pick-up coils. The flopper is mounted in the inner cell with a tuning fork and a $4.5\,\mu\text{m}$ wire acting as thermometers.

coil).

A high frequency probe current $(96.4\,\text{kHz})$, that does not interfere with the motion of the flopper, induces voltage in the two coils. This induced voltage is then measured by a lock-in amplifier (referenced to the high frequency probe current), and by knowing the geometry of the system we are able to derive the exact position of flopper. The position calibration process is addressed in more detail in section 6.2.1.

4.4.5   Quartz tuning forks

Construction

Quartz tuning forks are piezo-electric devices commonly found in many electronic appliances such as wristwatch, atomic force microscopes, etc. Here, I will briefly address the tuning fork construction and its experimental preparation. All tuning forks provided by manufacturers come encased in a metal box or cylindrical can [49]. The container, be it a box or a can, contains magnetic materials and must be removed. The bare tuning fork is then remeasured to ensure that its Q-factor stayed constant and that the fork was undamaged in the unpacking process. The next stage in the construction process is to solder two $150\,\mu$m thick copper wires onto pre-tinned contact pads of the fork as shown in figure 4.15.
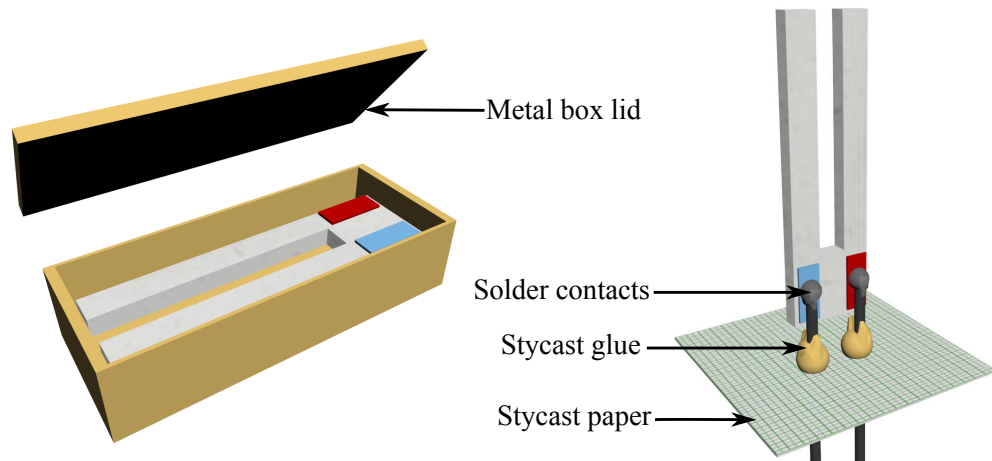
Figure 4.15: Schematic of tuning fork construction.

The wires are then threaded through Stycast-impregnated paper. The base of the tuning fork and the leads are then glued onto the paper by another drop of Stycast.

For our experiments we used nine $32\,$kHz tuning forks with high Q-factors ($Q \approx 5000$). Due to the high Q-factors, the detected signals of tuning forks with similar resonant frequencies are highly susceptible to cross-talk. A method was developed (described better in [50]) to "re-tune" the tuning forks while maintaining their high Q-factors. By adding a small drop of Stycast on the tip of the prongs of

the tuning fork we changed the mass of the prongs. This change in mass shifted the resonant frequency of the tuning fork. By applying different amounts of Stycast to each tuning fork we successfully separated the resonant frequencies of the tuning forks by $\approx 100\,\mathrm{Hz}$.

Operation

In the case of the tuning fork, we drive with an applied voltage and detect the current. As for the wires the tuning fork is very well described by the equation of damped simple harmonic motion (4.6). Due to the piezo-electric effect an applied electric field on the electrodes of the fork polarizes atoms within the fork which results in lattice deformations, resulting in prong displacement. If the applied electric field is periodic, the polarization of the fork will change in time. This results in a displacement current I(t) which depends on the amplitude of the electric field and on the rate of displacement, i.e., the velocity of the prongs [46, 51]

$$I(t) = \alpha \frac{dx(t)}{dt} = \alpha v, \tag{4.30}$$

where α is a constant linking the mechanical and electrical properties of each individual fork.

For the amplitude of the periodic force acting on the prongs of the tuning fork we can write

$$F_0 = \alpha \frac{V_0}{2}, \tag{4.31}$$

where V_0 is the amplitude of the drive voltage and the factor of two comes from the fact that the tuning fork has two prongs and is a convention.

The maximum prong velocity amplitude occurs on resonance. Then from equation (4.6) we can write for the drive force of amplitude F_0

$$F_0 = v_0 \Gamma 2, \tag{4.32}$$

Combining equations (4.31),(4.30),(4.15) with equation (4.32) we can determine

the α calibration constant as

$$\alpha = \sqrt{\frac{\Delta f I_0 2 m^*}{V_0}}, \tag{4.33}$$

where Δf is the width of the tuning fork resonance and I_0 is the amplitude of the displacement current at resonance. It is possible to determine α experimentally. The value of I_0/V_0 can be measured as the slope of the displacement current against the drive voltage. The effective mass of the bare tuning fork is calculated theoretically by treating the prongs of the tuning fork as cantilever beams fixed at one end. Then for the effective mass we can write [52]

$$m^* = 0.25 \rho L W T, \tag{4.34}$$

where ρ is the density of quartz and LWT are the length, width and thickness of the prong. The measured α constants for the tuning forks used in the experiment are $\alpha = 2.07 \times 10^{-6}\,\mathrm{C\,m^{-1}}$ for tuning fork 6 and $\alpha = 1.84 \times 10^{-6}\,\mathrm{C\,m^{-1}}$ for tuning fork 7 [53].

4.4.6 Potential flow

As was mentioned above, the motion of any massive object in a fluid creates backflow, and the velocity profile of this backflow depends on the shape and geometry of the object. In this subsection we will describe the velocity enhancement of pure potential backflow [3, 54, 55] around the experimental tools, such as a vibrating wire and the flopper. We define β as the velocity enhancement factor.

In simple terms we can approximate a vibrating wire as an infinitely long cylinder of radius R (along the z axis) moving through the superfluid at constant velocity v_{vw} along the x axis. In the frame of reference of the wire, the superfluid

is moving towards the wire at velocity

$$\boldsymbol{v} = v_{vw}\hat{i} + 0\hat{j}, \tag{4.35}$$

at the boundary with the cylinder

$$\boldsymbol{v}.\hat{n} = 0, \tag{4.36}$$

where $\hat{n}$ is the normal to the cylinder surface. Lets consider now that the liquid is inviscid, incompressible, without vorticity and with constant density. Then the velocity vector is irrotational.

$$\nabla \times \boldsymbol{v} = 0. \tag{4.37}$$

Being irrotational there must exist a velocity potential Φ for which we can write

$$\boldsymbol{v} = \nabla\Phi, \tag{4.38}$$

and furthermore since the fluid is incompressible the velocity potential must satisfy Laplace's equation. For convenience we work in the 2D polar coordinate system with the centre of the wire cross section at the origin. The solution to Laplace's equation that satisfies the boundary condition is [55]

$$\Phi = v_{vw}\left(r - \frac{R^2}{r}\right)\cos\theta, \tag{4.39}$$

The radial and tangential velocity components are then obtained from $\nabla\Phi$

$$v_R = \frac{\partial\Phi}{\partial r} = v_{vw}\left(1 - \frac{R^2}{r^2}\right)\cos\theta, \tag{4.40}$$

$$v_\theta = \frac{1}{r}\frac{\partial\Phi}{\partial\theta} = v_{vw}\left(1 + \frac{R^2}{r^2}\right)\sin\theta, \tag{4.41}$$

where r and θ are coordinates of a point in space with $r \geq R$. The speed of the

superfluid is then calculated as

$$v_s = \sqrt{v_R^2 + v_\theta^2}.$$
(4.42)

The calculated speed profile of the superfluid is shown in figure 4.16. Note that
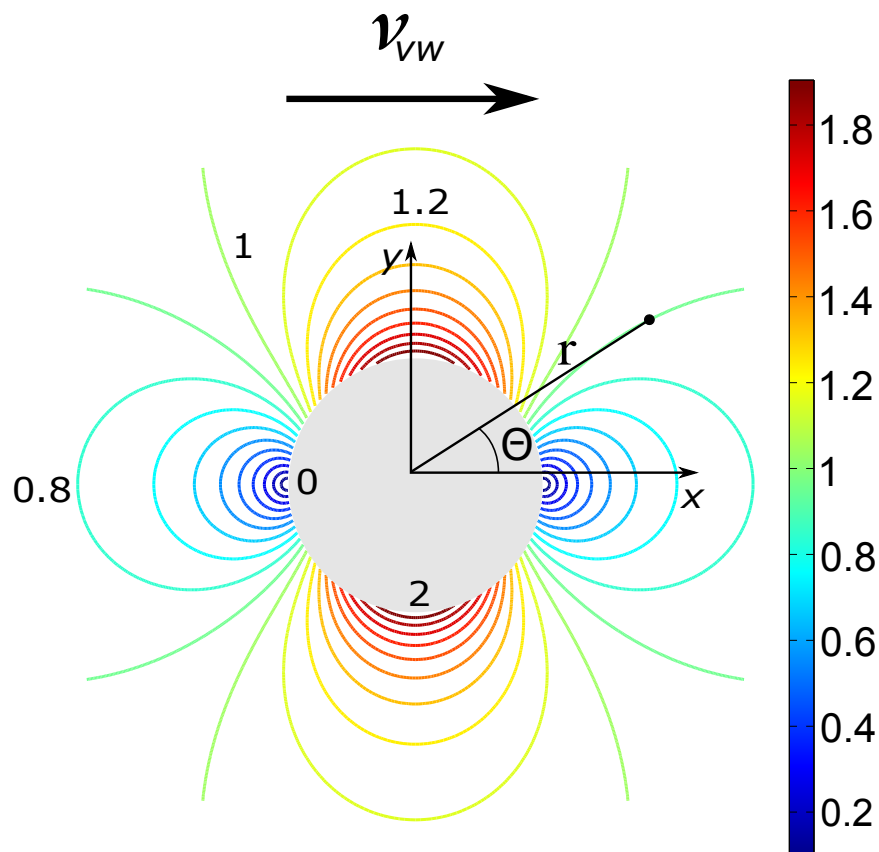
Figure 4.16: The velocity enhancement around a vibrating wire, where $\boldsymbol{v}$ is the velocity of the wire.

the maximum speed is at the poles of the wire where $\theta = \pi/2$ and the speed of the superfluid is $v_s = \beta v_{vw} = 2v_{vw}$. For a vibrating wire the velocity enhancement factor $\beta = 2$.

4.5 Measurement techniques

4.5.1 Measurement circuits

The measurement circuits of vibrating wires and tuning forks are shown in figure 4.17. Both of these circuits use Agilent 33220 function generators to supply the voltage. The device response signal is measured by a Stanford SRS830 lock-in amplifier referenced with the generator.

For vibrating wires the drive voltage supplied by the generator is converted to the drive current in a home made device called the "drive box". The drive box contains a 6:1 step down transformer and multiple different resistors. All the twisted pairs of drive and detection leads are heat sunk to various stages of the dilution refrigerator. This is done to prevent any unwanted heating coming down the wires into the experiment. The transformer on the detection side of the vibrating wire circuit shown in figure 4.17 is unique for $4.5\,\mu$m wire circuits and is used to amplify the detection signal. It has a step up ratio of 1:30. The detection leads go straight into the lock-in amplifier.

The drive voltage of the tuning forks is controlled by using attenuators. The attenuators reduce the voltage by a factor of approximately 10. Each of the attenuators in use has a slightly different attenuation and so each was separately measured in order to obtain the precise value. Similar to the vibrating wire, the twisted pairs of the tuning fork drive circuit are thermally anchored at various stages of the refrigerator. The shielded superconducting co-axial leads are used for the detection side. These leads enter a current to voltage (I-V) converter through a buffer unit. The buffer unit is a device that simply acts as a common ground for up to five tuning forks. The I-V converter converts the response current into voltage measured by the lock-in amplifier. The I-V converter in use is a Stanford research systems model SR570. Experience has shown that it is necessary that the I-V converter and the signal generator share the same ground. This was done on the top of the cryostat where the drive and detection leads enter the cryostat.
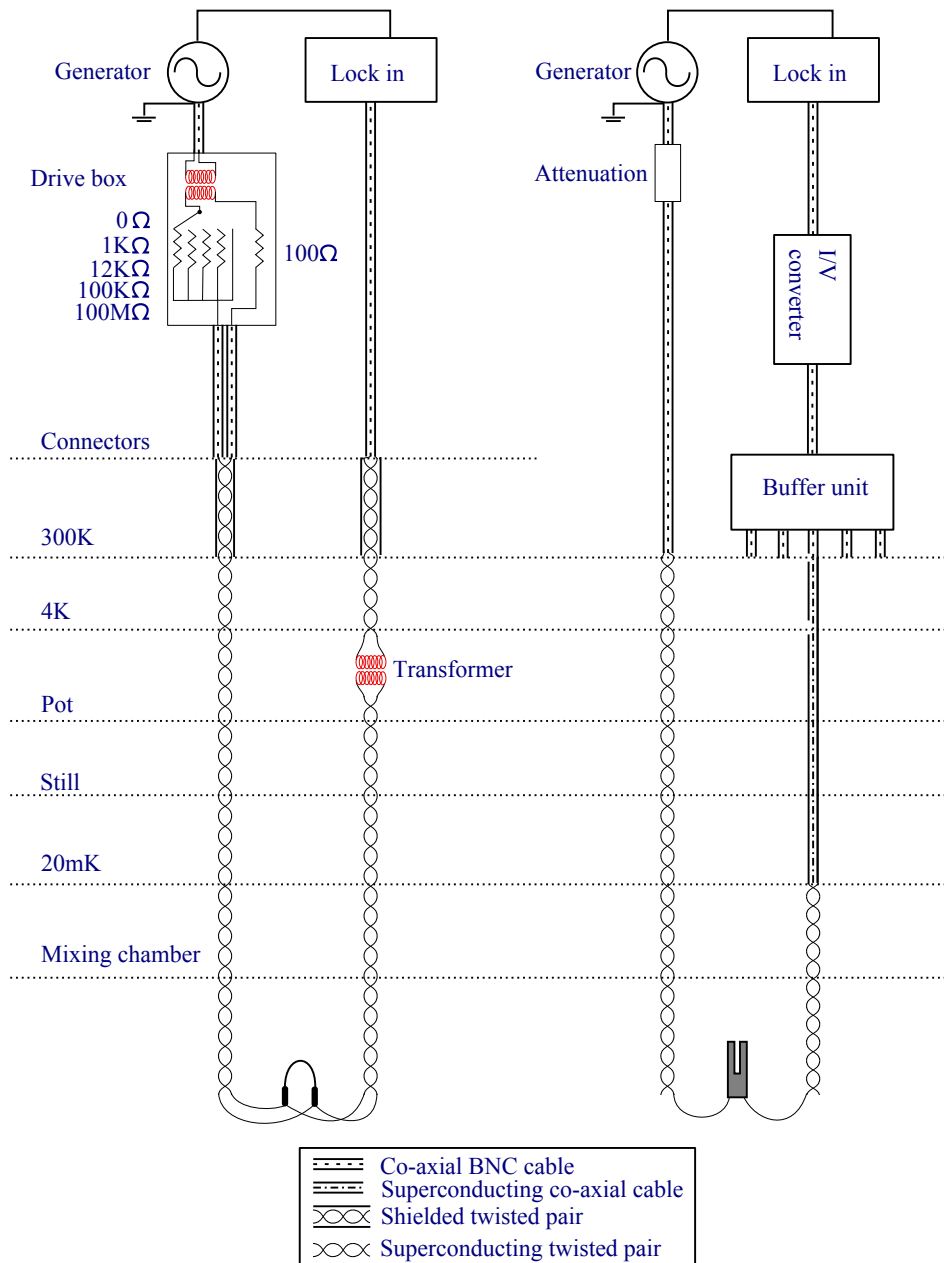
Figure 4.17: Left: the measurement circuit of vibrating wire. Right: the measurement circuit of a tuning fork.

For AC measurements the flopper measurement circuit is very similar to that of the previously described vibrating wires. The only difference is that the circuit does not contain any step-down transformers. Due to the low frequency range of the flopper the transformer would not have worked properly. The flopper measurement circuit is shown in figure 4.18.

For DC motion the custom-made current source of the flopper has two inputs. One is the DC offset that can be produced by a generator or by a DAQ card controlled by the measurement computer. The other is the high frequency (96.4 kHz) probe current used to detect the position of the flopper. The detection lock-ins in use are referenced to the high frequency probe current generator. The current source combines the two drive signals and the resulting drive current then passes through a $1\,\Omega$ resistor. The voltage across this resistor is measured by a lock-in amplifier for the AC part of the signal and the DC part is measured by a volt meter. This way we measure exactly the drive current passing through the flopper. The drive current is passed to the top of the cryostat by a twisted pair of low resistance wires. From the top of the cryostat down to the legs of the flopper we use superconductors.

As mentioned earlier the high frequency probe current is detected by the pick-up coils. Both of the coils are connected to lock-ins via superconducting coaxial cables.

In the experiment the lock-in outputs were measured by a DAQ card, which controlled the DC input of the drive.
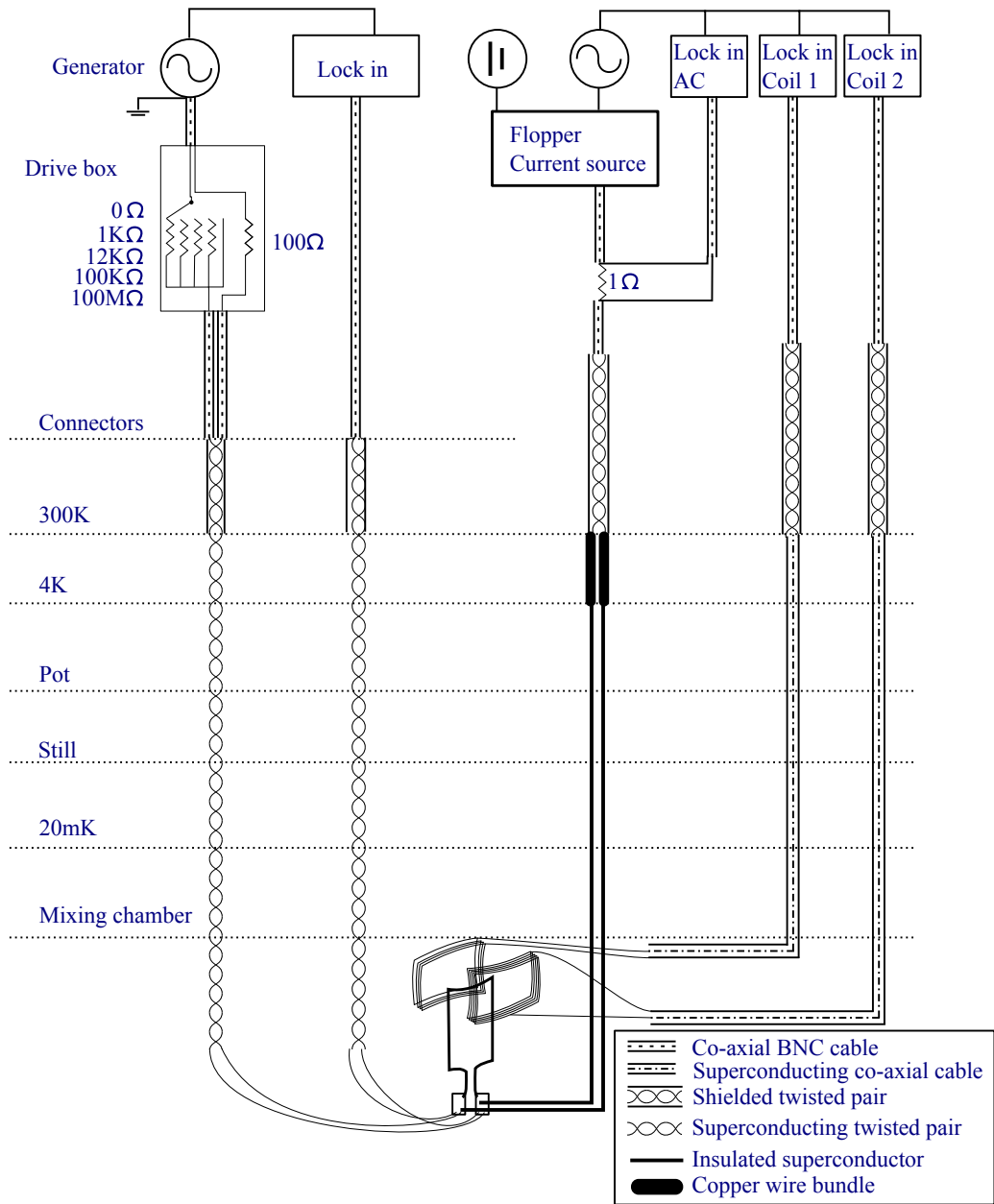
Figure 4.18: Flopper measurement circuit.

4.5.2 Lock-in amplifier

Lock-in amplifiers form the backbone of our measurements. Therefore, it is important to at least briefly describe their operation. In simple terms a lock-in amplifier consists of signal multipliers and low-pass filters. Apart from the measurement signal, the lock-in amplifier also requires a reference signal. Typically the reference signal is external, provided by the generator used to drive the measured device, but it also can be internal, i.e., supplied by the lock-in amplifier itself. The lock-in amplifier multiplies the measured signal with the reference signal. Lets assume that the measurement signal has a form:

$$\mathbf{V}_M = V_{M0}\cos(\omega_M t + \phi), \tag{4.43}$$

where ϕ is the phase, and the reference signal is expressed as

$$\mathbf{V}_R = V_{R0}e^{i\omega_R t}. \tag{4.44}$$

The output of the analogue multipliers is split into two channels (absorption and dispersion) each having two a component signal:

$$Re\left\{\mathbf{V}_A\right\} = 1/2\left[V_{M0}V_{R0}\cos((\omega_M + \omega_R)t + \phi) + V_{M0}V_{R0}\cos((\omega_M - \omega_R)t + \phi)\right] \tag{4.45}$$

and

$$Im\left\{\mathbf{V}_A\right\} = 1/2\left[V_{M0}V_{R0}\sin((\omega_M + \omega_R)t + \phi) + V_{M0}V_{R0}\sin((\omega_M - \omega_R)t + \phi)\right]. \tag{4.46}$$

The active low-pass filters, for which the frequency cut-off can be adjusted, suppress the high frequency components $(\omega_M + \omega_R)$ and amplify the low frequency components $(\omega_M - \omega_R)$. Usually, the frequency of the reference signal is identical (or very similar) to the frequency of the measured signal $\omega_M = \omega_R = \omega$. Thus,

equations (4.45) and (4.46) can be rewritten as:

$$Re\left\{\mathbf{V}_A\right\} = K(\omega)V_{M0}V_{R0}\cos(\phi), \qquad (4.47)$$

and

$$Im\left\{\mathbf{V}_A\right\} = K(\omega)V_{M0}V_{R0}\sin(\phi), \qquad (4.48)$$

where $K(\omega)$ is the transmission characteristic of the low pass filters. We identify expression (4.47) with (4.9) and (4.48) with (4.10). The lock-in technique selects and amplifies phase-correlated signals, while suppressing all others. It even has the capability to measure the signal at levels comparable with noise because noise signals are usually uncorrelated in phase. The bandwidth of the low-pass filters determines the level of noise and the time constant of the lock-in amplifier response. Typically $\omega_M - \omega_R < 1/\tau$, where τ is the time constant of the low-pass filters. A bigger time constant τ reduces noise but increases the time response of the lock in amplifier.

4.5.3 Frequency sweeping techniques

The frequency sweep is a basic method of measuring any oscillator. The oscillator is excited by an AC current supplied by a waveform generator. The frequency of the current is slowly changed while the drive amplitude remains constant. The slow speed of change in the frequency is to avoid unwanted ringing of the oscillator. In the experiments described here this measurement is automated by a Labview program which sweeps the frequency of the generator and reads out the measured voltage response of the oscillator from a lock-in amplifier. The data is then fitted to a Lorentzian function in order to determine the resonant frequency, the width and any nuisance background signals. These backgrounds arise from the circuitry used and for instance have been measured to scale linearly with the applied drive.
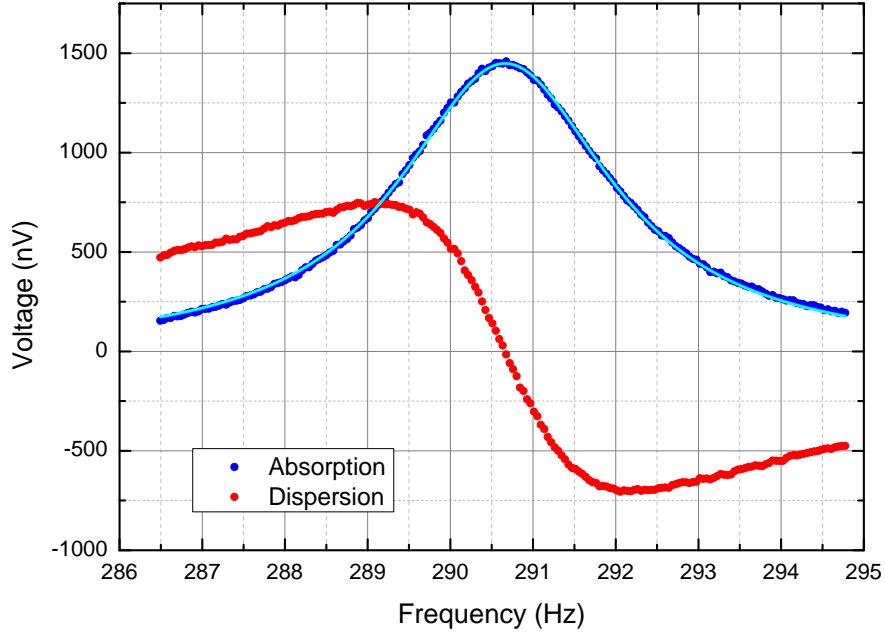
Figure 4.19: A typical frequency sweep performed on a $4.5\,\mu$m wire at approximately $160\,\mu$K. The bright blue line is the Lorentzian fit.

4.5.4 AC drive sweeping techniques

A drive sweep measures the response of an oscillator as a function of increasing drive amplitude. In our measurements the oscillator is set to its resonance frequency by a Labview automated program which also controls the generator providing excitation to the device. The response of the device is measured by a lock-in amplifier. After the measurement the drive is slightly increased followed by a short delay before the next measurement. This delay is necessary to allow the oscillator to settle (avoiding ringing). If the device backgrounds are known, then the program removes them from the absorption and dispersion signals. This enhances the accuracy of determining the resonant frequency of the device. This is done by minimising the ratio of dispersion vs. the absorption signal.

This type of measurement can also be used to measure the drive dependent backgrounds of a device. In the case of vibrating wires the background is measured in zero magnetic field and the drive sweep is performed at the resonant frequency of
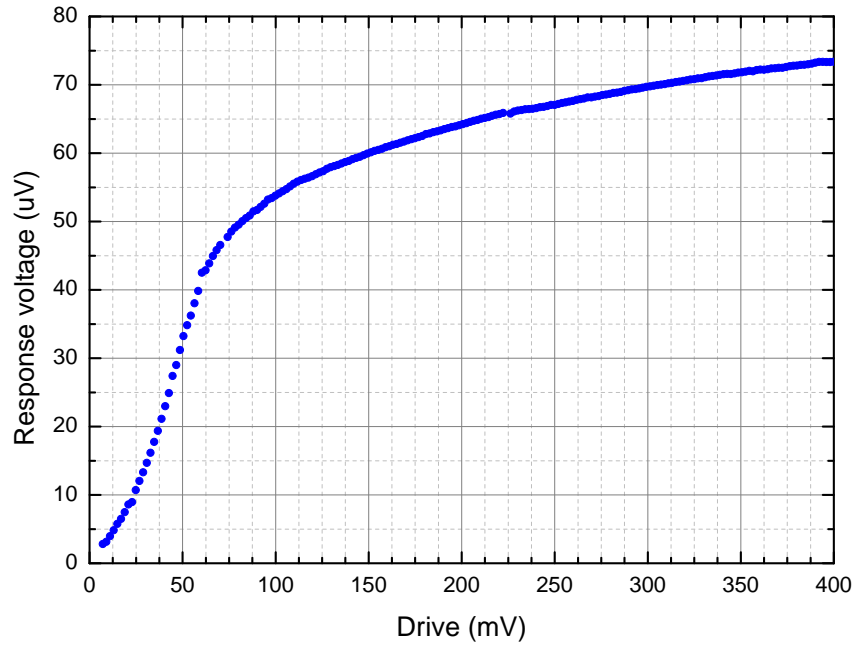
Figure 4.20: A typical drive sweep performed on a $4.5\,\mu$m diameter wire in ^{3}He-B at approximately $160\,\mu$K.

the wire. In the case of tuning forks two drive sweeps are performed at frequencies on either side of the resonant frequency, outside the damping width where the oscillator signal is smaller than the background signal. Both of these sweeps are at least $10\Delta f$ away from the resonance frequency, one above and one below. The average of these two sweeps is then considered as a proxy for the background that would be measured at the resonance.

Chapter 5

^{3}He-B gap anisotropy measurements

5.1 Introduction

The first set of experiments presented here probed the energy gap, a fundamental property of any superfluid condensate. From section 3.2.2 we know that the energy gap of ^{3}He-B is isotropic, unless there is an applied external magnetic field in which case the energy gap becomes distorted, reducing in the direction parallel to the external magnetic field. We have found that we are able to measure the magnitude of the distortion of the energy gap with tuning forks. Furthermore, we were able to determine the flow enhancement factor β of the superfluid backflow around the tuning fork. The experiments were performed in the tail piece of the experimental cell (shown in figure 4.9) containing the tuning fork array, and the external field is provided by the AB magnet.

The energy gap of ^{3}He-B in the bulk liquid at zero magnetic field is completely isotropic in momentum space. However, close to any surface, the energy gap reduces to zero owing to the fact that the Cooper pairs with orbital momentum vector parallel to the wall cannot exist. This energy gap suppression creates excitation states with energies lower than the energy of the superfluid gap. These states are called Andreev bound states (AB states) [56]. The dispersion curves of Andreev bound states and bulk excitations for stationary superfluid are shown in figure 5.1.

As mentioned in section 3.4, when an object is moving at velocity v with respect to the fluid, in the object's rest frame, the dispersion curves shift due to Galilean transformations by $\pm p_F v$. The liquid close to the surface of the object is moving at velocity βv relative to the object owing to the geometry of potential backflow around the object. The dispersion curve out in the bulk has a minimum energy of $\Delta - p_F v$ along the line of relative motion of the object and bulk liquid. When

$$(1 + \beta)p_F v = \Delta \tag{5.1}$$

quasiparticles created near the object surface can escape into the bulk, giving a
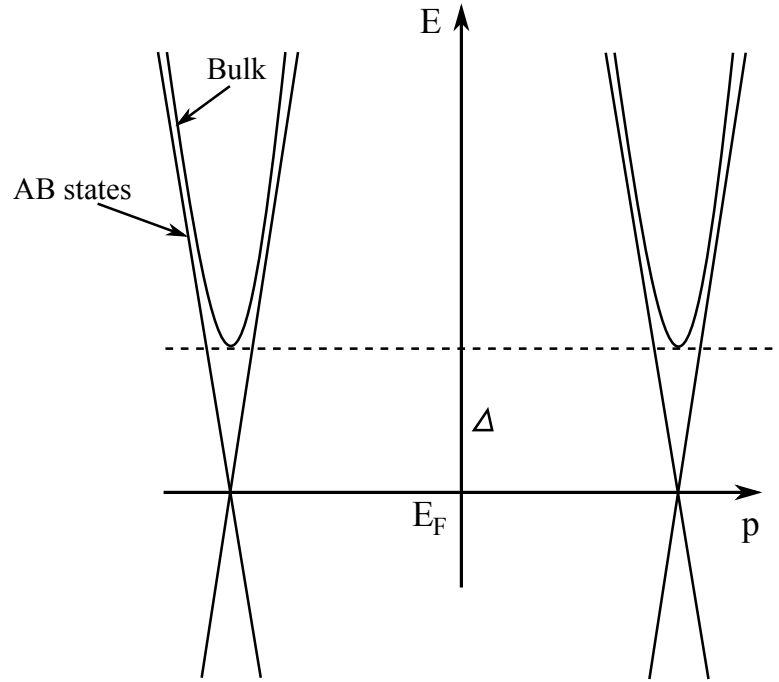
Figure 5.1: Dispersion curves for stationary fluid
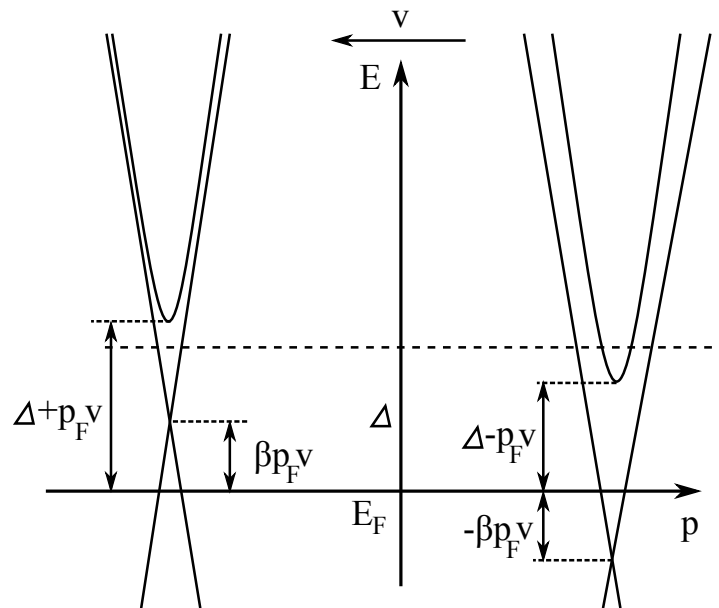
Figure 5.2: Moving object with the velocity v

critical velocity

$$v_c = \frac{\Delta}{(1+\beta)p_F}.$$ (5.2)

By determining this velocity, one can infer the magnitude of the energy gap. In

the experiment we utilised two out of the nine tuning forks as probes to measure the dependence of the critical velocity, and therefore the energy gap, on external magnetic field. Figure 4.9 shows a cross section of the tail piece with all fork positions and their orientation. The most suitable tuning forks for the experiment are forks 6 and 7. These two forks are in the same magnetic field, and due to their different orientations they are ideal to probe the size of the energy gap (figure 5.3 shows a model of the experiment). For convenience we will name these forks according to the direction of their prong oscillations as the vertical and the horizontal tuning fork, respectively.
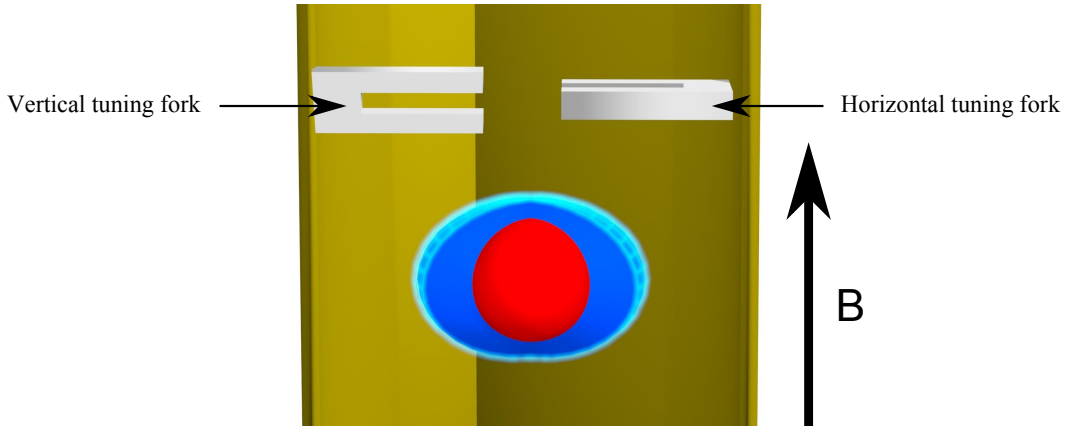
Figure 5.3: Close up of the horizontal and vertical tuning forks within the tail piece and a theoretical representation of the gap distortion.

5.2 Critical velocity measurements

After reaching ultra-low temperatures (approximately $178\,\mu$K), measured by a $4.5\,\mu$m thermometer wire, the resonance frequency of both tuning forks was determined by a frequency sweep prior to the main measurement. The frequency sweeps are shown in figure 5.4, giving resonance frequencies of $31.987\,$kHz and $31.211\,$kHz for the vertical and the horizontal tuning forks, respectively. This is a necessity in order to ensure the correct set-up for the following drive sweep of the device.

The drive sweep measurement technique was described in more detail in section
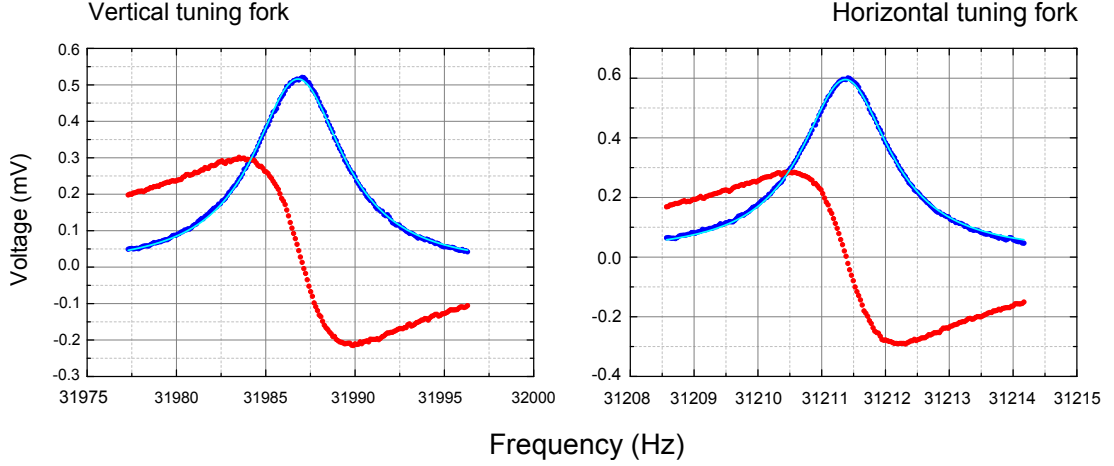
Figure 5.4: Frequency sweeps of vertical and horizontal tuning forks in ^{3}He-B at $178\,\mu$K. The bright blue lines are the Lorentzian fits.

4.5.4. Recalling equations (4.30) and (4.31) we can calculate the velocity of the fork prong from the measured signal and force acting on the prong from the applied drive.

The highest magnetic field of the experiment was set to be approximately $330\,$mT. After reaching the highest field the AB magnet power supply was set to ramp down at a very low rate providing enough time for the measurement programs to measure drive sweeps at quasi-static magnetic fields. The lowest magnetic field was $44\,$mT. This magnetic field is that of the main magnet after the demagnetisation. The drive sweeps performed at this field are shown in figure 5.5.

The first step of the analysis was to successfully determine the critical velocity from the drive sweeps. The last two drive sweeps (ones in the lowest field) will be used here as models to demonstrate the methods used to determine the critical velocity. There are three main methods used in determining the critical velocity. In the following subsections we will describe these methods using our model data.
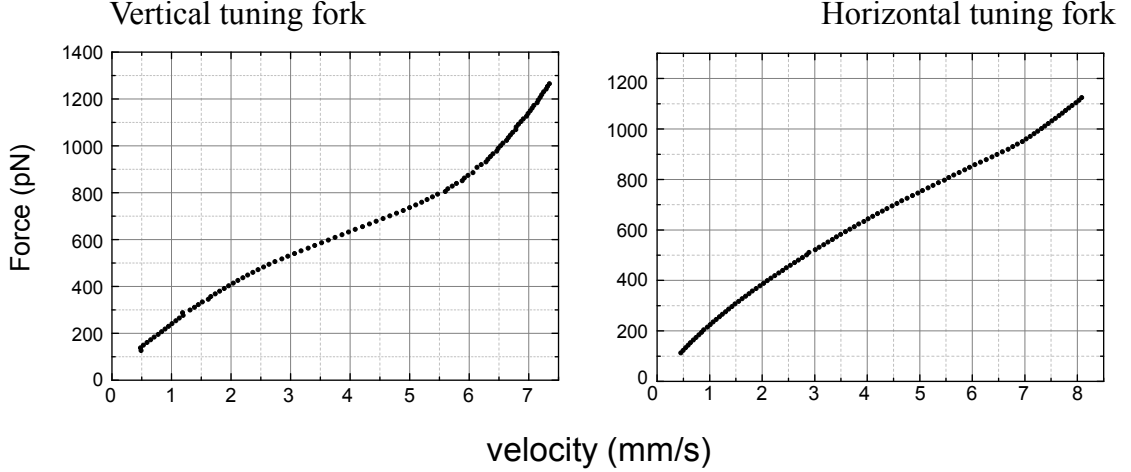
Figure 5.5: Drive sweeps of vertical and horizontal tuning forks at $44\,\text{mT}$ remnant field.

5.2.1 Point of inflection

The first method is more of a mathematical approach to locating the critical velocity. The thermal force F_{TH} (equation (3.42)) is a concave function reaching maximum of

$$(F_{TH})_{MAX} = 2p_F \gamma Ag(E_F)v_F k_B T e^{-\frac{\Delta}{k_B T}}, \tag{5.3}$$

for $v \to \infty$. When the critical velocity is reached, pair breaking begins which leads to a rapid increase in the damping of the fork. Thus, the function becomes convex. Therefore, the velocity coordinate of the point of inflection can be considered as a candidate for the critical velocity. The drive sweep is fitted by a high order polynomial (usually 6th to 8th order). The function is then differentiated twice in order to identify the inflection point (figure 5.6). The strong dependence on the quality of the data and the fit makes this method more susceptible to incorrectly identifying multiple critical velocities (finding more inflection points due to noise or bad fit) or finding completely unrealistic ones. The method usually underestimates the critical velocity. In the data presented here, this method was used to give us the "low limit" of the critical velocity.
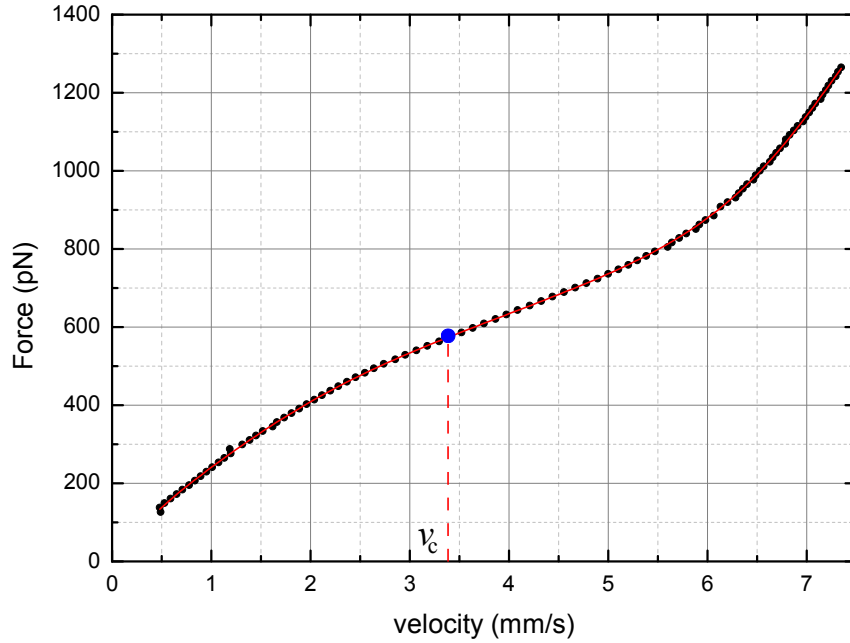
Figure 5.6: Drive sweep of the vertical tuning fork. The red line is the polynomial fit and the inflection point is indicated by the blue circle.

5.2.2 Linear approximation

This method approximates that the pair breaking region and the high viscosity thermal force both are a linear function of increasing velocity. Both the high viscosity thermal force and pair breaking region are fitted with linear functions. The critical velocity is then determined as the crossing point of the two linear fits shown in figure 5.7. The main flaw of this method is that it always overestimates the critical velocity. We use it to identify the "high limit" of the critical velocity.
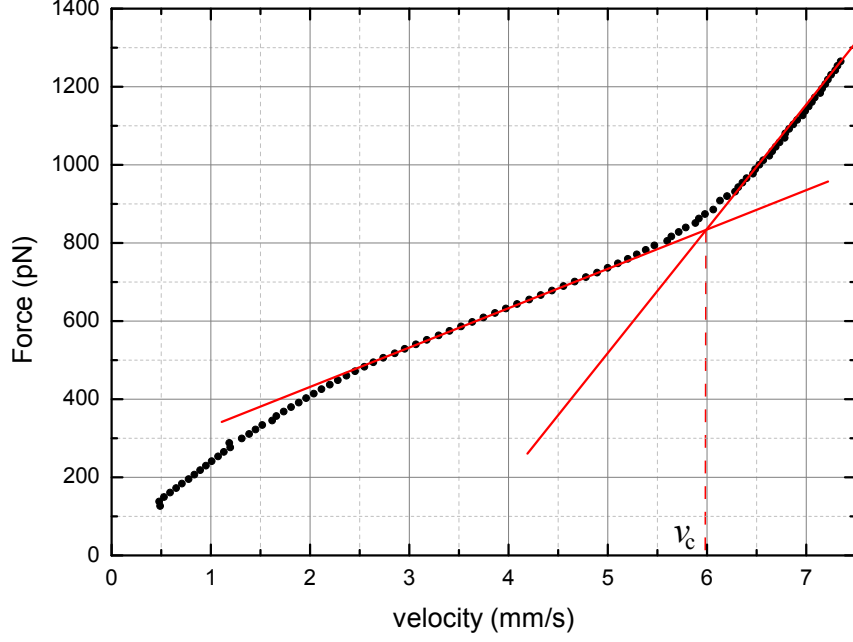
Figure 5.7: Drive sweep of vertical tuning fork with linear fits of thermal force and pair breaking force.

5.2.3 Force splitting

The most reliable method that we use focuses on splitting the damping force acting on the fork into all its components. Recalling from subsection 4.4.1 the total damping force can be written as

$$F_D = F_{IN} + F_{TH} + F_{PB}. \tag{4.19}$$

The intrinsic and the pair breaking forces are constant with temperature. The pair-breaking force is equal to zero when $v < v_C$. The thermal force is the only force depending on temperature. Recalling equation (3.42) we can write

$$F_{TH} = F_t = b(1 - e^{-\frac{\lambda p_f v}{k_B T}}). \tag{5.4}$$

Differentiating this equation with respect to velocity and rearranging for b we obtain

$$b = \frac{k_B T}{\lambda p_F} \frac{dF_t}{dv} e^{\frac{\lambda p_F v}{k_B T}}. \tag{5.5}$$

In the limit $v \to 0$ we obtain

$$b = \frac{k_B T}{\lambda p_F} \frac{dF_t}{dv}\bigg|_{v=0}.$$ (5.6)

Recalling equations (4.16), (4.30) and (4.31) we can write

$$(HWD) = \frac{\Delta f v \alpha^2 G}{2 F_D A_t},$$ (5.7)

where we introduce constants of G and A_t to account for the actual circuit set-up. The constant G (Gain) is the enhancement of the response signal by the preamplifier and A_t (Attenuation) corresponds to reduction of the drive signal. The $\sqrt{2}$ comes from our use of RMS voltage and α is the fork constant.
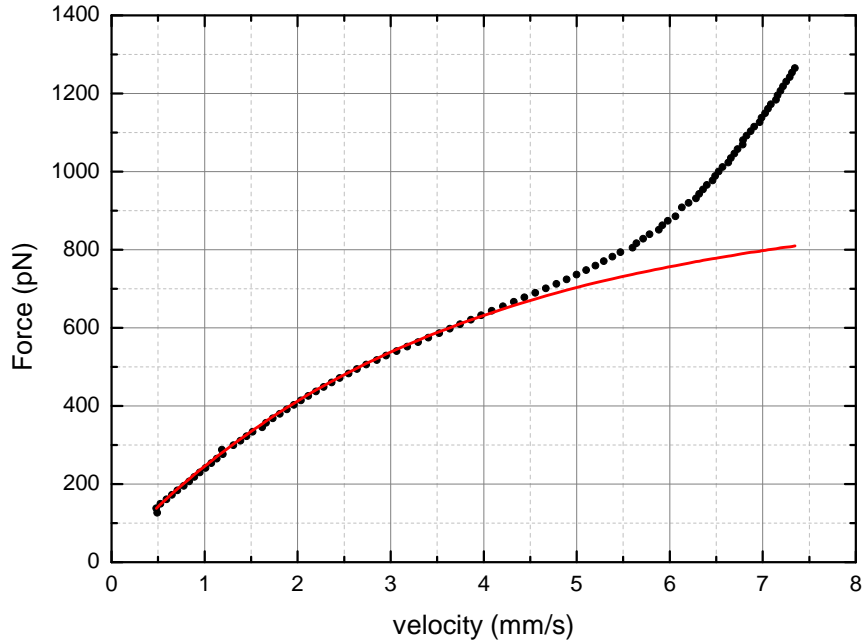
Figure 5.8: Drive sweep of the vertical tuning fork with thermal force fit.

Rearranging equation (5.7) for $\frac{F_D}{v}$ we get

$$\frac{F_D}{v} = \frac{G}{2 A_t} \frac{\Delta f \alpha^2}{(HWD)}.$$ (5.8)

78

At low velocities and temperatures the total damping $F_D = F_t$. Substituting now equation (5.8) into equation (5.4) we get

$$F_t = \frac{G}{2A_t} \frac{\Delta f \alpha^2}{HWD} \frac{k_B T}{\lambda p_F} (1 - e^{-\frac{\lambda p_f v}{k_B T}}).$$ (5.9)

Now λ is the only fitting parameter. Measuring directly the width of the tuning
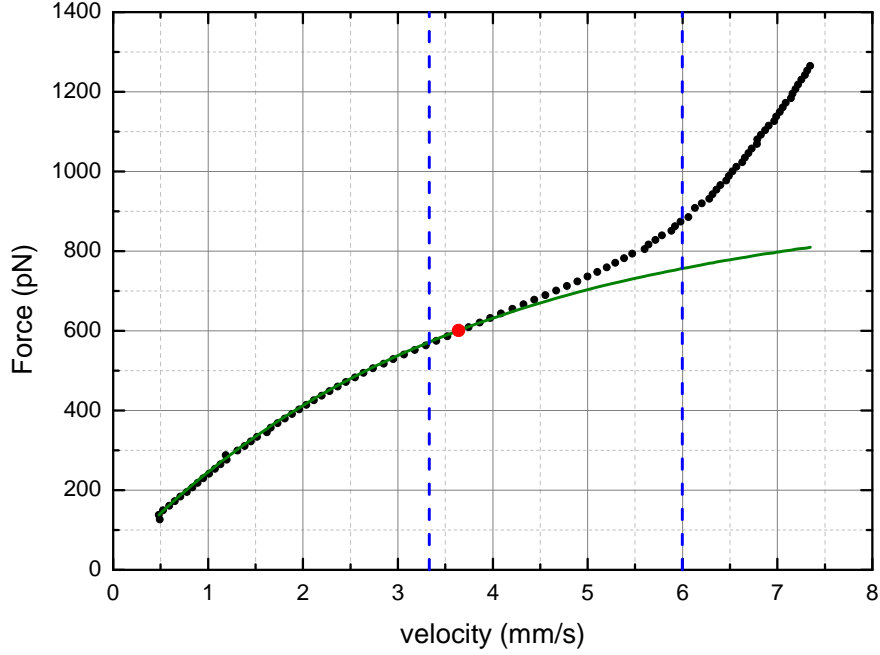
Figure 5.9: Analysis of the drive sweep of the vertical tuning fork (at a field of $44\,\text{mT}$ and temperature of $188.4\,\mu\text{K}$). The two dashed lines determine the critical velocity interval (boundaries obtained from point of inflexion and linear approximation methods), the red circle corresponds to the critical velocity, the green curve is the thermal fit. .

fork while sweeping the drive is very difficult. Instead we use the inferred width of the tuning fork from the width of a nearby $4.5\,\mu\text{m}$ wire which served as a thermometer. When the fork is driven to high velocities the temperature around it is changing dramatically. This change is registered by the thermometer wire. By calibrating the tuning fork with respect to the thermometer wire on a separate warm up we can find the relation between the width of the tuning fork and the

width of the thermometer wire.
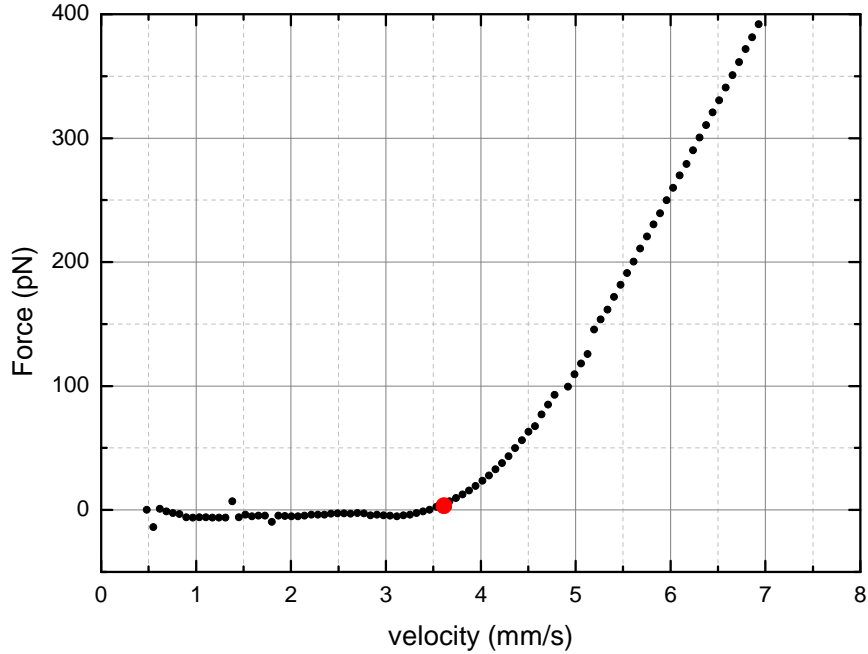
Figure 5.10: Drive sweep of vertical tuning fork after thermal force subtraction. The red circle corresponds to the critical velocity.

Once the thermal force has been determined we can subtract it from the total damping force. The remaining force is the pair breaking force which becomes $F_{PB} > 0$ when $v = v_c$. This method provides the most reliable measurement of the critical velocity (shown in figure 5.10).

In our analysis we used all three methods to determine the critical velocity. As mentioned above the first two were used to give us the boundaries and the third method was then used to accurately determine the critical velocity shown in figures 5.9 and 5.10. It is worth noting here that the critical velocity measured for the tuning forks is rather small (order of $3.5\,\mathrm{mm\,s^{-1}}$) compared to critical velocities measured by vibrating wires (order of $9\,\mathrm{mm\,s^{-1}}$). This is due to the complex geometry of the tuning fork and therefore very different flow enhancement by the potential backflow. From the measurements of the critical velocity we estimate β to be on the order of 6 much larger than the calculated value for a vibrating wire.
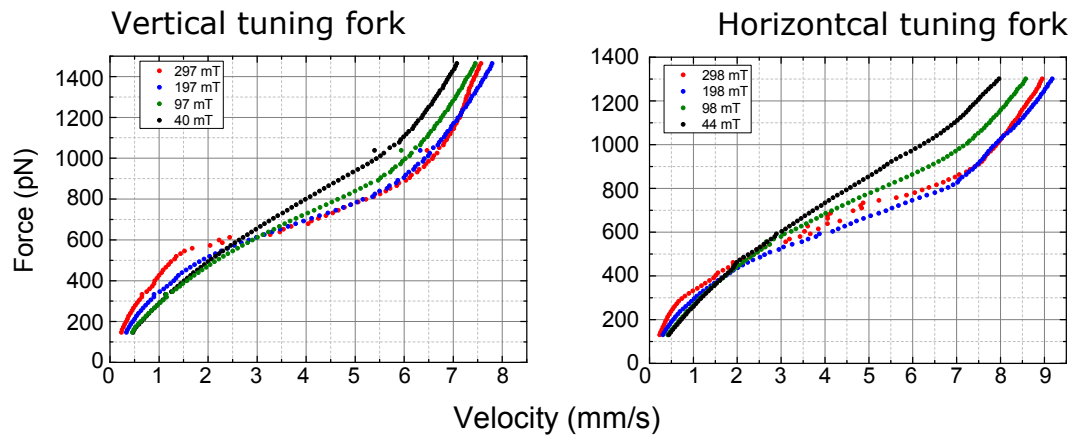
Figure 5.11: Examples of drive sweeps of vertical and horizontal tuning forks in different magnetic fields. The black sweep is at $44\,\mathrm{mT}$ magnetic field. During these measurements the temperature changed from $178\,\mu\mathrm{K}$ to $188\,\mu\mathrm{K}$.

The analysis process was automated by writing Matlab and Python programs which analysed all of the drive sweeps in different magnetic fields for both tuning forks. Examples of drive sweeps are shown in figure 5.11.

5.3 Results
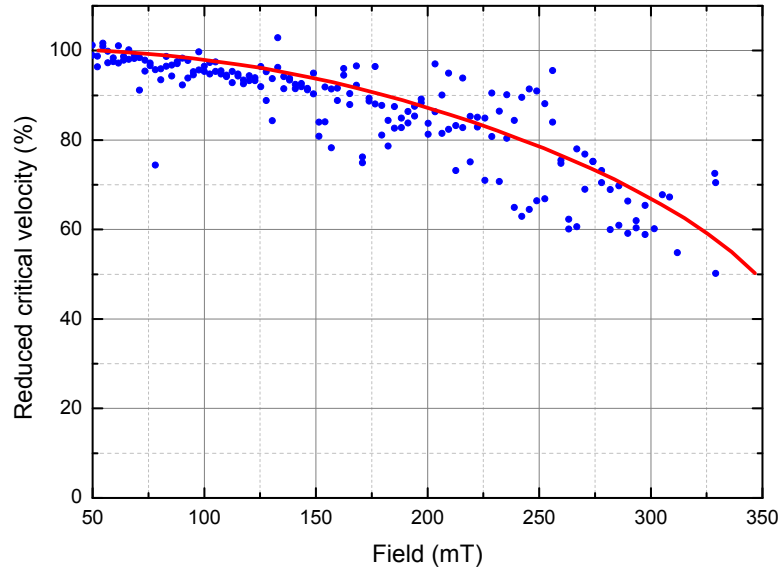
Figure 5.12: The reduced critical velocity of the vertical tuning fork as a function of magnetic field. The red line is a theoretical fit (5.10) giving $\beta = 6$.

During the measurements the temperature changed from $178\,\mu\text{K}$ to $188\,\mu\text{K}$. For convenience the results are in the form of a reduced critical velocity given by the measured critical velocity relative to the critical velocity at the lowest magnetic field where the gap is assumed to be isotropic. The results are shown in figures 5.12 and 5.13

The vertical tuning fork shows a drop in the critical velocity to almost 60% of the original critical velocity with increasing field, clearly showing the change in the size of the energy gap with magnetic field (figure 5.12). On the other hand the critical velocity of the horizontal tuning fork stays around the original value (figure 5.13). The extra scatter of the horizontal tuning fork comes from difficulties in determining the critical velocity at higher magnetic fields. This is discussed in section 5.4.

Our results show good agreement with results of a similar experiment on a vibrating wire that was previously conducted and is shown in figure 5.14. In
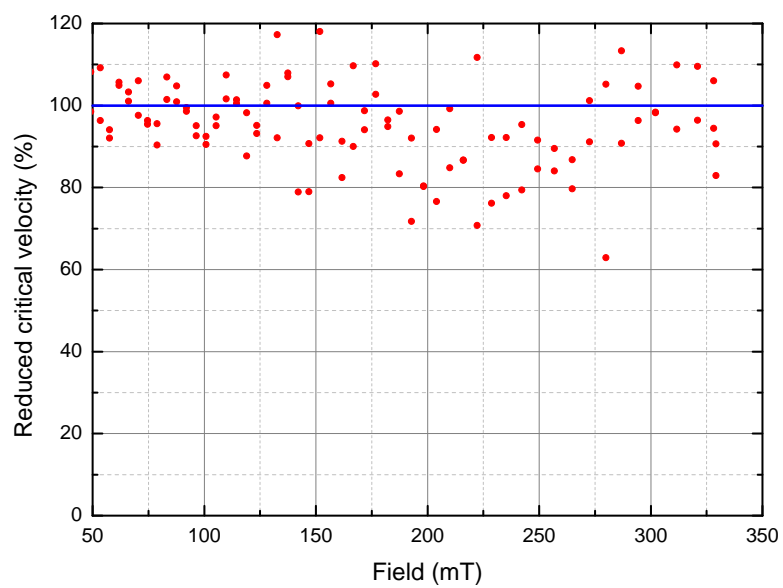
Figure 5.13: The reduced critical velocity of the horizontal tuning fork as a function of magnetic field.
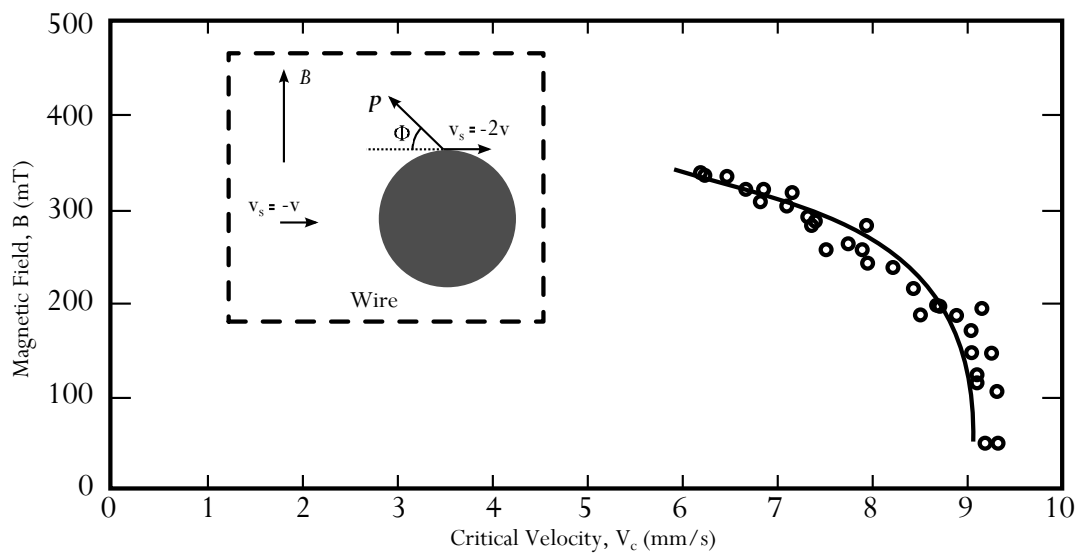
Figure 5.14: The critical velocity of a vibrating wire as a function of magnetic field. [3]

both cases the data was fitted by a theoretical prediction by Nagai et.al. [57, 58]

following minimisation of

$$v_c = \left\{ \frac{\sqrt{\left(\sqrt{\xi^2 + \Delta_\parallel^2 \sin^2 \Phi} - \sigma \hbar \tilde{\omega}_L\right)^2 + \Delta_\perp^2 \cos^2 \Phi}}{p_F(\beta + \cos \Phi)} \right\}_{min} . \qquad (5.10)$$

Note that β is the flow enhancement factor mentioned in equation (5.2) and ξ is the energy of a quasiparticle. $\Delta_\parallel$ and $\Delta_\perp$ are the theoretical magnitudes of the gap parallel and perpendicular to the external magnetic field (see Appendix A), $\tilde{\omega}_L$ is the Larmor frequency and $\sigma = \pm\frac{1}{2}$ is the spin of the quasiparticle. This equation is solved numerically as a function of magnetic field. The angle Φ changes from $0°$ for small velocities to $90°$ for high velocities. Using $\beta = 2$ and $\beta = 6$ for vibrating wire and tuning fork, respectively. We think that the large flow enhancement factor for tuning forks comes from the complicated geometry of the device (i.e. plenty of sharp corners), and from the quadrupolar flow around the fork prongs.
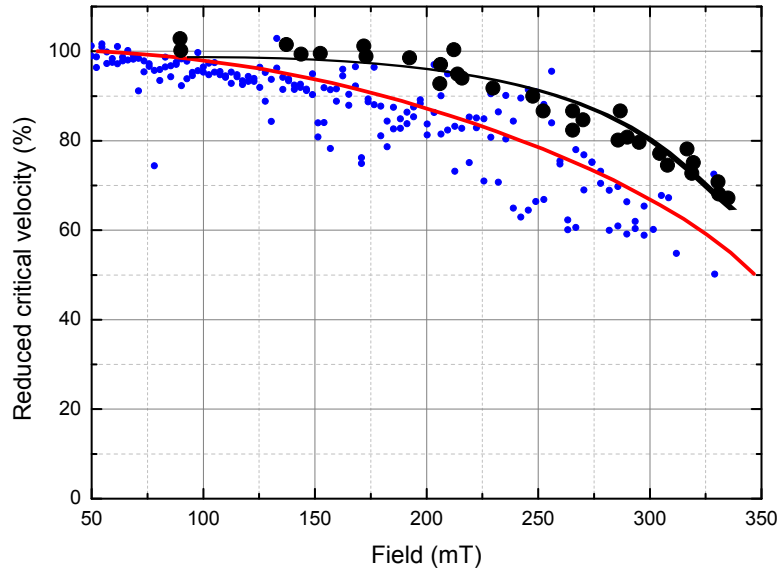
Figure 5.15: Comparison between the vertical tuning fork measurement (blue circles) and the vibrating wire measurement (black circles) [3]. The red and black lines are theoretical fits using (5.10) giving $\beta = 6$ for the tuning fork and $\beta = 2$ for the vibrating wire.

The tuning fork proves to be a very effective tool in sensing the changes in the energy gap of ^{3}He-B in magnetic field. However, for the vibrating wire, it

seems that the smallest energy gap is selected for the breaking of Cooper pairs, even though the wire velocity is perpendicular to the applied magnetic field (the direction of highest gap suppression). In contrast our measurements show that for tuning forks the critical velocity is set by the size of the energy gap in the direction of the prong velocity.

5.4 High magnetic field amplitude sweeps

At high magnetic fields we have observed anomalous behaviour of the force-velocity curves, shown in figure 5.16. This behaviour led to many difficulties in determining the critical velocity of the tuning fork, hence the large spread of data at high magnetic fields.
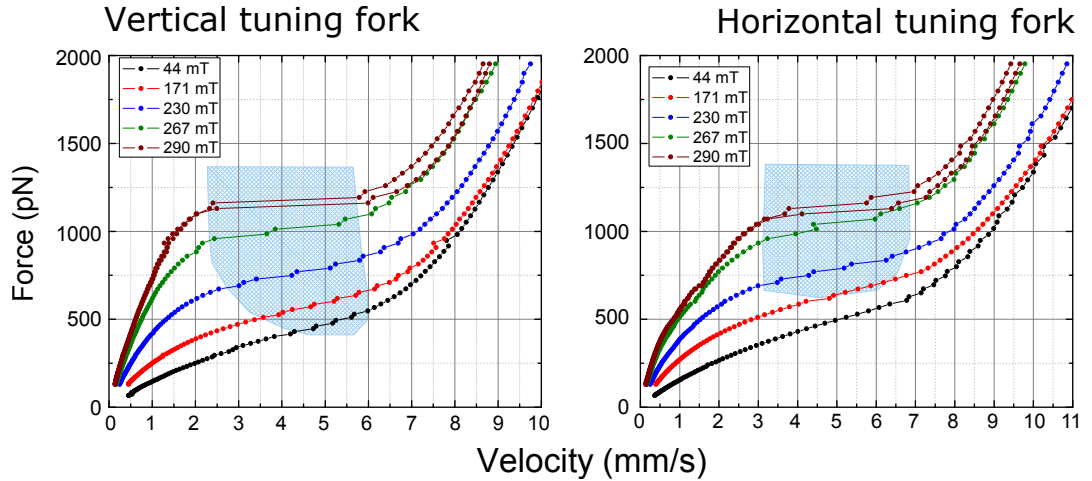
Figure 5.16: Vertical and horizontal tuning fork drive sweeps in high magnetic fields. Black curves correspond to drive sweeps in $44\,\mathrm{mT}$ field. The highlighted region represents shielding. The temperature varies from $178\,\mu\mathrm{K}$ to $188\,\mu\mathrm{K}$.

We posit that the process responsible for this behaviour is some form of quasiparticle shielding similar to recently measured quasiparticle shielding by quantum turbulence of the flopper [59], shown in figure 5.17.

In the case of the flopper the shielding is temperature dependant. As it moves through superfluid ^{3}He-B the wire creates a large region of quantum turbulence. This turbulent tangle in turn "protects" the wire from any incoming excitations

that could provide additional damping and also it prevents excitations from escaping and carrying away the energy of the wire. This self-screening reduces the damping force on the flopper which is seen as a large jump in the velocity on the force velocity diagram.

In the case of tuning forks, however, this effect is not temperature dependant but is magnetic field dependant. Unfortunately, the direct mechanism of this shielding is unknown. We speculate that due to the high magnetic field and local increase of the temperature around the prongs of the fork we are able to nucleate ^{3}He-A phase on the tuning fork. Another possibility is that the motion of the tuning fork itself strongly depends on the magnetic field [60]. Also it might be a new type of vortex or topological defect that exists at high field only. Further investigation needs to be carried out.
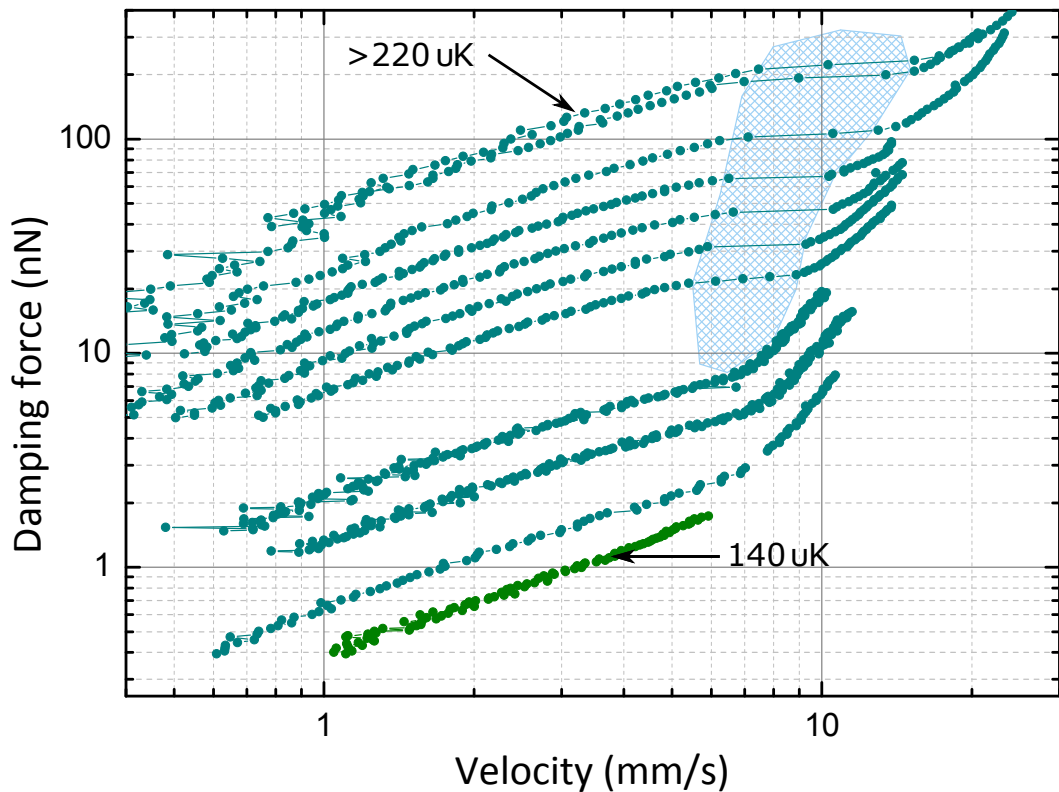
Figure 5.17: Shielding effect of the flopper. Here shielding by vortices is dependant on the temperature. The highlighted region represents shielding. Higher damping force is measured at higher temperatures.

Chapter 6

Landau critical velocity measurement

6.1 Introduction

The flexibility that we have in controlling the flopper allows us to investigate whether there is a difference between oscillatory motion and linear motion at constant velocity through superfluid ^{3}He-B. The flopper experimental arrangement was shown in figure 4.14. The experiments are performed at 0 bar. The usual demagnetisation process ended in the magnetic field of 77 mT for the inner cell. During this process the inner cell cools down to approximately 140 μK. The first step after reaching the ultra-low temperatures was to frequency sweep the flopper and 4.5 μm thermometer wires. The frequency sweep of the flopper is shown in figure 6.1. Due to the sheer size of the wire, the frequency sweep had to be
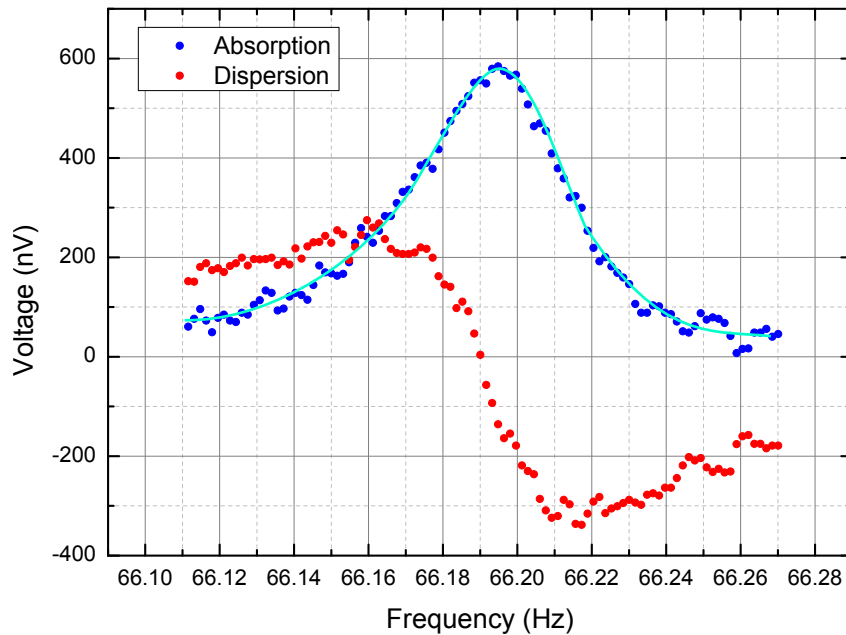
Figure 6.1: Flopper frequency sweep. The resonance frequency is 66.19 Hz, its full width at half maximum is ≈ 0.05 Hz giving a Q-factor of ≈ 1320. The bright blue line is the Lorentzian fit.

performed at very low drives to avoid heating of the cell. However, low drive amplitudes mean that the flopper is very lightly damped, which can result in unwanted ringing of the flopper. In order to avoid this effect the frequency sweeps and later the drive sweeps were carried out slowly, leaving enough time for the flopper to settle. Frequency sweeps took roughly $3-5$ minutes and drive sweeps

took around 10 minutes to complete. As in the previous experiment, the frequency sweep is necessary to ensure that the drive sweep is using the correct resonance frequency and that the backgrounds are accounted for and correctly subtracted.
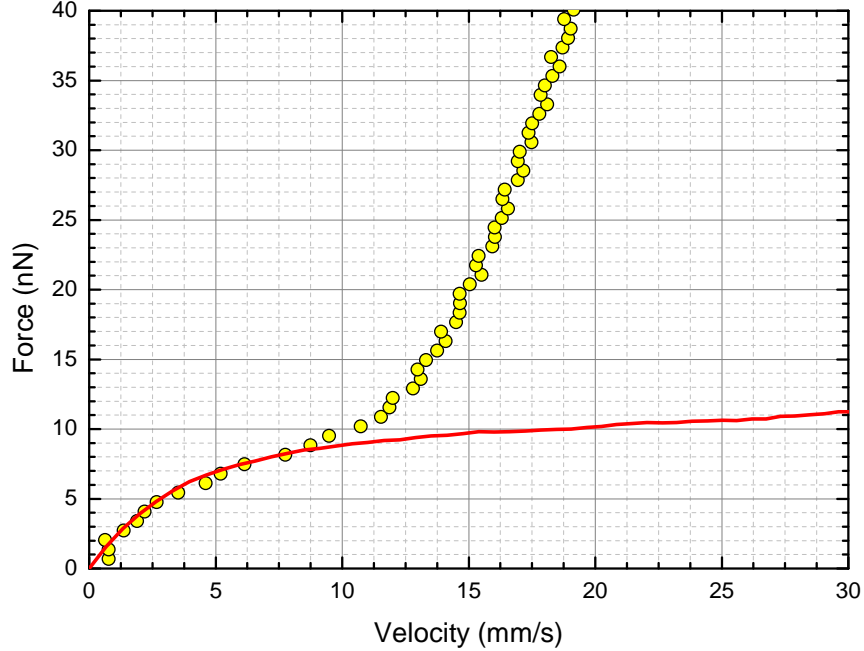
Figure 6.2: Flopper drive sweep with thermal damping fit (red line) at $155\,\mu$K.

The next step is the drive sweep of the flopper. The velocity of the flopper and the damping force are derived from the measured voltage and the drive current (using equations (4.28) and (4.25)). A typical drive sweep at the temperature of $155\,\mu$K is shown in figure 6.2. All of the previously described methods of drive sweep analysis are applicable to the flopper and here we used the force splitting method as it is the most accurate. For the flopper the equation describing the (HWD) parameter (4.16) is rewritten as

$$\frac{F}{v} = (BD)^2 \frac{\Delta f}{(HWD)},\qquad (6.1)$$

where B is the magnetic field and D is the leg spacing of the wire. Combining

equation (5.6) with equation (6.1) we get the thermal force

$$F_t = (BD)^2 \frac{\Delta f}{(HWD)} \frac{k_B T}{\lambda p_F} (1 - e^{-\frac{\lambda p_F v}{k_B T}}).$$ (6.2)

Here Δf is the inferred damping width of the flopper from the width of a nearby $4.5\,\mu$m which served as a thermometer.
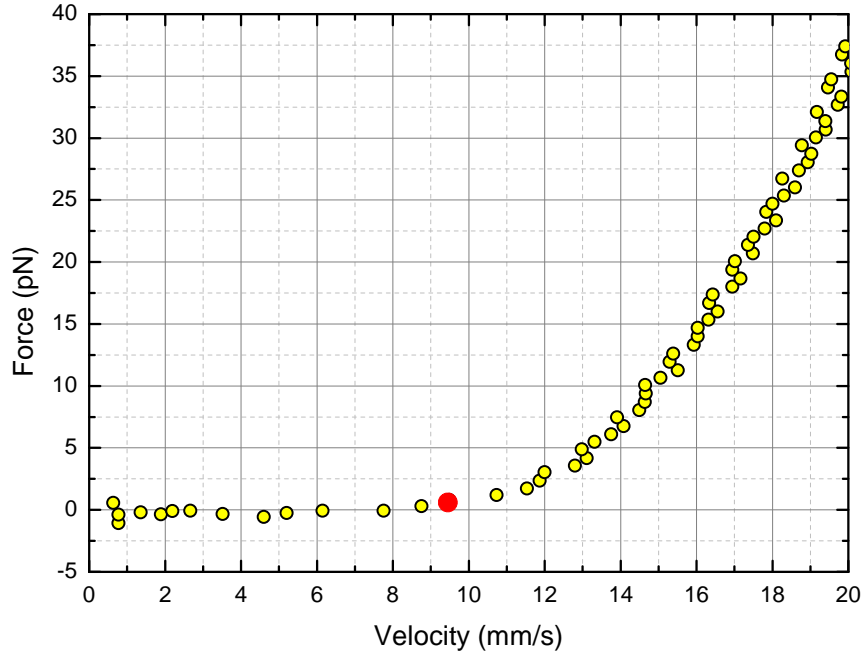
Figure 6.3: The drive sweep after thermal force subtraction. In this figure the increase in damping at critical velocity of $9\,\mathrm{mm\,s^{-1}}$ is clearly visible.

As mentioned in chapter 2 the critical velocity of $9\,\mathrm{mm\,s^{-1}}$ is expected if we consider the velocity enhancement of pure potential backflow around the wire (subsection 4.4.6).

6.2 DC measurements

We now turn to the DC measurements of the flopper. These were performed in strokes controlled and measured by a single LabView automated program. The program calculates the drive profile necessary for each predetermined stroke and applies it via data acquisition (DAQ) card to the DC input of the current supply. At the same time the DAQ card is reading its own output as well as outputs of all lock-in amplifiers measuring signals from the pick-up coils and $4.5\,\mu$m thermometer wire. The high frequency probe current of $96\,$kHz is supplied into the AC input of the current supply from a manually set generator. However, before any measurements can be taken it is necessary to consider whether all the settings are appropriate for the upcoming measurements. In order to accurately perform these DC strokes it was necessary to calibrate the induced voltage on the pick-up coils to deduce the position of the flopper. Another thing to consider are the sample rate and lock-in time constants. For our type of measurement we found that the most suitable sample rate for each stroke was $10\,$kHz. The lock-in time constants were selected considering the sample rate of the DAQ card. The whole measurement session lasted for 10 seconds giving approximately 4 seconds of backgrounds before and after the stroke. The strokes themselves were very short (usually on the order of a few tens of milliseconds) depending on the target velocity.

6.2.1 Flopper position calibrations

Selecting one of the coils as coil 1 and the other one as coil 2. Then the position of the flopper crossbar with respect to the detection coils is defined by two vectors $\mathbf{r}_1$ and $-\mathbf{r}_2$. For the distance between the coils we can write $\mathbf{r}_{12} = \mathbf{r}_1 + \mathbf{r}_2$. The voltage induced in coil 1 due to the flopper motion is expressed in the form [60]

$$V_1 = -\frac{\partial}{\partial t}\left(M_1(\mathbf{r}_1(t))\,I_w\right) - M_{12}\frac{\partial I_2}{\partial t} - L_1\frac{\partial I_1}{\partial t}, \tag{6.3}$$

where $M_1(\mathbf{r}_1)$ is the mutual inductance between coil 1 and the flopper, $\mathbf{r}_1 = \mathbf{r}_1(t)$ is the vector defining the distance between coil 1 and the flopper, M_{12} is the mutual inductance of the two detection coils, I_2 is the current flowing through the coil 2, I_w is the current flowing through the flopper and L_1 is the inductance of the coil 1. This current is a superposition of two currents: a current linearly increasing in time and a harmonic high frequency current $I_w = k_0 t + I_{AC}\sin(\omega t)$. Experimentally this is done by adding a high frequency signal of 96.4 kHz to the linear drive. The last term characterizes the contribution from coil 1 itself due to current I_1 flowing through it. The second and third terms in equation (6.3) are small and can be neglected. Then equation (6.3) can be rewritten as

$$V_1 = -I_w \frac{\partial M_1(\mathbf{r}_1(t))}{\partial t} - M_1(\mathbf{r}_1(t))\frac{\partial I_w}{\partial t}, \tag{6.4}$$

Substituting for I_w we obtain

$$V_1(\mathbf{r}_1) = -k_0 \left[\frac{\partial M_1(\mathbf{r}_1)}{\partial \mathbf{r}_1} \frac{\partial \mathbf{r}_1}{\partial t} t + M(\mathbf{r}_1) \right] - I_{AC}\left[\frac{\partial M_1(\mathbf{r}_1)}{\partial \mathbf{r}_1} \frac{\partial \mathbf{r}_1}{\partial t}\sin(\omega t) + \omega M_1(\mathbf{r}_1)\cos(\omega t) \right] \tag{6.5}$$

for the induced voltage in coil 1. The induced voltage described by the first term of equation (6.5) is not detected by the lock-in amplifier as it is not oscillating at the reference frequency. The induced voltage described by the second term is detected. The second term consists of two harmonic components at frequency ω shifted in phase by 90 degrees with respect to each other. It consists of a velocity dependent and independent term. Assuming now that the flopper is moving very slowly, i.e., quasistationary then the flopper velocity term with respect to the coil can be neglected and what we are detecting is only the signal that depends on the position of the crossbar.

The DC drive is slowly increased until the flopper touches the wall of the cell, at this point the induced voltage in the pick-up coil stops increasing. The process is then repeated in the opposite direction (figure 6.4).

By knowing the current at these two extreme points and the distance travelled
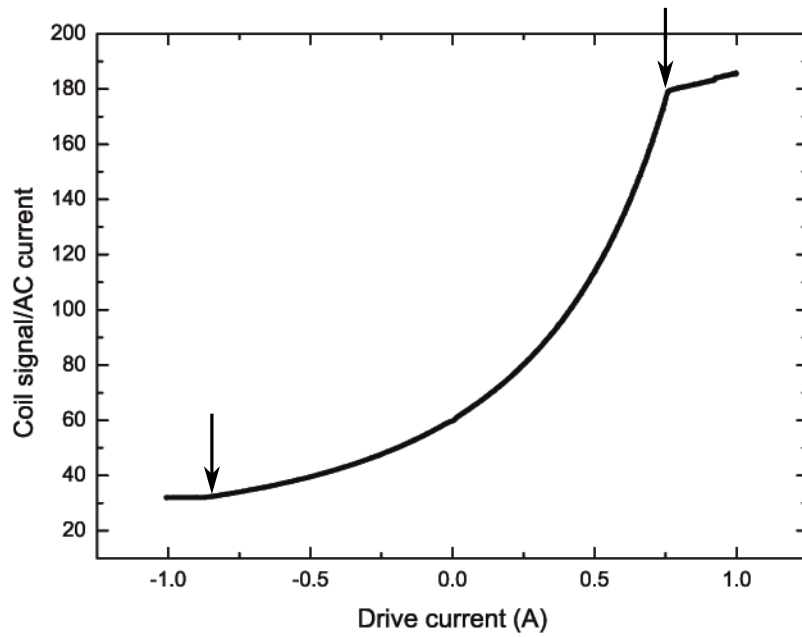
Figure 6.4: Signal from a pick up coil. The arrows are highlighting points at which flopper touches the walls of the experimental cell. The slight increase in the signal after the touch is due to the flopper being bent by the force.

by the flopper we can accurately determine the position of flopper crossbar for any DC current. The spring constant k of the flopper is another important factor determined in this calibration. Recalling section 4.4.1, if we stop the flopper just as it touches the wall then the driving force (Lorentz force) is equal to the restoring force of the wire, giving

$$k = \frac{BID}{x},$$ (6.6)

where B is the magnetic field, I is the drive current at which flopper touches the wall, D is the leg spacing of the flopper and x the displacement (distance from the central equilibrium position to the cell wall). Using equation (6.6) we get $k = 0.304 \, \mathrm{N \, m^{-1}}$.

6.2.2 Flopper force calibrations

The quantity we are able to measure most conveniently is the dissipation generated by the linear motion. Our first attempt was to directly determine the additional damping on the flopper as it moves through superfluid. This would be seen as a lag of the flopper wire behind its equilibrium position. However this technique proved to be impossible to use in our set-up due to a very small signal-to-noise ratio. The lag of the flopper due to additional damping was a very small distance, on the order of tens of micrometers, always smaller than the noise even after averaging over several strokes. In fact, the dissipation being so small helped us with the calculation of the driving force of the flopper as we could ignore it in comparison to the inertial force.

Instead of looking directly on the flopper we discovered that we were able to infer the dissipation as a temperature change (change in excitation density) on a nearby $4.5\,\mu\mathrm{m}$ thermometer wire. This provided a quantitative measure of the dissipation. Using the tuning fork, situated under the flopper, as a thermometer gave a consistency check, with similar results.

However, in order to determine the effective damping force, a calibration of the thermometer wire is necessary with respect to the energy dissipated by the flopper. To do this the flopper was driven by a series of AC burst pulses similar in duration to the actual DC strokes (shown in figure 6.5). To avoid ringing of the wire the drive current was very carefully profiled (also shown in figure 6.5). The induced voltage and the drive current of the flopper are measured by lock-in amplifiers at frequency of $66\,\mathrm{Hz}$. From the voltage and current we were able to determine the energy dissipated by the flopper. The width response of the thermometer wire was logged for each of these pulses, giving us the dependence of width change (quasiparticle density change) on energy dissipated by the flopper (figure 6.6). Note that for this calibration to work we have to assume that the whole energy delivered by the flopper is converted to ^{3}He-B thermal excitations and that the thermometer wire reacts to AC pulses in the same way as DC strokes. The
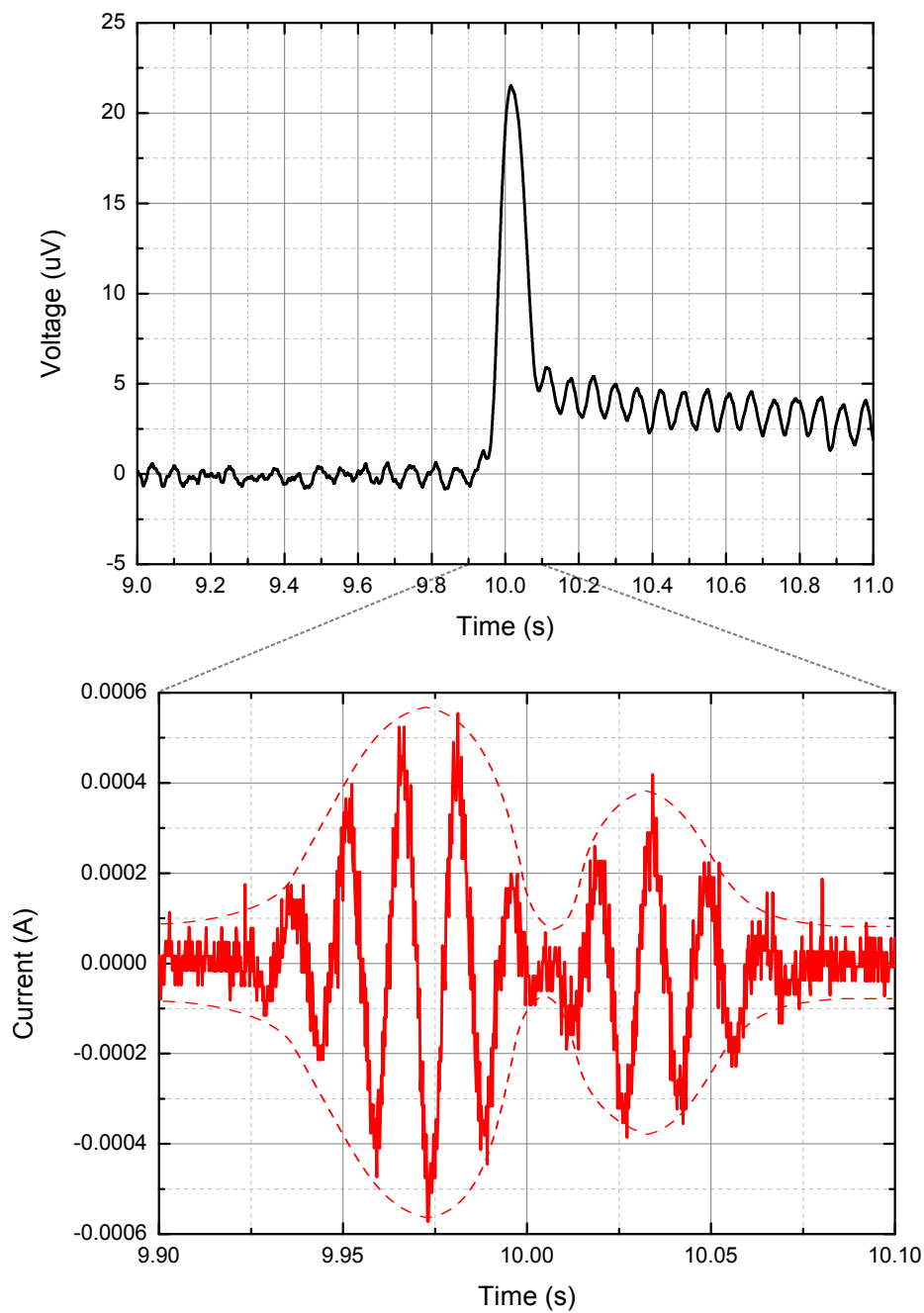
Figure 6.5: A typical AC calibration. The measured induced voltage in the flopper is shown in the top figure. The drive current supplied to the flopper is shown in the bottom figure.
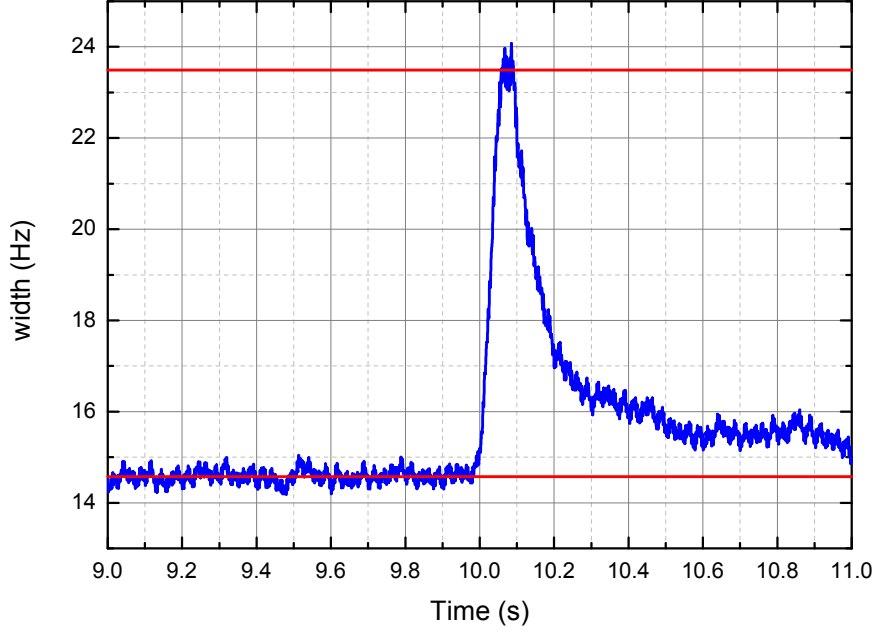
Figure 6.6: The response of the $4.5\,\mu$m thermometer wire to the AC burst. The lower red line corresponds to the background and the higher one to the average peak height, the difference between the two is the measured width change.

resulting width changes are plotted against the energy dissipated by the flopper (figure 6.7) and fitted by a function

$$E = A(d\Delta f - x_c)^p, \tag{6.7}$$

where $d\Delta f$ is the width change of the $4.5\,\mu$m wire and A, x_c, p are fitting parameters.

Knowing the energy calibration and the distance travelled by the flopper in DC motion we can then determine the damping force acting on the flopper itself. This requires one calibration constant which is determined by comparing the thermal damping force of the oscillatory motion with the calculated DC damping force at similar temperatures. Scaling down the calculated DC thermal damping force to match that of the AC measurements gives a value of 0.2 for the calibration constant.
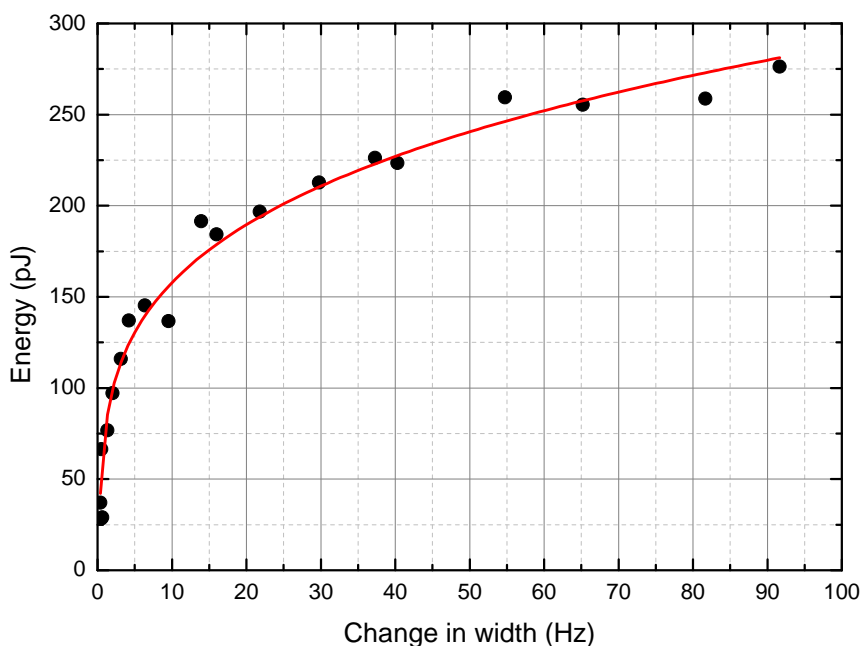
Figure 6.7: Width change on $4.5\,\mu$m wire as a function of energy. The red line is an power fit described in the text. Where $A = 8.86 \times 10^{-5}$, $x_c = 0.46$ and $P = 0.26$.

6.2.3 Flopper strokes

The backbone of the DC flopper measurement circuit (shown in figure 4.18) is the current supply. This current supply can deliver both positive and negative current, however, it brings large amounts of electric noise if the supply current is at 0 due to the current supply switching between two different circuits. This problem is easily avoided by changing the base current to some non-zero value therefore moving the flopper off the central position. Each stroke has a short acceleration period to get the flopper to the desired speed and deceleration period where the flopper is stopped. In the case of both acceleration and deceleration extra care was taken to avoid ringing of the flopper and to make sure the flopper never moved faster than the target DC velocity [53, 61]. A typical stroke is shown in figure 6.8.

After each stroke the flopper is very slowly returned to its starting position and then the whole process is repeated again. For DC motion it is important to select
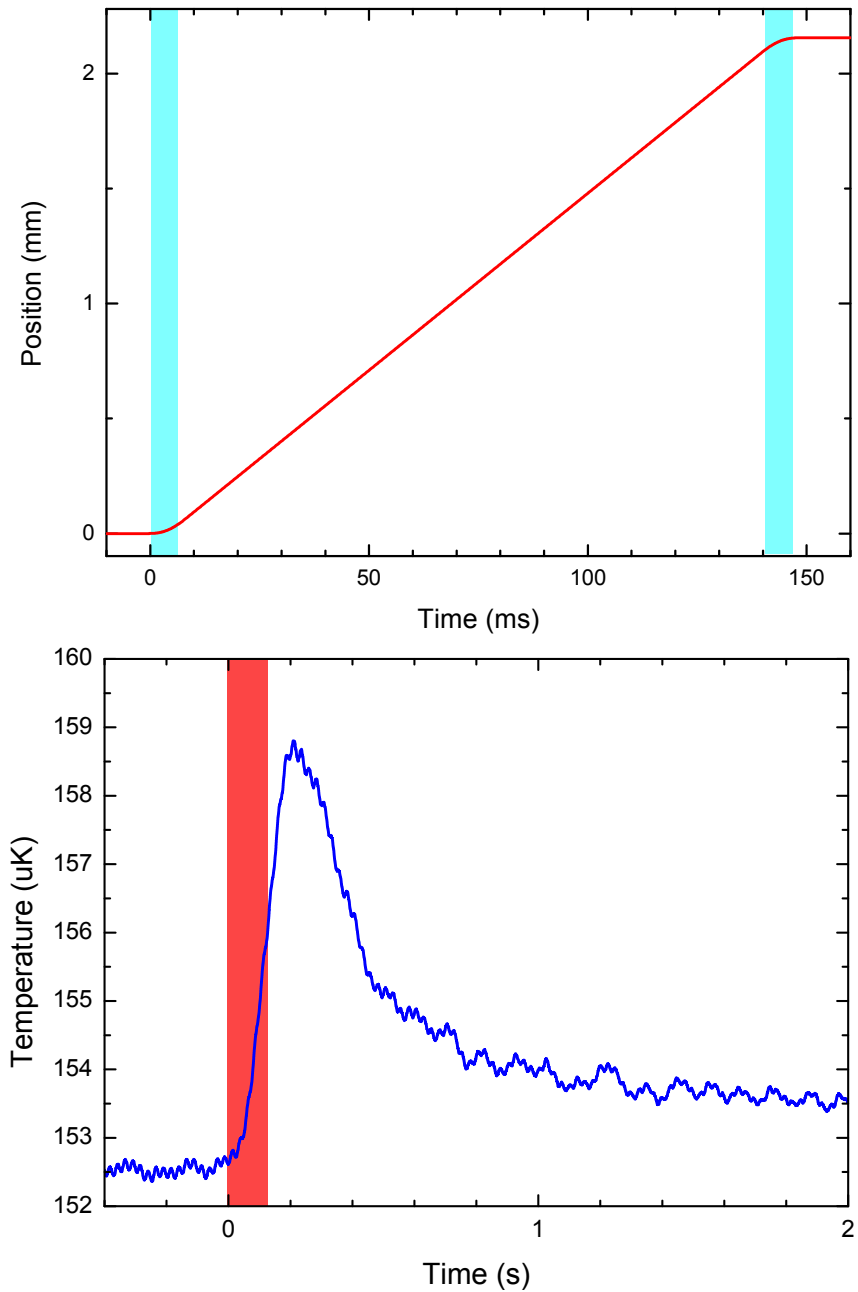
Figure 6.8: A standard stroke measured by the pick up coils. The flopper moved over distance of $2\,\mathrm{mm}$ at a speed of $15.4\,\mathrm{mm\,s^{-1}}$. The blue bands highlight the acceleration and deceleration periods. The figure below is showing the measured thermometer response with the red band highlighting the stroke time period.

the distance over which the flopper should move during each stroke. To do this we performed multiple stroke series for the flopper moving at same velocities over different distances measuring the change in the width of the thermometer wire. These measurements are shown in figure 6.9.
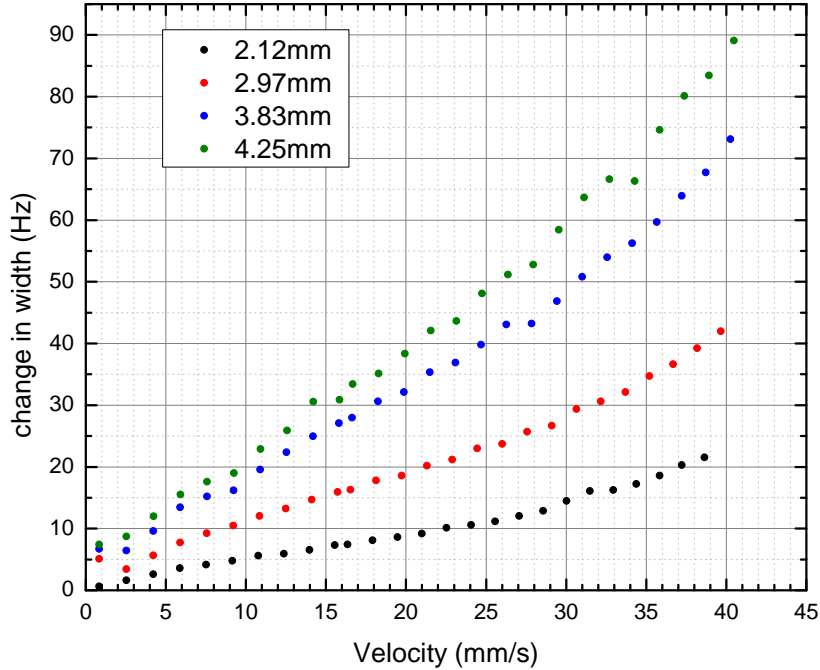
Figure 6.9: The change in width of the thermometer wire as a function of velocity of the flopper moving over different distances.

We believe that the increase in changing width for $3 - 4\,\mathrm{mm}$ distances comes from the magnetic flux lines depinning from the superconducting wire in flopper. The most suitable distance for the measurement was $2\,\mathrm{mm}$, due to it being short, leaving enough space between the flopper and the cell wall (unlike $4\,\mathrm{mm}$ when the flopper almost touches the cell wall), but at the same time being long enough, that even at the highest velocities of $60\,\mathrm{mm\,s^{-1}}$ the acceleration and deceleration intervals were still considerably shorter then the linear motion interval. All of the strokes were repeated at least three times in the data-tracking run and then usually averaged to give the points that we plot.

The measurement was left to continue while the inner cell warmed. The width change of $4.5\,\mu\mathrm{m}$ wire was logged by a fast DAQ tracking program. The results are shown in figure 6.10. The difference between the curves is associated with the rise in temperature. However, the shapes of both curves are identical throughout
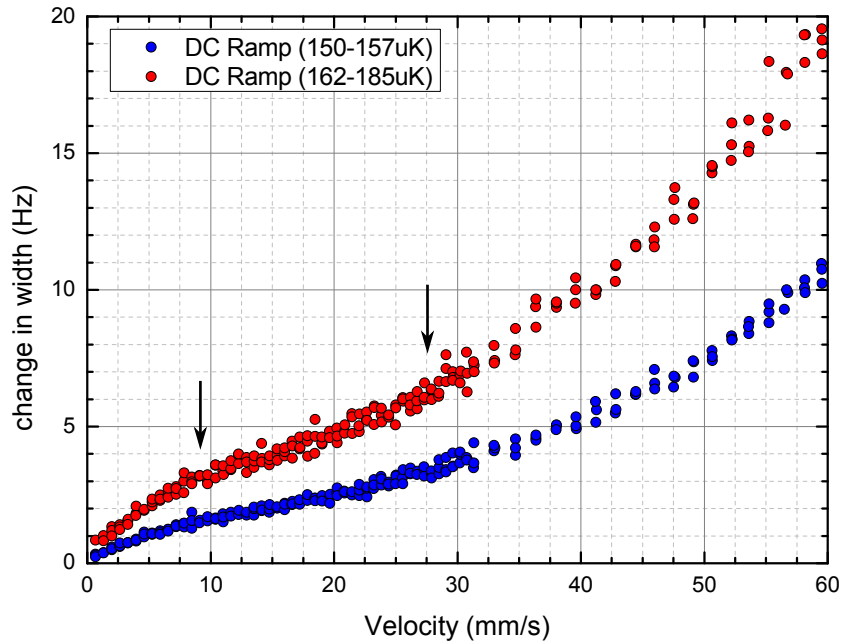
Figure 6.10: The change of widths of $4.5\,\mu$m thermometer wire as function of flopper velocity. The arrows label $v_L/3$ and v_L.

the whole velocity range showing only a mild increase in width change at higher velocities. The larger spread of points at velocities above $30\,\mathrm{mm\,s^{-1}}$ comes from the programmed velocity script calculations. Using the force calibration, the changing width is converted to a damping force, shown in figure 6.11. An AC drive sweep and a corresponding thermal curve are plotted along side the DC strokes. Here we see the striking difference between the AC and DC motion of the flopper. To our surprise there is no sudden onset of damping at $9\,\mathrm{mm\,s^{-1}}$ not even at the Landau critical velocity of $27\,\mathrm{mm\,s^{-1}}$. The DC results show only a very slow rise starting at $v_L/3$ but nothing suggesting mass pair breaking and breakdown of superfluid. At our experimental temperatures such process would be clearly visible as a large increase in damping instead of this slow rise.

By calculating the reduced velocity and reduced force we are able to eliminate
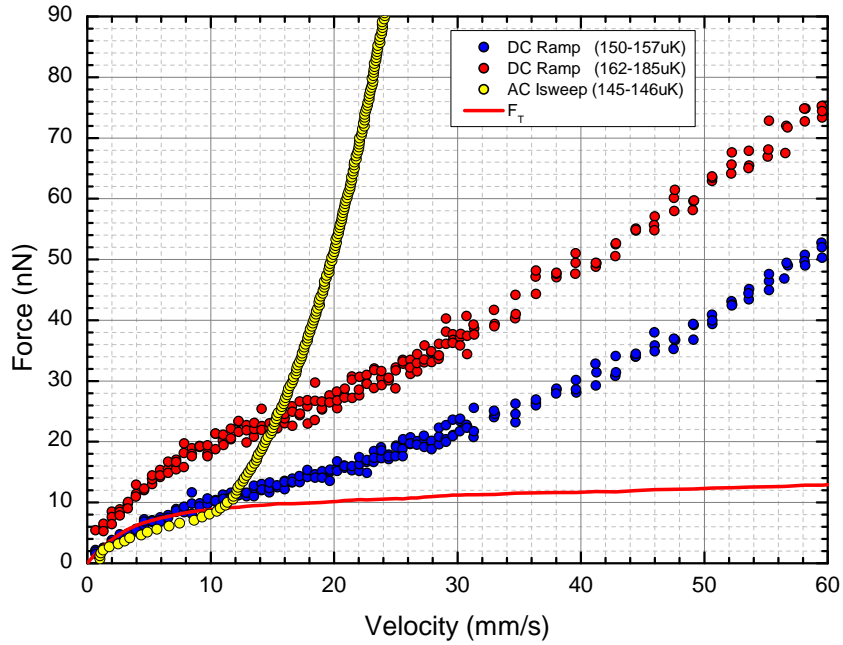
Figure 6.11: Calculated damping force as a function of flopper velocity. Blue circles correspond to measurements in the $150\,\mu\mathrm{K} - 157\,\mu\mathrm{K}$ temperature range and red correspond to the $162\,\mu\mathrm{K} - 185\,\mu\mathrm{K}$. The yellow points are from an AC drive sweep of the flopper at comparable temperatures ($146\,\mu\mathrm{K}$). The red line is the calculated thermal damping force.

all temperature dependencies from the data. For the reduced velocity we can write

$$v_{Red} = \frac{p_F v}{k_B T}, \tag{6.8}$$

here v is the velocity of the flopper and T is the temperature measured by the thermometer wire before each stroke. The reduced force is then calculated by dividing the force with the initial linear slope of the force to reduced velocity dependency. Also it is important to note that this gets rid of the need for a calibration constant. The amazing thing is that below $v_L/3$ all the objects collapse to the same thermal damping form as seen in figure 6.12. Using this technique we can compare DC motion with AC drive sweeps of wires and tuning forks at any temperatures within the ballistic limit.

101
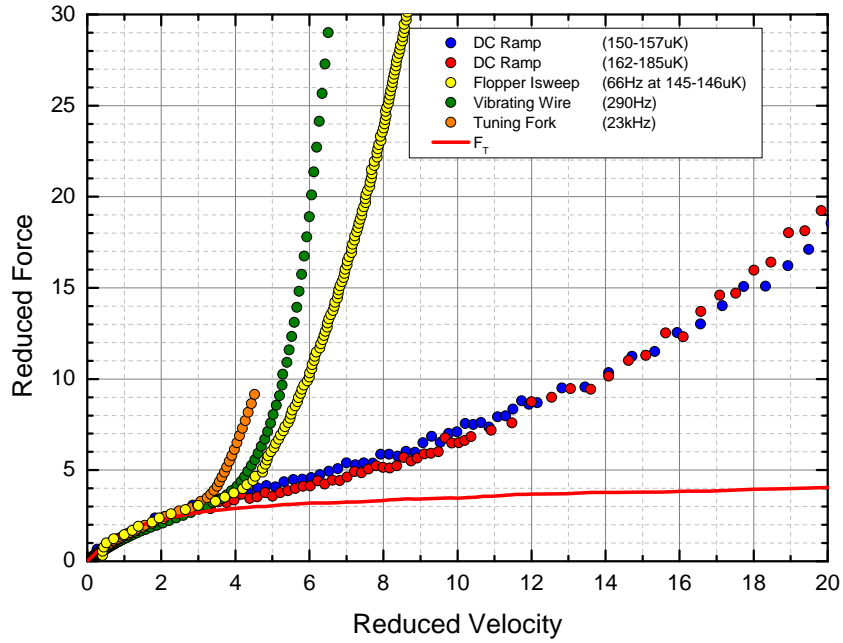
Figure 6.12: Reduced force vs reduced velocity. Comparing the DC strokes of flopper with flopper AC drive sweep and $4.5\,\mu$m drive sweep. Reduced velocity is described by equation (6.8).

All the measurements were done in the ballistic regime. If the temperature is too high, meaning that the system is no longer in ballistic regime, the thermal quasiparticle damping increases dramatically and effectively masks any features on the force-velocity plots as seen in figure 6.13. Both of the series were done in identical fashion, meaning that the program set-up was identical and the distance, over which the flopper moved, was identical. The second series becomes heavily influenced by thermal quasiparticles as the temperature in the cell increased above the ballistic limit. We were warming up the normal component instead of breaking pairs, and this got worse as the temperature increased.
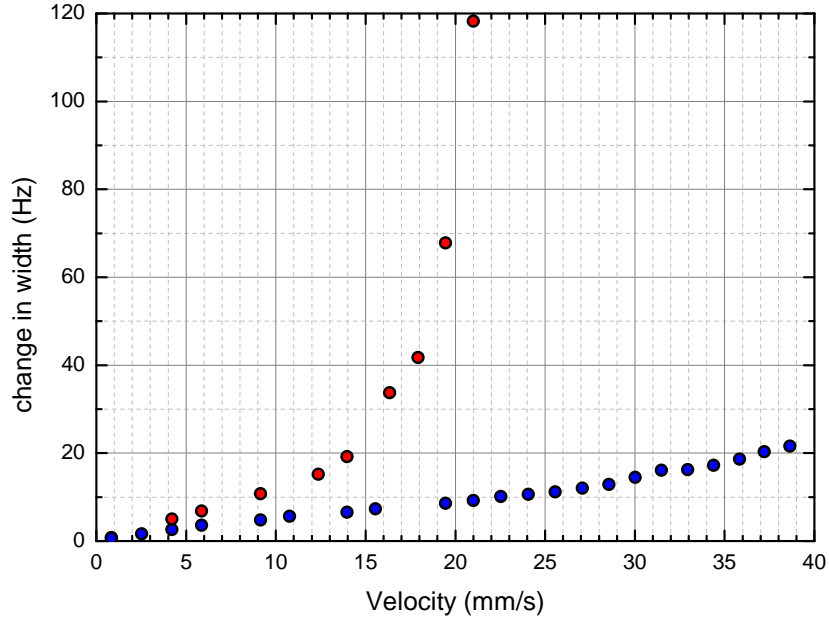
Figure 6.13: Two same stroke series during a slow warm-up (i.e. same velocity sequence, same length of stroke). The first series (blue) was done while the system was still within the ballistic regime $T \approx 180\,\mu\text{K}$. The large increase in damping of the second series (red) is due to the system warming up $T > 220\,\mu\text{K}$.

6.2.4 Flopper frequency dependence

After all our measurements so far, we had data for the on-resonance and DC motion of the flopper (66 Hz and 0 Hz). These two being so different fuelled our curiosity in what the transition between the on-resonance and DC motion might be. Our next set of amplitude sweep measurements was performed in an off-resonance mode of flopper, reducing the frequency form 66 Hz down to 20 Hz while measuring the response of the thermometer wire. This measurement was proved to be very difficult, because driving the flopper off-resonance required very high drives in order to reach desired velocities, in some cases these drives were unreachable by our set-up (i.e. too high currents). The results are shown in figure 6.14. Since a single series took a considerable amount of time, the ambient temperature of the cell was different for each measured series. Therefore in order to compare them we subtracted the thermal damping from all of the series. From the figure

103
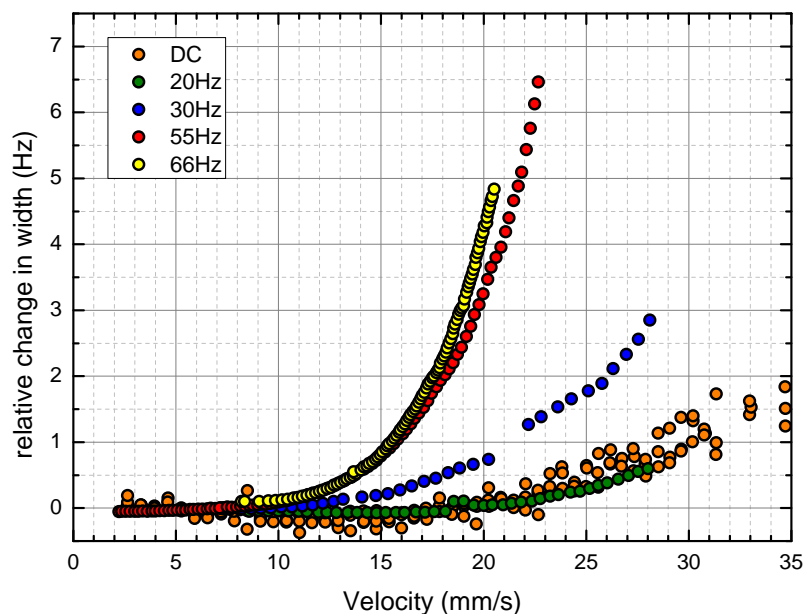
Figure 6.14: Relative change in width as a function of flopper velocity for different flopper frequencies. The yellow dots correspond to on resonance measurements of flopper and the orange correspond to DC strokes.

it seems that the 20 Hz series is similar to the DC strokes data which implies that the process preventing the extra dissipation has a time constant of approximately 25 ms. However, due to the fairly high quality factor of the flopper, difficulties arose in measuring the damping force for the low frequency drive sweeps (30 Hz − 20 Hz). When off resonance the damping force is significantly smaller than the inertial and restoring force. Using the phase between in-phase and quadrature signals is the way to extract the damping force signal from the quadrature. For the phase we can write

$$\Theta = \arctan\left(\frac{V_y}{V_x}\right) \pm \phi, \tag{6.9}$$

where V_y and V_x are quadrature and in-phase voltages, and ϕ is the phase between the drive current and the measured voltage. Then for the damping force we can write

$$F_D = BID\cos\left(\Theta\right). \tag{6.10}$$

104

Our set-up was not able to precisely measure ϕ, the generator to lock-in phase difference. This leads to errors for the low frequency data. Future experiments could use a wire with a very small quality factor. This way the off resonance data would be less dependant on the precision of the phase measurement.

6.3 Dissipation model and discussion

The fact that no extra damping, coming form pair-breaking processes, is visible means that the bulk superfluid (far away from the wire) does not know about the wire velocity and is not influenced by it. Authors Bardeen and Baym in their articles propose a similar behaviour for superconductors [62] and a weakly interacting Bose gas [63]. In their work, they propose that when the velocity of the superfluid exceeds the Landau critical velocity, the system will spontaneously generate quasiparticles. At $T = 0$ all the quasiparticle states with negative energies become occupied. As all the excitations are fermions they cannot occupy the same momentum states. The creation of quasiparticles at the critical velocity then
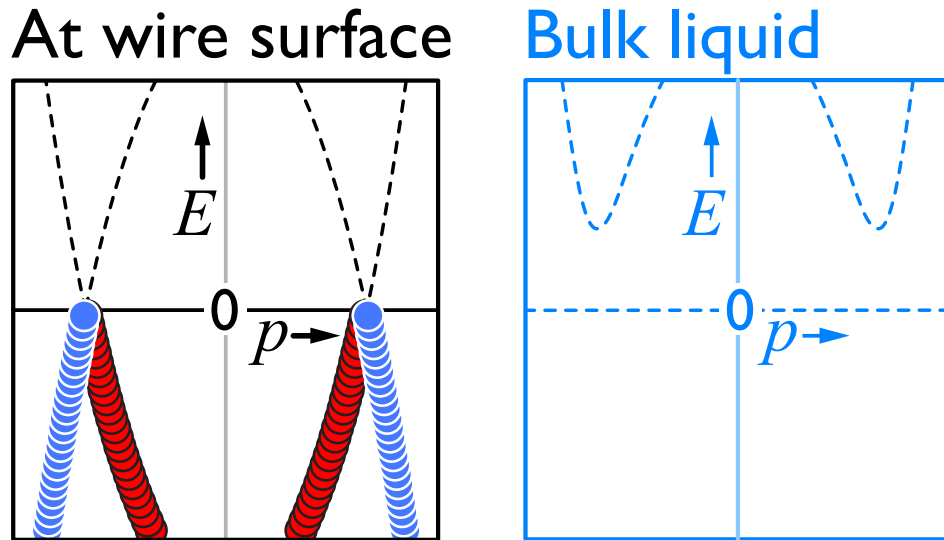
Figure 6.15: Dispersion curves for stationary fluid, left at the wire surface and right in the bulk liquid. Blue circles are quasiholes and red circles are quasiparticles.

results in a normal fluid component being present even at zero temperature.

In order to describe the processes involved we first look at oscillatory behaviour, for which we have a reasonable understanding [64]. First let us assume that $T = 0$ and that the surface of the wire is specular. Then as mentioned in section 5.1

at the wire surface the energy gap is suppressed to 0 giving rise to empty low energy states. Figure 6.15 shows the appropriate dispersion curves in the frame of reference of the wire. As the wire moves the dispersion curves will tilt. It is worth reiterating that, due to pure potential flow around a wire moving at a velocity of v (subsection 4.4.6), the superfluid at the wire surface will move at velocity of $2v$. Due to elastic collisions with the wire surface the excitations start to populate states on the positive momentum side (referred to as $+p$). In turn this will lead to depletion of states on the negative momentum side (referred to as $-p$) as illustrated in figure 6.16. We refer to this as a "cross-branch" process.
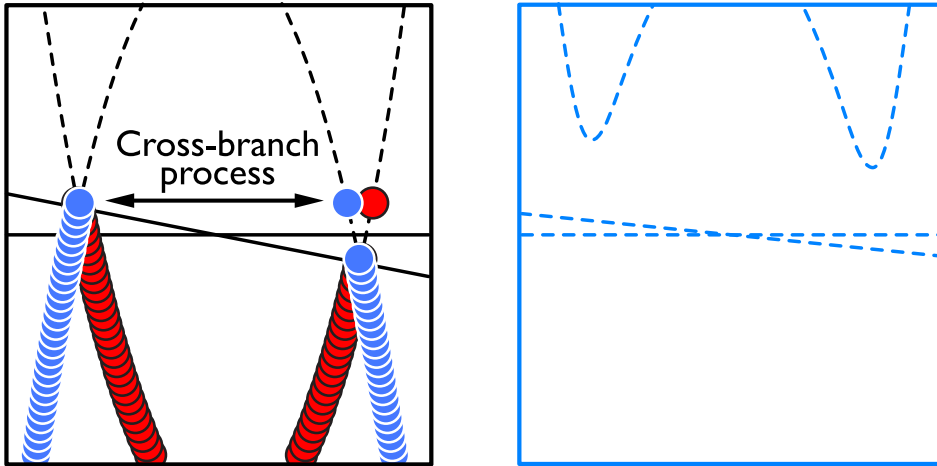
Figure 6.16: Dispersion curves for moving fluid with cross-branching process $v < \Delta/3p_F$.

At constant velocities the distribution of excitations must eventually come into equilibrium. This is probably also true for slow accelerations and velocities below $\Delta/3p_F$. At fast accelerations it is possible to prevent the cross-branch processes from maintaining equilibrium between the $+p$ and $-p$ sides. If the velocity of the excitations in the $-p$ side is equal to or greater than $\Delta/3p_F$, then the excitations can enter the bulk via an "escape process". This occurs when the minimum of the

$+p$ bulk dispersion curve matches the energy of the excitation's as illustrated in figure 6.17. The excitations on the $-p$ side do not require any additional energy to escape into the bulk. This loss of excitations represents dissipation.
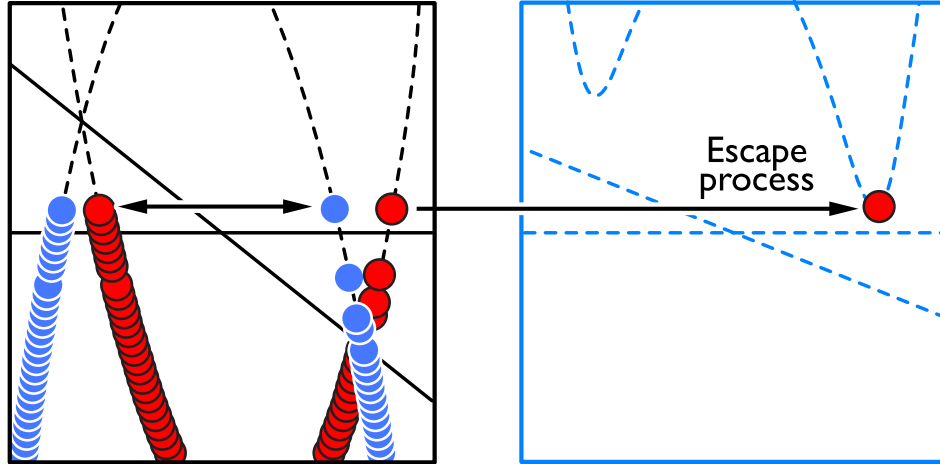
Figure 6.17: Upon reaching the velocity of $v = \Delta/3p_F$ excitations are able to escape into the bulk.

We can conclude that the cross-branch process cannot be a very fast nor very slow process. If it was fast then the distributions of excitations on both $+p$ and $-p$ dispersion curves would be in equilibrium and no dissipation would occur. If it was too slow then the equalisation would not happen and again no dissipation would occur. Experimentally we know that at velocities $v \geq \Delta/3p_F$ the dissipation occurs for oscillatory motion of vibrating objects. From our measurements presented in section 6.2.4 we can assume that the time constant of the cross-branch process is on the order of $25\,\text{ms}$.

Another conclusion we can draw from our measurements is that the excitations are emitted while the wire is accelerating, whereas in steady state with constant velocity, the number of excitations able to escape will become depleted (figure 6.18). Therefore, during the steady motion stage only the thermal force causes

dissipation, even when the flopper is moving at a supercitical velocity. The force we measure in the experiment is averaged over the whole DC stroke and includes extra dissipation due to the quasiparticle emission during the non-steady motion stages (acceleration and deceleration).
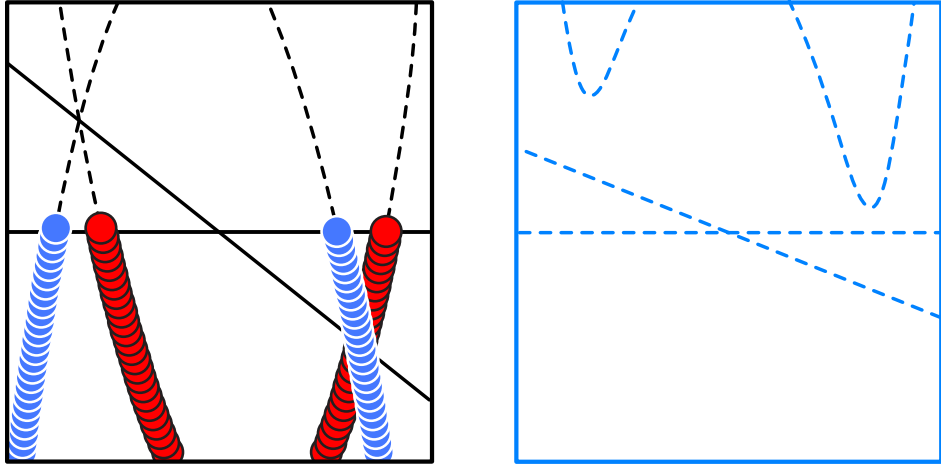
Figure 6.18: Both branches fully equalised after initial acceleration period.

In oscillatory motion this does not happen since upon reaching the maximum velocity the wire is slowed down to $v = 0$ and then the motion is reversed and the whole process starts again.

Let us consider the effect of acceleration to a sustained steady velocity much greater than $v_L/3$. Starting from zero we will see the tilting of the dispersion curves. As the velocity of the wire reaches $v_L/3$, figure 6.19 panel **a)**, the first burst of excitations are able to escape into the bulk. Increasing the velocity further, more surface states around the wire can access the escape process, not just the excitations at the points of maximum flow enhancement, figure 6.19 panel **b)**. This increases the escape probability and the angular range of emission, increasing the damping force during acceleration [65]. Upon reaching the full Landau critical velocity v_L, figure 6.19 panel **c)**, a new escape process becomes available as surface
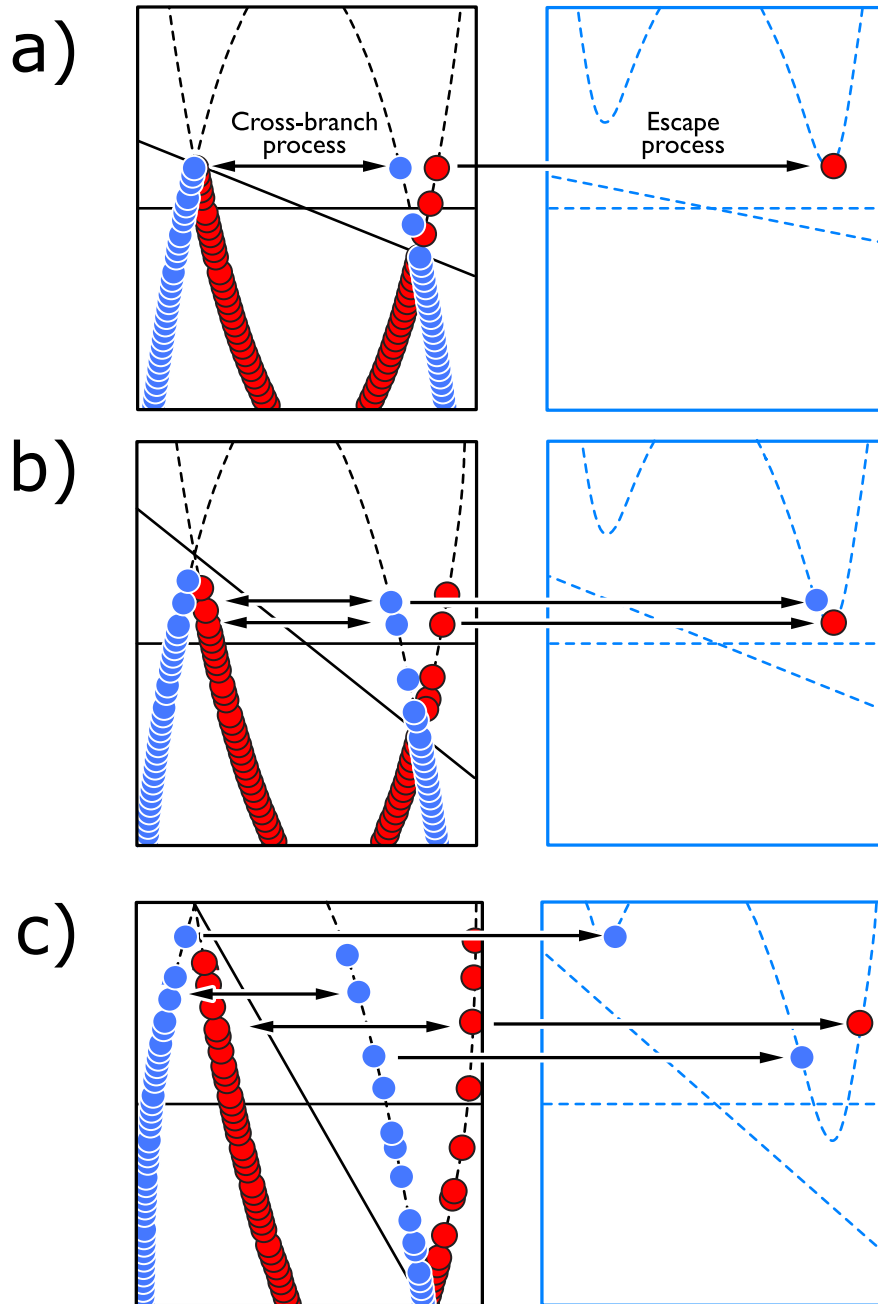
Figure 6.19: Accelerating the wire to higher velocities. Panel a) $v = v_L/3$ first excitations are able to escape into the bulk. Panel b) $v > v_L/3$ more surface excitations are able to escape into the bulk. Panel c) $v = v_L$ new escape process is available for surface excitations directly on the $-p$ side of the dispersion curves.

excitations on the $-p$ side can now escape directly into the minimum of the bulk dispersion curve on the $-p$ side for the first time. This new process increases the escape probability for excitations and can be seen in the measured data as a small

increase in slope when $v > v_L$ (figures 6.10, 6.11 and 6.12).

If the acceleration becomes zero at a final velocity above v_L the surface excitation distributions will equilibrate, thus cutting of the escape processes and the dissipation ceases. Subsequently during the deceleration at the end of the stroke, the dispersion curves tilt in the opposite way. Now the $+p$ side of the dispersion relation is being lifted while the $-p$ side is being lowered. The same cross-branching and escape processes come into play giving another burst of escaping excitations upon deceleration.

This theoretical idea is very similar to that proposed by Lambert in [64] for oscillatory motion. In further analysis, the damping force acting on the flopper moving in DC motion has to be split into a sum of intrinsic, thermal and pair breaking contribution. The intrinsic damping is very small and we assume it to be independent of temperature. The thermal damping has a well known temperature dependence described by equation (6.2) and this component is displayed in both figures 6.11 and 6.12 as a red line. The slight rise in the lines at high velocities accounts for the increasing temperature in the cell during the stroke series. In the case of the pair-breaking force, a possible functional form for the force-velocity dependence was suggested by Lambert

$$F_{PB} = C \left(\frac{v}{v_c} - 1 \right)^2 / v, \tag{6.11}$$

where C is a constant. This function is valid for velocities $v > v_c = v_L/3$ when pair breaking starts. Subtracting the known thermal force component from the AC and DC data leaves only the contribution to the damping due to pair-breaking. The dashed lines in figure 6.20 represent a fit to the model suggested by Lambert with $v_c = 9 \, \text{mm s}^{-1}$ and $C = 70 \, \text{pW}$ for DC data series, but $C = 590 \, \text{pW}$ for the AC sweep. We might estimate that the constant C is the energy required to create N quasiparticles in a time τ, where each quasiparticle has an energy of $\Delta + k_B T$.
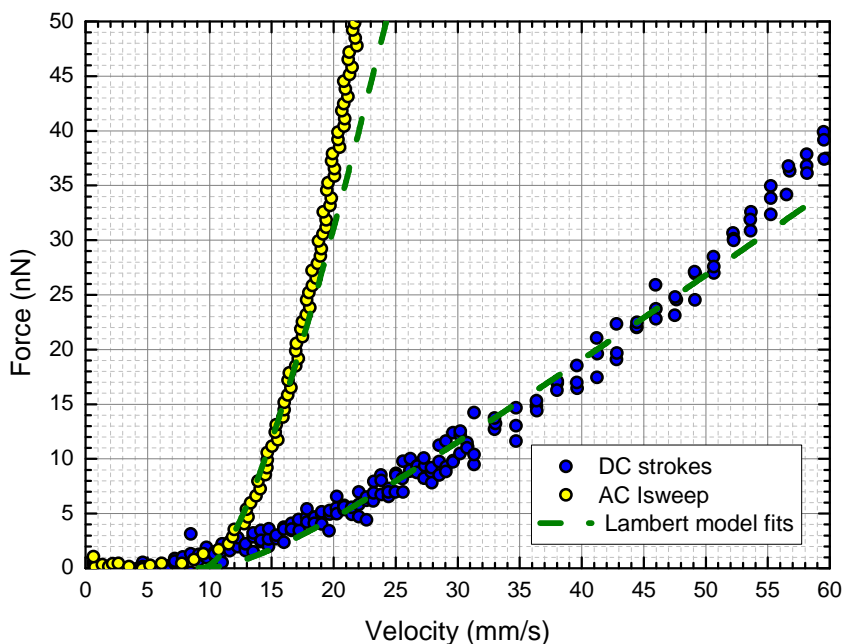
Figure 6.20: AC and DC motion force-velocity curves with thermal force removed leaving only the pair-breaking component of the damping force. The dashed green lines represent the fit to our data using model proposed by Lambert (equation (6.11)).

Then for N we can write

$$N = \frac{C\tau}{\Delta + k_B T},$$

(6.12)

where τ is a characteristic time of motion. For the DC motion this gives a total number of excited quasiparticles $N = 4 \times 10^{14}$. By knowing N and the density of ^{3}He we calculated the volume that these particles occupy. By approximating the flopper crossbar as a rectangle we estimate the length scale over which the flopper interacts with the quasiparticles. This interaction distance is approximately 100 nm, pleasingly similar to the coherence length in superfluid ^{3}He (coherence length in ^{3}He is approximately 88 nm [20]). This suggests that the flopper excites quasiparticles over a distance on the order of the length scale over which the superfluid order parameter is influenced by the presence of the flopper. We obtain similar result when we do the same calculations for AC motion.

For the AC motion the Lambert model is consistent with the experiment up until $v = 2v_c$. There might be two reasons for this discrepancy above $2v_c$. First is the onset of turbulence. For vibrating wires it exists at around the same velocities as the pair-breaking begins [66] and it has been observed on the flopper while in AC motion [59]. The detection of damping is sensitive only to quasiparticles and any formation of vortices or turbulence might not be detected (and might even provide shielding). Secondly, there are concerns about fully understanding the pair-breaking process. For the DC motion the model lines are in good agreement up until $v \approx 50\,\mathrm{mm\,s^{-1}}$.

We speculate that the main difference between the experiments performed by Ahonen et.al.[2] and our experiment is the size of the moving objects, or more specifically; the presence or absence of Andreev bound states (surface bound states). If the object is smaller than the coherence length of $^3\mathrm{He}$, the energy gap is only marginally disturbed by the objects surface. However, if the object is larger than the coherence length, the energy gap is suppressed at the surface, giving rise to free AB states. In our experiment, these states "shield" the wire from the bulk superfluid at temperatures close to $0\,K$ and there is no mechanism for the bulk condensate to know what the flopper is doing on the other side of the boundary layer. Whereas the ions used in [2] were microscopic objects that were fully exposed to the bulk superfluid. All of our results were consistent up to $190\,\mu\mathrm{K}$

Chapter 7

Summary

7.1 Summary

The work described in this thesis focuses on the study of fundamental physical properties of superfluid ^{3}He-B, mainly probing the energy gap with quartz tuning forks and the Landau critical velocity utilising a new measurement tool namely the flopper.

The experimental facility including the measurement arrangement and the principles of measurement techniques were described. The preparation and construction process, placement of the flopper inside the experimental cell, together with its associated pick-up coils, were described in detail. The production, installation and operation of devices used for thermometry, such as vibrating wires and quartz tuning forks were also introduced and explained.

Experiments probing the ^{3}He-B energy gap distortion in large magnetic fields using tuning forks showed very good agreement with theory and with data collected from previous experiments using vibrating wires [3, 57, 58]. Difficulties in determination of the energy gap arose in high magnetic fields, where an effect similar to the quasiparticle shielding reported in [59] was observed. However, unlike in [59] the shielding does not depend on the temperature of the ^{3}He-B, but on external magnetic field. To elucidate this other experiments need to be done.

In order to use the flopper as an experimental tool to investigate its interaction with superfluid ^{3}He-B, it had to undergo two different calibrations. The first one was the position calibration. Passing the wire between the two pick-up coils, which are a known distance apart, induces voltages in the coils, which is proportional to the distance of the flopper crossbar from each of the coils. The second was the force calibration. This calibration was done by using AC drive pulses on the flopper, and measuring the power dissipated by the flopper with the corresponding thermometer response.

The most important experimental results are presented in chapter 6. These measurements took place in superfluid ^{3}He-B at temperatures $T = 0.2T_C$ and zero pressure, in the regime of ballistic quasiparticle transport. By performing AC

drive sweeps of the flopper, we were able to map out the force-velocity response of the device. A clear onset in dissipation was observed at one third of the Landau critical velocity v_L, as expected and proven time and time again by using multiple different oscillatory devices. At velocities $v = v_L/3$, the dispersion curves are shifted enough due to backflow that excitations from the surface states can escape into the bulk. This is seen as an increase in damping force on the flopper. However, the most astonishing result was observed when switching from the AC regime to linear strokes at constant velocity. The onset of dissipation, so typical for AC motion, is dramatically reduced. Furthermore, the dissipation is modest up to the full Landau velocity, and with unexpectedly small dissipation even when v_L is exceeded.

The model developed to describe the dissipation processes emphasizes a mechanism of promoting local excitations into the bulk condensate, when the dispersion curves are tilted by $\pm p_F v$ during the initial acceleration period. Excitations on the $-p_F v$ side with high enough energies are able to escape into the bulk liquid by scattering of the wire surface. However, upon reaching the constant velocity the tilting process stops and the local states on the $-p_F v$ side become depleted, while the $+p_F v$ becomes occupied due to cross-branch processes. Upon slowing the flopper down, the process repeats in reverse, until the dispersion curves tilt back to their original configuration when the wire is stationary. It is clear that the absence of velocity reversal plays a key role in the difference between AC and DC motion. The weak point in the data analysis is the calibration of the power dissipated by the flopper during its motion.

Using the functional form for the force-velocity dependence suggested by Lambert we have approximated the interaction distance of the flopper, suggesting that the flopper interacts only with particles within the coherence length from the wire surface. From the off-resonance drive sweeps of the flopper we have estimated that the time constant of the cross-branching process is approximately 25 ms.

7.2 Future work

Future measurements of the Landau critical velocity could use the black body radiator technique. The flopper or a similar device would be put within a BBR along with several thermometers. This way the power dissipated by the flopper in AC or DC motion would be known precisely from the BBR calibrations.

The technique of the flopper and the results presented in this thesis open doors to many new exciting physical experiments. One such experiment in zero temperature limit could be the study of Andreev-Majorana bound states, trapped at the surface of the flopper. The application of different flopper type wires with various diameters and/or quality of surface should influence the density of the surface trapped excitations, and therefore lead to different damping experienced by the wire at the same temperature. This type of experiment could give insight into surface states and shed light on the properties Andreev-Majorana particles in ^{3}He-B. As part of this proposed future work is an open question if there is influence of the solid layers of ^{3}He on the surface of the wire on the property of Andreev-Majorana states [67, 68].

Another experiment could be the study of condensed matter analogue of the Unruh effect [69, 70, 71] in superfluid ^{3}He-B. The Unruh effect predicts that an accelerating object generates a flux of thermal excitations via a tunnelling process and the flux magnitude is proportional to the acceleration.

For the current cell and its tail piece a new magnet has been designed for the study of ^{3}He-B and ^{3}He-A phase boundary interactions and ^{3}He-A nucleation processes. This magnet will be able to create a bubble of high magnetic field within the tail piece, thus allowing ^{3}He-A to nucleate without touching the walls of the experimental cell. This could answer what triggers the nucleation of ^{3}He-A phase from ^{3}He-B phase without the influence of solid walls.

Appendix

Appendix A

Gap parameters of the ³He-B in magnetic field at 0 bar.

$\hbar\omega_L/\Delta_{BW}$	$\Delta_\perp/\Delta_{BW}$	$\Delta_\parallel/\Delta_{BW}$	$\hbar\bar\omega_L/\Delta_{BW}$
0.05	1.0013	0.997	0.100
0.06	1.0020	0.996	0.120
0.07	1.0026	0.995	0.141
0.08	1.0034	0.993	0.161
0.09	1.0043	0.991	0.181
0.10	1.0052	0.989	0.202
0.11	1.0063	0.987	0.222
0.12	1.0075	0.985	0.243
0.13	1.0088	0.982	0.264
0.14	1.0102	0.979	0.285
0.15	1.0118	0.976	0.306
0.16	1.0134	0.972	0.328
0.17	1.0152	0.968	0.349
0.18	1.0171	0.964	0.371
0.19	1.0191	0.959	0.394
0.20	1.0213	0.954	0.416
0.21	1.0237	0.949	0.439
0.22	1.0262	0.943	0.462
0.23	1.0288	0.936	0.486
0.24	1.0314	0.930	0.509
0.25	1.0345	0.922	0.534
0.26	1.0377	0.914	0.559
0.27	1.0412	0.905	0.585
0.28	1.0450	0.894	0.612
0.29	1.0490	0.883	0.640
0.30	1.0534	0.870	0.669
0.31	1.0584	0.855	0.700
0.32	1.0640	0.837	0.734
0.33	1.0705	0.814	0.770

The table gives the values of parallel $\Delta_\parallel$ and perpendicular $\Delta_\perp$ energy gap parameters as function of magnetic field. Δ_{BW} is the energy gap at zero magnetic field. All the values were calculated by Nagai [57].

Appendix B

Calculating the drive force, to move the flopper at uniform velocity over the set distance without ringing at the acceleration and deceleration period, starts with expressing the total distance travelled by the flopper. The total distance can be calculated as a sum of distance travelled during acceleration, linear motion and deceleration. In our scripts the acceleration and deceleration periods have the same duration, i.e., the distance covered is the same. To calculate the distance travelled during acceleration period we will use a 4th order polynomial function in form

$$x_a = (At + B)t^3, \tag{1}$$

where t is the time resolution of ramp, $B = C/T_a^2$ and $A = -B/(2T_a)$. Here C is the constant final velocity of the ramp and T_a is the duration of the acceleration period. We do this in order to obtain velocity, acceleration, force and current as continuous functions, without any steps. The linear part is simply $x_l = CT_l$, where T_l is the duration of the linear period. For the total force we write

$$m^*\ddot{x} + \Gamma\dot{x} + m^*\omega^2 x = F, \tag{2}$$

here ω is the resonant frequency of the flopper and Γ is the projected damping of the environment. The Γ term, in ballistic regime, is very small and it can be neglected giving the final form for the force applied on the flopper

$$\ddot{x} + \omega^2 x = F, \tag{3}$$

This force is then recalculated to set the flopper driving current.

Bibliography

[1] D. R. Allum, P. V. E. McClintock, and A. Phillips. The Breakdown of Superfluidity in Liquid ^{4}He: An Experimental Test of Landau's Theory. *Philosophical Transactions of the Royal Society of London A: Mathematical, Physical and Engineering Sciences*, 284(1320):179–224, jan 1977.

[2] A. I. Ahonen, J. Kokko, O. V. Lounasmaa, M. A. Paalanen, R. C. Richardson, W. Schoepe, and Y. Takano. Mobility of negative ions in superfluid ^{3}He. *Phys. Rev. Lett.*, 37:511–515, 1976.

[3] S. N. Fisher. *Ph.D. thesis*. Lancaster University, 1991.

[4] V. V. Dmitriev, A. A. Senin, A. A. Soldatov, and A. N. Yudin. Polar phase of superfluid ^{3}He in anisotropic aerogel. *Phys. Rev. Lett.*, 115:165304, 2015.

[5] G. E. Volovik. *The Universe in a Helium Droplet*. Clarendon Press, Oxford, 2003.

[6] N. B. Kopnin and G. E. Volovik. Critical velocity and event horizon in pair-correlated systems with relativistic fermionic quasiparticles. *Journal of Experimental and Theoretical Physics Letters*, 67(2):140–145, 1998.

[7] L. D. Landau. Theory of superfluidity of helium ii. *J. Phys. Moscow*, 5:71, 1941.

[8] L. D. Landau. *J. Phys. Moscow*, 11:91, 1947.

[9] P. Kapitza. Viscosity of liquid helium below the λ-point. *Nature*, 141:74, 1938.

[10] J. F. Allen and A. D. Misener. Flow phenomena in liquid helium ii. *Nature*, 142:643–644, 1938.

[11] J. F. Allen and A. D. Misener. Flow of liquid helium ii. *Nature*, 141:75, 1938.

[12] D. G. Henshaw and A. D. B. Woods. Modes of Atomic Motions in Liquid Helium by Inelastic Scattering of Neutrons. *Phys. Rev.*, 121(5):1266–1274, mar 1961.

[13] D. R. Tilley and J. Tilley. *Superfluidity and Superconductivity.* IOP, 2001.

[14] T. Ellis and P. V. E. McClintock. The Breakdown of Superfluidity in Liquid ^{4}He. Measurement of the Landau Critical Velocity for Roton Creation. *Philosophical Transactions of the Royal Society of London A: Mathematical, Physical and Engineering Sciences*, 315(1532):259–300, aug 1985.

[15] L. P. Pitaevskii. *JETP*, 37(1754), 1959.

[16] D. D. Osheroff, R. C. Richardson, and D. M. Lee. Evidence for a new phase of solid ^{3}He. *Phys. Rev. Lett.*, 28(885), 1972.

[17] J. Bardeen, L. N. Cooper, and J. R. Schrieffer. Microscopic Theory of Superconductivity. *Phys. Rev.*, 106:162, 1957.

[18] Naoto Masuhara, Brian C. Watson, and Mark W. Meisel. Direct measurement of the energy gap of superfluid ^{3}He $- B$ in the low-temperature limit. *Phys. Rev. Lett.*, 85:2537–2540, 2000.

[19] Dennis S. Greywall. ^{3}He specific heat and thermometry at millikelvin temperatures. *Phys. Rev. B*, 33:7520–7538, 1986.

[20] E.R. Dobbs. *Helium Three.* 2000.

[21] C. A. M. Castelijns, K. F. Coates, A. M. Guénault, S. G. Mussett, and G. R. Pickett. Landau critical velocity for a macroscopic object moving in superfluid

^{3}He-B: Evidence for gap suppression at a moving surface. *Phys. Rev. Lett.*, 56(1):69–72, jan 1986.

[22] J. P. Carney, A. M. Guénault, G. R. Pickett, and G. F. Spencer. Extreme nonlinear damping by the quasiparticle gas in superfluid ^3B in the low-temperature limit. *Phys. Rev. Lett.*, 62:3042–3045, 1989.

[23] D. I. Bradley, M. Človečko, E. Gažo, and P. Skyba. Probing Andreev Reflection in Superfluid ^{3}He-B Using a Quartz Tuning Fork. *JLTP*, 152(5):147–155, 2008.

[24] D. I. Bradley, P. Crookston, S. N. Fisher, A. Ganshin, A. M. Guénault, R. P. Haley, M. J. Jackson, G. R. Pickett, R. Schanen, and V. Tsepelin. The Damping of a Quartz Tuning Fork in Superfluid ^{3}He-B at Low Temperatures. *JLTP*, 157(5-6):476–501, 2009.

[25] R. Blaauwgeers, M. Blazkova, M. Človečko, V. B. Eltsov, R. de Graaf, J. Hosio, M. Krusius, D. Schmoranzer, W. Schoepe, L. Skrbek, P. Skyba, R. E. Solntsev, and D. E. Zmeev. Quartz Tuning Fork: Thermometer, Pressure- and Viscometer for Helium Liquids. *JLTP*, 146(5-6):537–562, 2007.

[26] F. Pobell. *Matters and Methods at Low Temperatures.* Springer Verlag, 1996.

[27] J. Tuoriniemi, J. Martikainen, E. Pentti, A. Sebedash, S. Boldarev, and G. R. Pickett. Towards superfluidity of ^{3}He diluted by ^{4}He. *JLTP*, 129(5-6):531–545, 2002.

[28] J. Bardeen, L. N. Cooper, and J. R. Schrieffer. Theory of superconductivity. *Phys. Rev.*, 108(5):1175, 1957.

[29] D. Vollhardt and P. Wölfle. *The Superfluid Phases of Helium 3.* Taylor & Francis, 1990.

[30] R. S. Šafrata and kol. *Fyzika nízkych teplot.* Matfyzpress, MFF KU Praha, 1998.

[31] P. W. Anderson and W. F. Brinkman. *Phys. Rev. Lett.*, 30(1108), 1973.

[32] R. Balian and N. R. Werthamer. *Phys. Rev.*, 131(1553), 1963.

[33] A. J. Leggett. A theoretical description of the new phases of liquid ^{3}He. *Reviews of Modern Physics*, 47(2):331–414, 1975.

[34] S. N. Fisher, A. M. Guénault, C. J. Kennedy, and G. R. Pickett. *Phys. Rev. Lett.*, 63(23), 1989.

[35] S. N. Fisher, G. R. Pickett, and R. J. Watts-Tobin. A microscopic calculation of the force on a wire moving through superfluid ^{3}He-B in the ballistic regime. *JLTP*, 83(3):225–235, 1991.

[36] A. F. Andreev. *Zh. Eksp. Toer. Fiz.*, 46(1823), 1964.

[37] O. V. Lounasmaa. *Experimental Principles and Methods Below 1K*. Academic Press Inc. (London) Ltd., 1974.

[38] O. V. Lounasmaa. Dilution refrigeration. *Journal of Physics E: Scientific Instruments*, 12(8):668, 1979.

[39] A. M. Guénault. *Basic Superfluids*. Taylor & Francis, 2003.

[40] P. M. Berglund, G. J. Ehnholm, R. G. Gylling, O. V. Lounasmaa, and R. P. Svik. Nuclear refrigeration of copper. *Cryogenics*, 12:297–299, 1972.

[41] G. L. Pollack. Kapitza resistance. *Rev. Mod. Phys.*, 41:48–81, 1969.

[42] S. N. Fisher, A. M. Guénault, C. J. Kennedy, and G. R. Pickett. Blackbody source and detector of ballistic quasiparticles in ^{3}He$-B$: Emission angle from a wire moving at supercritical velocity. *Phys. Rev. Lett.*, 69:1073–1076, 1992.

[43] C. Bäuerle, Yu. M. Bunkov, S. N. Fisher, and H. Godfrin. Temperature scale and heat capacity of superfluid ^{3}He-b in the 100μK range. *Phys. Rev. B*, 57:14381–14386, 1998.

[44] A. M. Guénault, V. Keith, C. J. Kennedy, and G. R. Pickett. Transition from hydrodynamic to ballistic quasiparticle behavior in a fermi gas: The response of a vibrating-wire resonator in a ^{3}He-^{4}He solution from 0.3 to 10 mk. *Phys. Rev. Lett.*, 50:522–525, 1983.

[45] A. M. Guénault, V. Keith, C. J. Kennedy, and G. R. Pickett. Observation of the mechanical response of the condensate in ^{3}He-*b* in the regime of negligible normal fluid density. *Phys. Rev. Lett.*, 51:589–592, 1983.

[46] P. Skyba. Notes on measurement methods of mechanical resonators used in low temperature physics. *JLTP*, 160(5-6):219–239, 2010.

[47] A. M. Guénault, V. Keith, C. J. Kennedy, S. G. Mussett, and G. R. Pickett. The mechanical behavior of a vibrating wire in superfluid ^{3}He-B in the ballistic limit. *JLTP*, 62(5-6):511–523, 1986.

[48] D. I. Bradley, M. Človečko, M. J. Fear, S. N. Fisher, A. M. Guénault, R. P. Haley, C. R. Lawson, G. R. Pickett, R. Schanen, V. Tsepelin, and P. Williams. A New Device for Studying Low or Zero Frequency Mechanical Motion at Very Low Temperatures. *JLTP*, 165(3):1–18, 2011.

[49] Citizen America. Quartz Tuning Fork, part number CM315.

[50] M. Fear. *Ph.D. thesis*. Lancaster University, 2011.

[51] D. I. Bradley, P. Crookston, M. J. Fear, S. N. Fisher, G. Foulds, D. Garg, A. M. Guénault, E. Guise, R. P. Haley, O. Kolosov, G. R. Pickett, R. Schanen, and V. Tsepelin. Measuring the prong velocity of quartz tuning forks used to probe quantum fluids. *JLTP*, 161(5-6):536–547, 2010.

[52] D. I. Bradley, M. Človečko, S. N. Fisher, D. Garg, E. Guise, R. P. Haley, O. Kolosov, G. R. Pickett, V. Tsepelin, D. Schmoranzer, and L. Skrbek. Crossover from hydrodynamic to acoustic drag on quartz tuning forks in normal and superfluid ^{4}He. *Phys. Rev. B*, 85:014501, 2012.

[53] R. Schanen. private communication.

[54] G. K. Batchelor. *An introduction to fluid dynamics.* Cambridge University Press, 1973.

[55] William S. Janna. *Introduction to Fluid Mechanics.* CRC Press, 4 edition, 2010.

[56] H. Choi, J. P. Davis, J. Pollanen, and W. P. Halperin. Surface specific heat of ^{3}He and andreev bound states. *Phys. Rev. Lett.*, 96:125301, 2006.

[57] K. Nagai. private communication.

[58] M. Ashida and K. Nagai. *Prog. Theor. Phys.*, 74(949), 1985.

[59] D. I. Bradley. Anomalous damping of a low frequency vibrating wire in superfluid ^{3}He-B due to vortex shielding. *JLTP*, 175(1):372–378, 2013.

[60] P. Skyba. private communication, 2015.

[61] D. E. Zmeev. A Method for Driving an Oscillator at a Quasi-Uniform Velocity. *JLTP*, 175(1-2):480–485, 2014.

[62] J. Bardeen. Critical fields and currents in superconductors. *Reviews of modern physics*, 34:667, 1962.

[63] G. Baym and C. J. Pethick. Landau critical velocity in weakly interacting bose gases. *Phys. Rev. A*, 86:023602, 2012.

[64] C. J. Lambert. Theory of pair breaking by vibrating macroscopic objects in superfluid ^{3}He. *Physica B*, 178(1-4):294–303, 1992.

[65] S. N. Fisher, A. M. Guénault, C. J. Kennedy, and G. R. Pickett. Blackbody Source and Detector of Ballistic Quasiparticles in ^{3}He-B: Emission Angle From a Wire Moving at Supercritical Velocity. *Phys. Rev. Lett.*, 69:1073–1076, 1992.

[66] D. I. Bradley, S. N. Fisher, A. M. Guénault, M. R. Lowe, G. R. Pickett, A. Rahm, and R. C. V. Whitehead. Quantum turbulence in superfluid ^{3}He illuminated by a beam of quasiparticle excitations. *Phys. Rev. Lett.*, 93:235302, 2004.

[67] G. E. Volovik. Fermion zero modes at the boundary of superfluid ^{3}He-B. *JETP Letters*, 90(5):398–401, 2009.

[68] Suk Bum Chung and Shou-Cheng Zhang. Detecting the Majorana Fermion Surface State of ^{3}He-B through Spin Relaxation. *Phys. Rev. Lett.*, 103(23):235301, dec 2009.

[69] W. G. Unruh. Notes on black-hole evaporation. *Phys. Rev. D*, 14(4):870–892, 1976.

[70] G. E. Volovik. *Exotic properties of superfluid ^{3}He.* World Scientific Publishing Co., 1992.

[71] R. Schuetzhold and W. G. Unruh. *Quantum analogues: From phase transition to black holes and cosmology.* Springer Verlag, 2007.